INFORMATION TO USERS

This manuscript has been reproduced from the microfilm master. UMI films the text directly from the original or copy submitted. Thus, some thesis and dissertation copies are in typewriter face, while others may be from any type of computer printer.

The quality of this reproduction is dependent upon the quality of the copy submitted. Broken or indistinct print, colored or poor quality illustrations and photographs, print bleedthrough, substandard margins, and improper alignment can adversely affect reproduction.

In the unlikely event that the author did not send UMI a complete manuscript and there are missing pages, these will be noted. Also, if unauthorized copyright material had to be removed, a note will indicate the deletion.

Oversize materials (e.g., maps, drawings, charts) are reproduced by sectioning the original, beginning at the upper left-hand corner and continuing from left to right in equal sections with small overlaps. Each original is also photographed in one exposure and is included in reduced form at the back of the book.

Photographs included in the original manuscript have been reproduced xerographically in this copy. Higher quality 6" x 9" black and white photographic prints are available for any photographs or illustrations appearing in this copy for an additional charge. Contact UMI directly to order.

UMI

A Bell & Howell Information Company
300 North Zeeb Road, Ann Arbor MI 48106-1346 USA
313/761-4700 800/521-0600

CRUSTAL AND UPPER MANTLE VELOCITY STRUCTURE IN ALASKA

A

THESIS

Presented to the Faculty

of the University of Alaska Fairbanks

in Partial Fulfillment of the Requirements

for the Degree of

DOCTOR OF PHILOSOPHY

By

Cheryl Kaye Searcy, B.S.

Fairbanks, Alaska

August 1996

CRUSTAL AND UPPER MANTLE VELOCITY STRUCTURE IN ALASKA

by

Cheryl Kaye Searcy

RECOMMENDED:

Paul Layer
Dr. Paul Layer

W. J. Stringer
Dr. William Stringer for Dr. Koji Kawasaki

D. B. Stone
Dr. David Stone

Douglas Christensen
Dr. Douglas Christensen, Advisory Committee Chair

Paul Layer
Dr. Paul Layer, Head,
Department of Geology and Geophysics

APPROVED:

Paul B. Reichardt
Dr. Paul Reichardt, Dean, College of Natural Sciences

Joseph P. Kan
Dr. Joseph Kan, Dean of the Graduate School

7/19/96
Date

Abstract

The crustal and upper-mantle velocity structure of Alaska testifies to a complex tectonic framework. Much of the structure and history of this framework remains to be conclusively determined. This thesis presents the results of three independent investigations of velocity structure in Alaska in an attempt to provide some insight into its tectonic development. The first study involved the analysis of receiver functions to determine velocity structure beneath College Station (COL), located in Fairbanks, Alaska. Receiver functions from several back azimuths facilitate a fairly detailed analysis of deep crustal velocity structure beneath COL, including an indication that Moho dips to the northeast. The second study also employed receiver function methods to investigate velocity structure for four temporary three-component seismic stations placed in the Brooks Range. Due to the short deployment of these stations in the Brooks Range only a rough estimate of crustal velocities were obtained. Nevertheless, crustal thickening beneath the Brooks Range is clearly indicated by an increase in the depth to Moho. The final study undertaken was a three-dimensional tomographic P-wave velocity inversion for the subduction zone region of south central Alaska. Data for the tomographic inversion consisted of local and teleseismic ray paths. The resulting velocity perturbations indicate a positive velocity anomaly associated with the subducting Pacific plate. Furthermore, the tomographic images clarify physical characteristics of the subducting plate such as structure, thickness, and depth of penetration into the mantle.

Table of Contents

List of Figures

List of Tables

Acknowledgments

I owe a debt of gratitude to many who have helped me through my graduate studies. First and foremost, I wish to thank my committee chair and thesis advisor, Dr. Douglas Christensen. Doug always made sure that I was funded so I could focus my energies on my studies. He provided expert scientific guidance and in addition managed to foster a sense of self-confidence in me. I would also like to express my appreciation to Dr. David Stone who was primarily responsible for my arrival at the Geophysical Institute. I have long admired his breadth of scientific knowledge and in particular his knowledge of Alaskan tectonics. His careful editing of my thesis and instructions on proper English, greatly improved this document. Dr. Paul Layer was a valuable member of my committee. In addition to his scientific knowledge, he is skilled in department protocol and guided me accordingly. Dr. Koji Kawasaki brought a wealth of knowledge to my committee. I am thankful for his encouragement and careful editing of this thesis. I dedicate this manuscript to his memory. I wish to thank Dr. William Stringer for stepping in under these sorrowful circumstances and taking over where Koji left off.

I am also grateful to Dr. Dapeng Zhao for the use of computer codes used in the tomographic work. For the receiver function studies, I used codes developed by Dr. Charles Ammon and Dr. Tom Owens. Dr. Charles Ammon provided a careful, and thorough review of the College Station paper. I am obliged to Dr. John Lahr for his helpful comments on the tomography study.

This research was funded by the National Science Foundation (grant numbers:

EAR-95-06379, EAR-90-04112, and EAR-91-18090) and the United States Geological Survey/Alaska Volcano Observatory (grant number 1434-93-A1127). The Keck foundation donated much of the instrumentation that was used in the Brooks Range study. I wish to acknowledge the Society of Exploration Geophysics (SEG) for awarding me a scholarship for two years.

Finally, I would like to thank Craig for always believing in me.

CHAPTER 1

Introduction

This thesis consists of a body of work which I accomplished while in the doctoral program at the University of Alaska. Chapters 3, 4 and 6 contain complete manuscripts that have either been published or are in the process of being submitted for publication at the time of this writing. Chapters 2 and 5 detail methods that were used but not completely described in the manuscripts.

Alaska possesses an intriguing tectonic framework, the history and structure of which is still being unraveled. It is the location of a major convergent plate boundary that is transitional in nature from normal subduction along the Aleutian trench to a transform fault system at the southeastern edge of the state. The structure, location and relative motion of the subducting plate in the transitional zone is still to be conclusively determined. The Pacific Plate motion has translated allochthonous terranes from the south into collision with the North America Plate and, in fact, much of the Alaska land mass is comprised of these exotic terranes (*Coney et al., 1980; Jones et al., 1982; Stone et al., 1982; Stone and Wallace, 1987, Plafker and Berg, 1994*). The interactions of these terranes with each other, the North American Plate boundary, and the subduction zone are complicated. Currently, the Yakutat Terrane is in the process of colliding with the Alaska land mass. Its impingement appears to be transferring stresses deep into the interior of Alaska. This is made evident by the occurrence of relatively large earthquakes (~7.0) that have occurred even as far inland as the Fairbanks area (*Page et al., 1991*). A detailed reflection study by

Page et al. (1994) suggests that the lower crust of the Yakutat Terrane is being sheared off and subducted along with the Pacific Plate. They hypothesize that the added thickness of the subducting material causes a resistance of the Pacific Plate to flex downward and may explain the anomalously low dip angle of the subducting plate in this region. This low dip angle results in a large contact zone between the Pacific Plate and the overriding North American Plate which initiates large earthquakes. Further inland there is evidence that the collisions of previous terranes have similar histories to that of the Yakutat Terrane. The lower crust of the Yukon-Tanana Terrane is believed to have been sheared off and underthrust by portions of the Wrangelia Terrane (*Beaudoin et al.. 1992*) perhaps in an older subduction environment. It is also thought that the collision of terranes has caused a southward migration of the subduction trench in a series of step-like jumps (*Jacob et al.. 1977; Coney et al., 1980; Stone and Wallace. 1987; Lahr et al., 1988).*

It has been estimated that 900 to 1000 km of oceanic plate has been subducted beneath Alaska since 30 to 35 m.y. ago (*Delong et al., 1978).* However, the maximum depth of earthquakes associated with the subducting slab is only about 250 km (*Burbach and Frohlich, 1986*). The question as to whether the Pacific Plate has been thermally absorbed below its deepest seismicity such that it no longer possesses a high velocity signature from the background mantle has been the source of some controversy (*Boyd and Creager. 1991*).

The northern part of Alaska consists of the relatively aseismic North Slope and the Brooks Range. The Brooks Range is an east-west trending fold-and-thrust belt that is part of a series of subterranes that comprise the Arctic Alaska Terrane. The uplift of this range

is believed to have been due to the impingement of an island-arc on the Arctic Alaska continent following the subduction of oceanic crust beneath that arc (*Gottschalk, 1990*).

The work presented in this thesis is unified in its attempt to study the structure of the crust and upper mantle of Alaska and thereby derive some insight into the tectonic processes from which this structure arises.

Chapter 3, *Velocity structure beneath College Station Alaska from receiver functions*, contains analysis of velocity structure deduced from the study of receiver functions for the Yukon-Tanana Terrane in the Fairbanks area. My coauthors, Douglas Christensen and George Zandt contributed to this paper by providing guidance and consultation. The body of work for this manuscript is my own.

Chapter 4, *Crustal structure and anisotropy in the Brooks Range, Alaska*, presents a velocity model for the Brooks Range based also on the analysis of receiver functions. This study is enhanced by an analysis of shear wave anisotropy for the same stations at which the receiver function study was undertaken. The entire shear wave analysis was conducted by Douglas Christensen and Martha Savage. The receiver function part of the study was conducted by myself with the guidance of Douglas Christensen.

Chapter 6, *Tomographic inversion for P-wave velocity structure in the South-Central Alaska subduction zone*, is comprised of a three-dimensional tomographic study for the subduction zone velocity structure in South Central Alaska. My coauthor, Douglas Christensen, contributed to this manuscript by providing guidance and consultation. The tomographic study described in this chapter is original work of my own.

Chapter 1 References

Beaudoin, B. C., G. S. Fuis, W. D. Mooney, W. J. Nokleberg, and N. I. Christensen, Thin, low-velocity crust beneath the southern Yukon-Tanana terrane, east central Alaska: results from Trans-Alaska Crustal Transect refraction/wide-angle reflection data, *J. Geophys. Res.*, *97*, 1921-1942, 1992.

Boyd, T. M., and K. C. Creager, The geometry of Aleutian subduction: three-dimensional seismic imaging, *J. Geophys. Res.*, *96*, 2267-2291, 1991.

Burbach, G. V. and C. Frohlich, Intermediate and deep seismicity and lateral structure of subducted lithosphere in the circum-Pacific region, *Rev. Geophys.*, *24*, 833-874, 1986.

Delong, S. E., P. J. Fox, and F. W. McDowell, Subduction of the Kula Ridge at the Aleutian Trench, *Geol. Soc. Am. Bull.*, *89*, 83-95, 1978.

Coney, P. J., D. L. Jones, and J. W. H. Monger, Cordilleran suspect terranes, *Nature*, *288*, 329-333, 1980.

Gottschalk, R. R., Structural evolution of the schist belt, south-central Brooks Range fold and thrust belt, Alaska, *J. Struct. Geol.*, 12, 453-469, 1990.

Jacob, K. H., K. N. Nakamura, and J. N. Davies, Trench-volcano gap along the Aleutian arc: facts and speculations on the role of terrigenous sediments, in *Island Arcs, Deep Sea Trenches and Back Arc Basins*. Maurice Ewing Series I, edited by M. Talwani and W. Pitman Am. Geophys. Union, 1977.

Jones, D. L., N. J. Silberling, W. Gilbert, and P. Coney, Character, distribution, and tec-

tonic significance of accretionary terranes in the central Alaska Range, *J. Geophys. Res.*, *87*, 3709-3717, 1982.

Lahr, J. C., R. A. Page, C. D. Stephens, and D. H. Christensen, Unusual earthquakes in the Gulf of Alaska and fragmentation of the Pacific Plate., *Geophys. Res. Let.*, *15*, 1483-1486, 1988.

Page, R. A., N. N. Biswas, J. C. Lahr, and H. Pulpan, Seismicity of continental Alaska, in *Neotectonics of North America: Boulder, Colorado, Geological Society of America, Decade Map Volume 1*, edited by D. B Slemmons, E. R. Engdahl, M. D. Zoback, and D. D. Blackwell, 47-68, 1991.

Page, R. A. , T. M. Brocher, C. D. Stephens, J. C. Lahr, K. A. Fogelman, and M. A. Fisher, Piggyback subduction at the eastern end of the Aleutian Trench and the giant asperity that ruptured in the great 1964 earthquake, in *SUBCON, an interdisciplinary conference on the subduction process*, convened by D. Scholl, G. Bebout and S. Kirby, 152-154, 1994.

Plafker, G., and H. C. Berg, editors, *The geology of Alaska, The geology of North America, volume G-1, Decade of North American Geology Project*, U. S. Geological Survey, Boulder Colorado, 1994.

Stone, D. B., B. C. Panuska, and D. R. Packer, Paleolatitudes versus time for southern Alaska, *J. Geophy. Res.*, *87*, 3697-3707, 1982.

Stone, D. B., and W. K. Wallace, A geologic framework of Alaska, *Episodes*, *10*, 283-289, 1987.

CHAPTER 2

Receiver Function Methods

2.1. Introduction

A receiver function is defined as that part of a seismic waveform that is recorded at a single seismic station that is due to the response of local crustal structure. For waveforms arriving at a recording station with a steeply incident path, particle motions are polarized such that most of the P-wave ground motion is recorded on the vertical component instrument and the S-wave motion is recorded on the horizontal component instruments. The S-wave energy immediately following the direct P arrival arises from P to S conversions in the crust in a narrow cone beneath the recording station. The result of this is that crustal information is contained in the coda following the direct P arrival on the horizontal component seismograms. For our purposes, receiver functions are defined as the wave forms on the horizontal components of the seismogram that represent these locally generated, direct P to S conversions as well as multiple bounces of P to S conversions in the crustal layers, generally including Moho. In practice, the receiver function must be isolated from the raw data by deconvolving the vertical seismogram from the radial and tangential components as described in section 2.2. In this manner source and path effects are removed from the horizontal components and P-wave multiples are suppressed leaving the P to S conversions that define the receiver function. Figure 2.1 illustrates a synthetic receiver function generated by a simple layer over a half space velocity model.

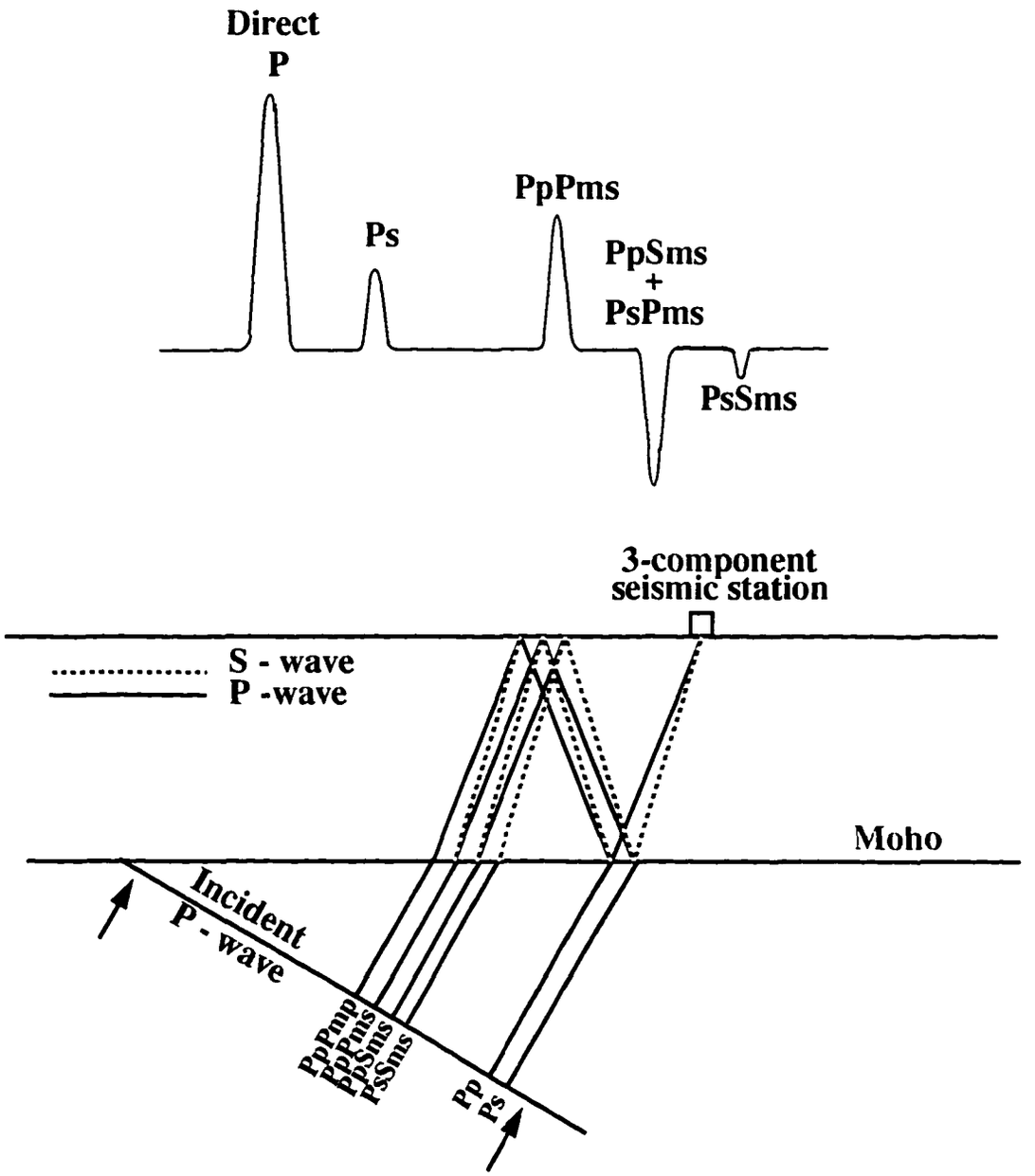

Fig. 2.1: Diagram of a receiver function. Top drawing shows a synthetic receiver function in which peak and trough arrivals following the direct P arrival occur in response to conversions and multiple bounces at Moho. In each case the last leg of the ray path in spent in S-wave particle motion. In the lower diagram a schematic of these ray paths is drawn. Redrawn from *Owens (1984)*.

The phase arrival notation used here follows that of *Langston et al. (1977)* where the first capital P represents the incident wave, the subsequent lower case s or p indicates the converted up going ray in the layer, and a following capital P or S refers to a down going ray. The reflection at Moho is indicated by an "m" (figure 2.1).

The relative arrival times of the converted phases following the direct P phase are directly dependent on the product of the velocity above and the depth to the boundary of conversion. There is therefore a range of possible depth-velocity distributions that are capable of producing a given arrival on the receiver function. Because of this nonuniqueness some *a priori* information on a region's velocity structure is necessary to provide a detailed interpretation of the receiver function. In spite of this limitation, receiver functions are useful in providing additional information such as indications of low velocity layers and to corroborate previous studies. The amplitude of the arrival is indicative of the velocity contrast and the polarity of the arrival is determined by whether the velocity contrast is positive or negative.

The horizontal components of ground motion are rotated into radial and tangential components before the receiver functions are isolated in the deconvolution process. The radial component represents ground motion in the horizontal plane that lies in line with the source-receiver azimuth and is positive away from the source. The tangential component is defined as the horizontal motion perpendicular to the radial component.

Typically, the major phases on the radial receiver function are the Ps (P to S conversion at Moho) and later multiple conversions within the crust in which the final leg of the ray path is spent in S-wave particle motion. Shallow structure arrivals (i.e. arrivals in

which only the last 10 km or so are spent in S wave particle motion) arrive too closely to the direct P arrival to be discernible. While the resolution of such structure is not usually attempted using receiver functions, high velocity contrasts at shallow depths can also effect the amplitudes of deeper conversions.

For an idealized, perfectly horizontal velocity structure no P to S conversions appear on the tangential receiver function since all S wave motion at the point of conversion will be in the direction of the radial component. Theoretically, arrivals on the tangential receiver function represent conversions at non-horizontal boundaries or from off-azimuth arrivals of incident waves. The tangential component has been shown to be sensitive to contamination by noise and dipping structure at shallow depths *(Lapp et al., 1990)* and hence care must be observed in its interpretation. Nevertheless, important information may be gleaned from the tangential component such as a general dip direction for a dipping velocity boundary. (See section 2.5 for a more detailed discussion on dipping interfaces)

Information about the velocity structure beneath a station can be obtained by the analysis of a single good receiver function making this method ideal for studies in which there exists limited data at a single station. More detailed information about the velocity structure is obtained by the analysis of receiver functions arriving from a range of back azimuths and distances or from receiver functions obtained at more than one station. Furthermore, signal to noise ratios are often increased by stacking together several receiver functions from a limited back-azimuth/distance range. An ideal earthquake for a receiver function study is a teleseismic event with a simple pulse-like source.

2.2. Isolating the Receiver Function

The deconvolution method of *Langston (1979)* and *Ammon (1991)* were used to isolate the receiver functions from the raw data. This method consists of first rotating the north-south and east-west components of the raw data into radial and tangential components. The radial component is defined as the component of the waveform that is parrallel to the direction that the ray path is travelling. The tangential componet is then perpendicular to the direction that the ray path is travelling. In the time domain the radial component of the seismogram ($D_r(t)$) is given by:

$$D_r(t) = I(t) * S(t) * E_r(t) \qquad (2.1)$$

Where $I(t)$ is the instrument response, $S(t)$ is the source function representing both source and path effects outside the study area, and $E_r(t)$ is the radial receiver function. The asterisk represents the convolution operator. Similar equations apply to the tangential and vertical components. The vertical component is deconvolved from the radial and tangential components to remove instrument, source and external path effects. The deconvolution assumes the vertical receiver function may be approximated by a delta function. Thus the vertical seismogram is approximately equal to:

$$D_v(t) \approx I(t) * S(t) \qquad (2.2)$$

Thus the vertical seismogram represents precisely the terms we wish to remove from the

horizontal components. While some errors exist in the delta function assumption, it has been shown to be valid for steeply-incident ray paths (*Owens, 1984*) such as are produced by teleseismic events. Thus in the frequency domain, using the radial component as an example, the receiver function is given by:

$$E_r(\omega) \approx \frac{D_r(\omega)}{I(\omega)S(\omega)} = \frac{D_r(\omega)}{D_v(\omega)} \tag{2.3}$$

Because of noise present in actual data, the final form of the deconvolution is as follows.

$$E_r(\omega) \approx \frac{D_r(\omega)\overline{D_v(\omega)}}{\phi(\omega)} G(\omega) \tag{2.4}$$

Where $\overline{D_v(\omega)}$ is the complex conjugate of $D_v(\omega)$. The Gaussian filter, $G(\omega)$ is used to remove high frequency noise and is defined as:

$$G(\omega) = exp\left(-\frac{\omega}{4a^2}\right) \tag{2.5}$$

Parameter a is the width of the Gaussian filter. The factor, $\phi(\omega)$ is the minimum allowable spectral amplitude for the vertical seismogram. It insures the stability of the deconvolution by forcing a minimum value in the denominator of equation (2.4) for spectral regions where the vertical seismogram has little or no information. The minimum allow-

able amplitude, $\phi(\omega)$, as shown in equation 2.6, is expressed as a fraction of the maximum vertical amplitude. The minimum amplitude allowed is determined by the parameter c, called the water level parameter. The water level parameter ranges between 0.0 and 1.0. The optimum parameter for c is one in which $c \cdot max\left|D_v(\omega)\right|^2$ is above the noise level (*Clayton and Wiggins, 1976*):

$$\phi(\omega) = max\{D_v(\omega)\overline{D_v(\omega)}, c \cdot max[D_v(\omega)\overline{D_v(\omega)}]\} \quad (2.6)$$

To determine the best value for the parameters, c and a, a suite of deconvolutions are typically performed for a range of water level parameters (i.e. 0.001, 0.01, 0.1) and Gaussian widths (i.e. 1.0, 2.5) and then judged for stability. Stable results are defined as those waveforms having minimum pre-signal noise and a high resolution of individual arrivals within the receiver function. The optimum values of these parameters for a given inversion will vary from one study to the next and must be determined for each case.

The final step in the deconvolution is to estimate the actual relative amplitudes on the horizontal components. Prior to this step, the receiver functions are normalized to unit amplitude since noise in the deconvolution produces a variability in peak amplitudes *(Ammon, 1991)*. The benefit of true amplitude receiver functions is that the effects of shallow structure on the amplitudes of deep conversions are suppressed (*Cassidy, 1992*). This method also reduces the effect of missed boundaries on the amplitudes of deeper conversions *(Cassidy and Ellis, 1993)*. True amplitudes are achieved by deconvolving the vertical

component from itself using the same water-level parameter that was used in the horizontal deconvolutions and then normalizing the horizontal components by the maximum amplitude of this vertical auto-deconvolution (*Ammon, 1991*).

2.3 Stacking Methods

In order to increase the signal to noise ratio and to decrease the effects of scattering in the upper crust, receiver functions may be stacked. Care must be exercised when stacking true amplitude wave forms since there is a large amplitude difference in waveforms arriving from events at different distances *(Ammon, 1991)*. If it is necessary to stack waveforms from a broad distance range it may be beneficial to delete the last step in the deconvolution process and use normalized amplitudes since their variation with distance is not quite so pronounced. For a truly flat earth model, receiver functions from all back azimuths could be stacked together allowing only for distance variations. In most situations the velocity structure varies from such a purely horizontal model and only receiver functions from a limited back azimuth and distance range can be stacked. In determining the back azimuth and distance range of a given stack it is desirable to have as many receiver functions as possible that are located close enough in space (back azimuth and distance) such that an accurate composite stack results. The exact range may vary with the location of the study being undertaken, regions with stronger lateral variations in velocity requiring tighter stacking bounds.

One stacking method that is often used in receiver function studies is a binning technique, in which a set bin range of the ray parameter and back azimuth is used. Since

this method has the advantage of being completely unbiased it is the best method for studies in which a reasonably high density of data is arriving from certain bins. It has the disadvantage that if a strong velocity variation or boundary lies within a predetermined bin, receiver functions from either side of this variation would be stacked together reducing the ability to resolve that structure.

An alternative unbiased method for determining stacking bounds developed here, is the use of a semblance test to determine the "likeness" of receiver functions to be stacked together. The reasoning is that receiver functions sampling the same crustal and sub-crustal features will have the same peak and trough features. Semblance is a time-domain coherence measure that has the property of being sensitive to amplitude variation. The semblance is given by (*Neidell and Taner, 1971*):

$$S = \frac{\sum_{x=1}^{2}\sum_{y=1}^{2} f_{xy}(0)}{2\sum_{x=1} f_{xx}(0)} \qquad (2.7)$$

where f_{xy} is the cross correlation of the stack (x) with the individual trace (y) and f_{xx} is the autocorrelation:

$$f_{xy}(j) = \sum_{i=1}^{N} x_i y_{i+j} \qquad f_{xx}(j) = \sum_{i=1}^{N} x_i x_{i+j} \qquad (2.8)$$

The semblance ranges between 0 and 1, a semblance of 0 indicating no waveform match and a semblance of 1 being a perfect match. The direct P arrival has the largest amplitude of any peak in the receiver functions and is always correlated in time from one trace to another. In order to keep the semblance calculations from being dominated by this phase, the calculations were performed using the waveform following the direct P.

The stack was first computed using all of the unweighted receiver functions within a given broad back-azimuth and distance range. Initially this range is spatially large, sometimes even a full quadrant. The semblance of each receiver function was calculated with respect to the stacked trace. Individual receiver functions with low semblances were then rejected and the remaining traces were re-stacked. This process was repeated until a stable stack existed. After a few iterations it sometimes becomes apparent that two or three stacks are required, the initially rejected receiver functions coinciding into a single stack. Typically, semblances calculated for receiver functions in an initial stack would cluster together in value with the exception of one or two receiver functions falling well below the others. For example, in the COL study (chapter 3) the initial stack 2 had 16 traces with semblance values that ranged from 0.79 to 0.96 and two traces with semblances values of 0.62 and 0.70. These outliers were the traces that were rejected. In some cases outliers were found to fit better in a nearby stack.

2.4. Inverting Receiver Functions for Velocity Structure

The method used for inverting receiver functions for velocity structure is outlined in *Ammon et al. (1990)*. This time-domain inversion process involves an iteration cycle in

which a given initial model is first pseudo-randomly perturbed. One typically uses the results from previous studies to compose the initial velocity model, however, it has been shown that the inversion process is relatively insensitive to the beginning model (*Owens, 1984*). The closer the initial model is to the actual velocity structure, the fewer the number of iterations required to reach convergence. In study areas where no previous work has been undertaken it is sometimes possible to use forward modeling techniques on the receiver functions to derive a suitable model. A synthetic radial receiver function is computed based on the perturbed initial velocity model and compared to the stacked receiver functions. The following equation is solved by minimizing the L2 norm of the residual vector, $|d\vec{R}|^2$:

$$d\vec{R} = A d\vec{p} \tag{2.9}$$

where A is an m (# of equations) by n (# of unknowns) matrix containing the partial derivative representing the sensitivity of the i^{th} point in the receiver function to a small perturbation in the k^{th} model parameter $\frac{\partial R_i}{\partial p_k}$. The component $d\vec{p}_k$ is the correction vector for the k^{th} element, and dR_i is the residual of the i^{th} element. The partial derivative matrix is inverted by a singular value decomposition method (*Golub and Kahan, 1965*) to compute model parameter changes. Once the model is changed by the correction parameters a synthetic receiver function is again calculated and the process repeated until convergence is reached. In this way one velocity model is produced. The initial model is then once again perturbed and the entire process repeated to produce a total of 24 velocity models.

Variations among the 24 models provides some qualitative insight into the sensitivity of the inversion to the initial velocity model. An overview of the inversion process is illustrated in figure 2.2 where the initial model, final inversion models, and the synthetics produced by those models compared to the true receiver function are shown for stack 1 of the COL study (Chapter 3).

In the inversion process a smoothness trade-off parameter is used (*Ammon et al., 1990*). The function of this parameter is to allow for a stable inversion and has the effect of minimizing roughness in the model. A smoothness parameter of 0.0 allows the model to vary without limit in attempting to match the waveform, increasing this parameter imposes more constraints on the model by minimizing, in a least squares sense, the difference between the initial and final models. An obvious result of using this parameter in the inversion process is to smooth out sharp velocity contrasts. Therefore we can, at best, hope to model such contrasts as a velocity gradient.

The model parameterization in the inversion is limited to that consisting of homogeneous, horizontal layers. Following this assumption, arrivals in the radial receiver function represent P to S wave conversions and multiple reflections due to the earth structure. Another result of this assumption is that the tangential waveform should vanish. Coherent energy appearing on the stacked tangential waveforms represents the presence of off-azimuth energy that may be produced by non-horizontal structure, path effects, or anisotropy.

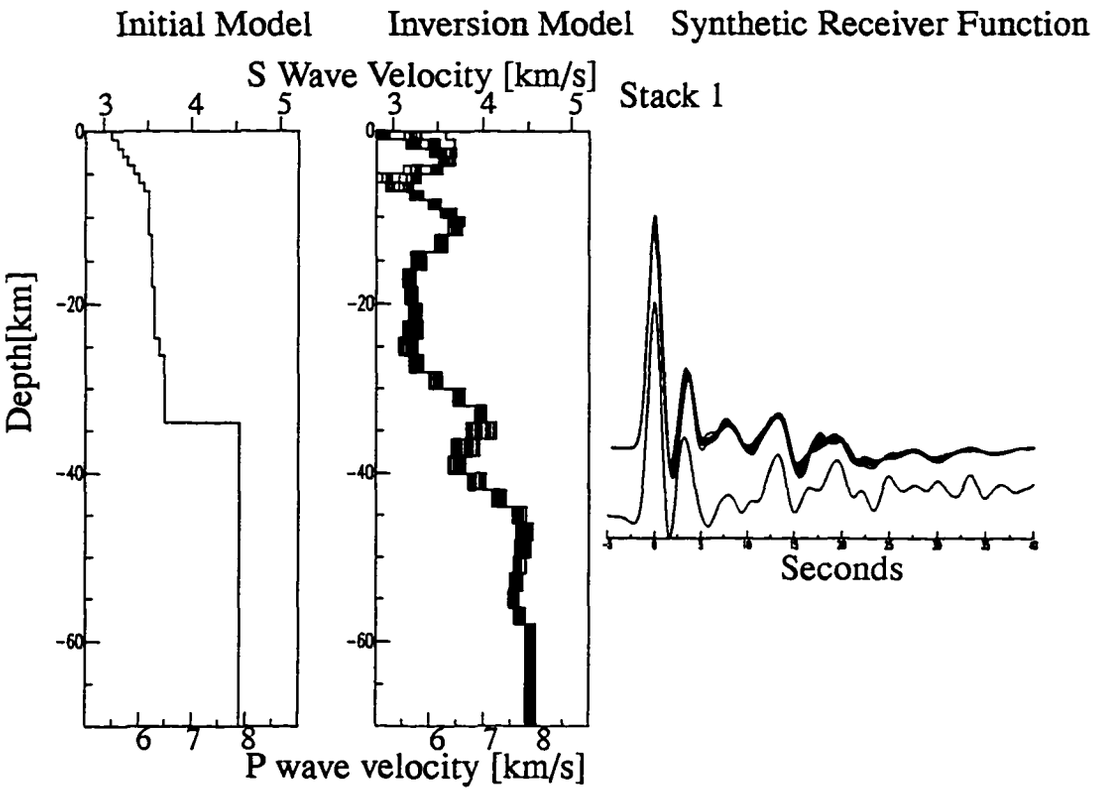

Fig. 2.2: An illustration of the inversion process carried out for stack 1 of the COL study (chapter 3). The initial velocity model is shown on the left. The final inversion velocity models are shown in the center plot and the resulting synthetics for each of the 24 velocity models and the observed stacked receiver function are shown on the right. The observed receiver function is artificially offset below the synthetics for clarity.

2.5. Forward Modeling of Receiver Functions

To gain insight into non-horizontal velocity structure an attempt is made to forward model the receiver function by manually varying a velocity model and producing synthetically traced ray paths through the model. Synthetic seismograms are deconvolved in the same manner that the receiver functions resulting from the actual seismogram were produced. The synthetic receiver functions are then compared to the observed receiver functions and the velocity model varied in an attempt to match the observed receiver functions. In the forward modeling process one typically varies the number of velocity boundaries, the depth to these boundaries, their strike and dip as well as the velocities within each layer. Forward modeling was accomplished using a ray-tracing code that was written by T.J. Owens and described in *Langston (1977)*. For this particular ray-tracing, model parametrization is limited in complexity to planar dipping structures. A general constraint used is to keep the model as structurally simple as possible while attempting to match the true receiver function.

Planar dipping structures are known to affect receiver functions in three ways *Langston (1977)*. Firstly, for the radial receiver function, the amplitude and arrival time of P to S conversions at a dipping boundary vary as a functions of back azimuth and distance. There is a higher P to S conversion efficiency for rays travelling in the up-dip direction. Hence, the largest and most delayed Ps arrivals occur for incident P waves travelling in the up-dip direction and the smallest and earliest arrivals occur for incident P waves travelling in the down-dip direction. In most cases, unless dips are very large, the amplitude and timing variations due to dip are minor effects, the primary factor influencing these amplitudes

being the velocity contrast at the interface. In general, there is a trade-off between dip angle and velocity contrast, i.e. a steeply dipping interface with a small velocity contrast will have the same arrival amplitude as from a shallower dipping interface with a higher velocity contrast. The second effect is that the direct P amplitude on the radial receiver function will also vary with changing back azimuth. The largest amplitudes occur for waves travelling in the down-dip direction and the smallest amplitudes occur for waves travelling in the up-dip direction. In cases of complex velocity structure where more than one interface dips in different directions, this phase will exhibit a complicated azimuthal amplitude variation. Again, as for the Ps conversions, there is a trade-off between dip angle and velocity contrast and the effect is not prominent unless the interface has a relatively large dip ($dip > 30°$). The third effect arises from the fact that dipping layers divert P and S wave particle motion from the vertical-radial plane thereby introducing energy onto the tangential component receiver function. Amplitudes of the direct P arrival are most affected. The largest amplitudes occur for waves arriving along strike of the dipping interface and change polarity as they pass through zero in the up-dip and down-dip directions. The strongest evidence for the existence and orientation of a dipping layer are typically found from examination of the tangential receiver functions since the effects of dipping structure on the radial component are less pronounced. Unfortunately tangential receiver functions can not be precisely modeled due to their susceptibility to pre-signal and deconvolution noise. However, one is typically able to obtain a general dip direction and magnitude from the tangential receiver function. In figure 2.3 the amplitude and polarity variation of the direct P arrival is illustrated for tangential receiver functions recorded

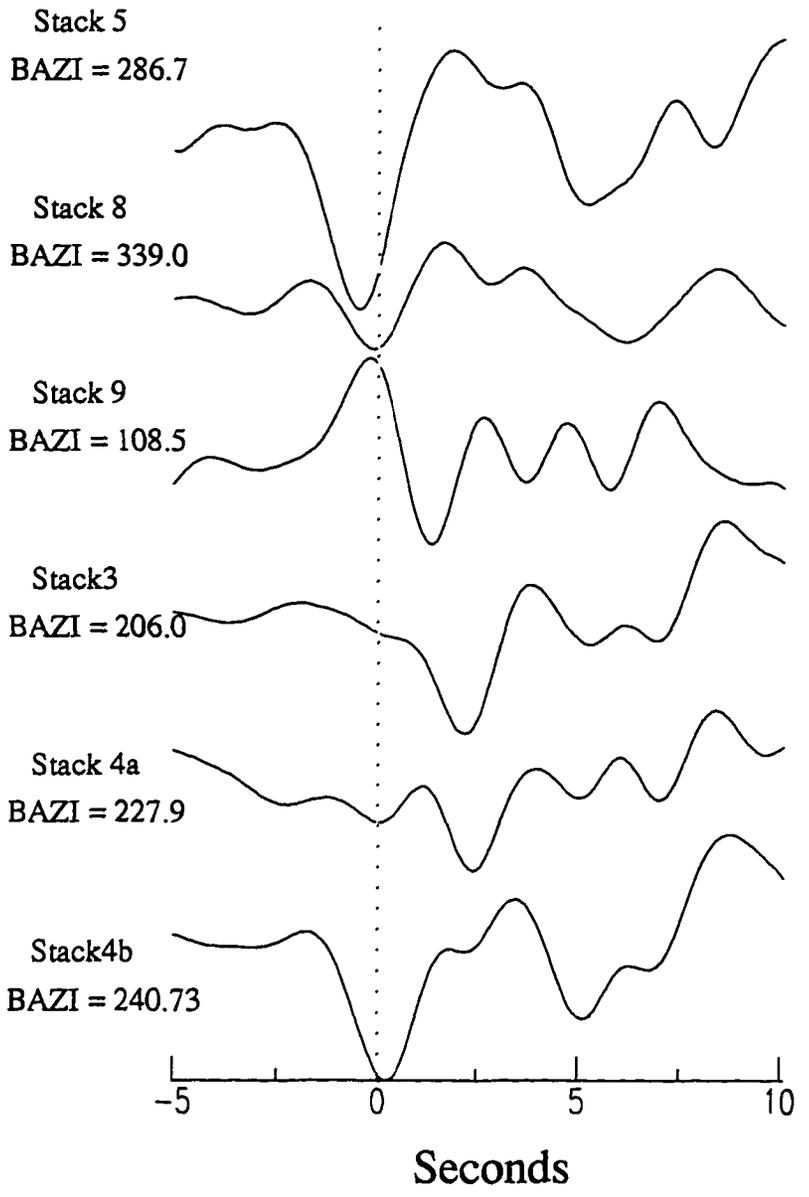

Fig. 2.3: Tangential stacked receiver functions recorded at station COL. Back azimuths shown are averages for the stack. Polarity and amplitude changes occur for the direct P arrival indicating the existence of a dipping interface.

at station COL. This amplitude and polarity variation pattern is consistent with the existence of a dipping velocity boundary believed to be Moho.

2.6. Discussion

Receiver functions are a very useful tool for the study of crustal velocity structure particularly in cases where limited data exists for one or a few stations. Care must be exercised in interpreting receiver function arrivals due to nonuniqueness in the velocity depth product affecting the arrival time of P to S converted phases. For regions in which dipping structure exists, a nonuniqueness also arises between the dip angle and velocity contrast at the interface affecting phase amplitudes. Receiver functions may be contaminated by dipping structure in shallow layers where the receiver functions have little resolution. For these reasons some *a priori* information on the velocity structure is required to corroborate receiver function results and allow definite conclusions to be drawn regarding that structure. Naturally, information on shallow structure is particularly helpful. If such corroborative information exists, receiver functions may be used to determine some independent information on the velocity structure such as deeper crustal structure, depth to Moho, and the orientation of dipping interfaces.

A velocity inversion of the radial receiver function is useful in determining the depth to major interfaces and their relative velocity contrasts. While the inversion process uses only the radial component, forward modeling can make use of both the radial and the tangential receiver functions. In the case where non-horizontal structure exists, coherent energy appears on the tangential component that may be effectively modeled.

Chapter 2 References

Ammon, C. J., G. E. Randall, and G. Zandt, On the non-uniqueness of receiver function inversions, *J. Geophys. Res.*, *95*, 15,303-15,318, 1990.

Ammon, C. J. , The isolation of receiver effects from teleseismic P waveforms, *Bull. Seismol. Soc. Am.*. *81*. 2504-2510, 1991.

Cassidy, J. F., Numerical experiments in broadband receiver function analysis, *Bull. Seismol. Soc. Am.*. *82*. 1453-1474, 1992.

Cassidy, J. F. and R. M. Ellis, S-wave velocity structure of the northern Cascadia subduction zone, *J. Geophys. Res.*, *98*. 4407-4421, 1993.

Clayton, R. W. and R. A. Wiggins, Source shape estimation and deconvolution of teleseismic body waves, *Geophys. J. R. Astr. Soc.*. *47*, 151-177, 1976.

Golub, G. H. and W Kahan, Calculating the singular values and pseudoinverse of a matrix, *SIAM J. Numer. Anal.*. *2*. 205-224, 1965.

Langston, C. A., The effect of planar dipping structure on source and receiver responses for constant ray parameter, *Bull. Seismol. Soc. Am.*. *67*, 1029-1050, 1977.

Langston, C. A., Structure under Mount Rainier, Washington, inferred from teleseismic body waves, *J. Geophys. Res.*, *84*, 4749-4762, 1979.

Lapp, D. B., T. J.Owens, and R. S. Crossen, P-waveform analysis for local subduction geometry south of Puget Sound, Washington, *Pageoph*, *133*, 349-365, 1990.

Neidell, N. S., and T. Taner, Semblance and other coherency measures for multichannel data, *Geophysics*, *36*, 482-497, 1971.

Owens, T. J., *Determination of crustal and upper mantle structure from analysis of broad-band teleseismic P-waveforms*, Ph. D. dissertation, 146 pp., Univ. of Utah, 1984.

CHAPTER 3

Velocity Structure beneath College Station Alaska from Receiver Functions[1]

3.1. Abstract

Time domain inversions of radial receiver functions and forward modeling of radial and tangential receiver functions were used to determine the velocity structure beneath DWWSSN station COL (Fairbanks, Alaska). The receiver functions were deconvolved from teleseismic recordings of magnitude 4.6 to 6.8 earthquakes that were retrieved from the NEIC digital data base. Intermediate period waveforms recorded between February 1982 to November 1985, a total of 57 events, were used in the final analysis.

Receiver functions from similar back azimuths and distances appear to be very uniform. The receiver functions within small azimuth/distance ranges were stacked based on their similarity, determined by semblance tests, in order to increase the signal to noise ratio. At some azimuths (particularly from the west) significant energy is observed in the tangential component indicating the possible existence of dipping structures or other off-azimuth energy. The calculated velocity profiles are complicated, showing several distinct features which are consistent between the different stacks. Among the most obvious features are two strong velocity increases or boundaries in the lower crust. The first of these

1. Chapter 3 is composed of the complete text and figures from the manuscript: *Velocity Structure beneath College Station Alaska from Receiver Functions* by C.Searcy, D. Christensen and G. Zandt, published in the *Bulletin of the Seismological Society of America*, 86, 232-241, 1996.

ramps occurs between 27 and 32 km, a depth which is often associated with the Moho boundary in this region. Forward modeling of the receiver function arrivals associated with this boundary indicates that it has a strike of ~280° and at a dip of at least 10° to the northeast. The velocity profiles and forward modeling also indicate a low velocity layer between about 15 - 28 km depth. This layer is consistent with TACT results that show a layer with high electrical conductivity and a lower than expected seismic velocity interpreted to be Mesozoic flysch at approximately this depth.

3.2. Introduction

The purpose of this study is to estimate the crustal and sub-Moho velocity structure beneath the Digital World-Wide Standard Seismograph Network (DWWSSN) station COL (College Station) located in Fairbanks, Alaska (figure 3.1). COL resides on the Yukon-Tanana terrane (YTT), one of the terranes in a complex collage that composes Alaska. More than 60 allochthonous terranes have been identified in Alaska and neighboring Canada and are distinguished by geologic histories that differ from neighboring terranes (*Jones et al., 1982; Stone and Wallace, 1987; Coney et al., 1980*). On the basis of paleomagnetic evidence, it has been shown that many of the terranes amalgamated far south of their present positions (*Stone et al., 1982*) and were probably translated northward along the western margin of North America. Most of the terranes are bounded by known or suspected faults (*Jones et al., 1982*) although these faults may not be the original sutures that separated the terranes at the time of collision (*Churkin et al., 1980*). The origin of these terranes and the physical processes involved in terrane collisions produced

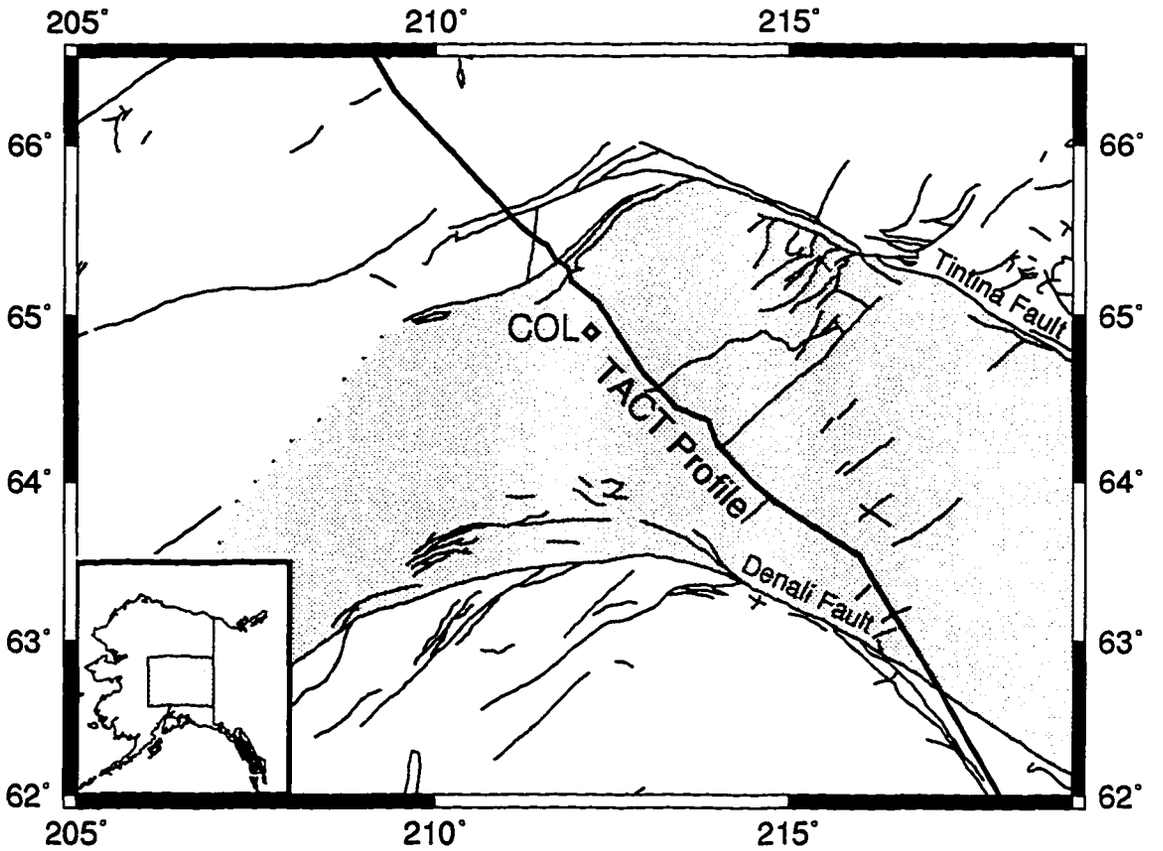

Fig. 3.1: Location map showing the study area. Station COL is indicated by the diamond. The stippled area represents the Yukon-Tanana terrane. The TACT profile is shown by the heavy line. Selected known and inferred faults are drawn to demonstrate the complexity of the area.

complex velocity structures beneath Alaska.

The Yukon-Tanana terrane is the largest of nine major terranes that make up central Alaska. These terranes are believed to have been emplaced and deformed by late Mesozoic or early Cenozoic time and have since provided a backstop for outboard terranes such as Wrangellia and the most recent Yakutat block (*Coney et al., 1980; Stone and Wallace, 1987*). The YTT extends from central Alaska into the Yukon Territory (*Dusel-Bacon and Aleinikoff, 1985*) bordering on the rocks of the Mesozoic North American continental margin to the north along a 1500 km contact zone (*Mortensen and Jilson, 1985*). It is bounded on the northeast by the Tintina Fault and on the southwest by the Denali Fault (*Dusel-Bacon and Aleinikoff, 1985; Beaudoin et al., 1992*).

The YTT is characterized by regionally metamorphosed sedimentary, plutonic and volcanic rocks and is thought to be an assemblage of several discrete subterranes. However, an intense metamorphic event in the middle Cretaceous has obscured many of the boundaries and deformed the subterranes together into nappe structures (*Jones et al., 1982; Churkin et al., 1982; Stone and Wallace, 1987; Coney et al., 1980*). The YTT and the Omineca Crystalline belt in Yukon, Canada are believed to be structurally related, but have been offset 450 km by right lateral movement on the Tintina fault in the late Cretaceous (*Tempelman-Kluit, 1977*).

The YTT has been the subject of several previous studies. Early investigations include an unreversed seismic refraction profile by *Hanson et al. (1968)* and a gravity profile by *Woolard et al. (1960)*. *Hanson et al. (1968)* estimated a Moho depth under Fairbanks of 32 km dipping 7° to the southwest. These results agree with the study of

Woolard et al. (1960) that estimated a Moho depth of 33 km under Fairbanks, increasing to 38 km under the Alaska Range. *Clark and Silver (1991)* investigated the depth to Moho for several RSTN and DWWSSN stations by modeling the P and S waveforms from teleseismic earthquakes. COL was among the seven stations used in their study. They found that the seismograms recorded at station COL were complicated. In spite of this complexity, the depth to Moho beneath COL was consistently determined to be about 30 km. *Beaudoin et al. (1992)* suggested that the YTT is composed of a thin silicic upper crust (10 km) underlain by a flysch layer containing discontinuous sub-horizontal reflectors followed by a higher velocity (P-wave velocity 7.0-7.2 km/s) unit. These conclusions were based on the data from one of three 130 km long refraction/wide-angle reflection profiles that were collected in 1987 and stretched across the entire YTT from south to north. This study was a part of the Trans-Alaska Crustal Transect (TACT) program initiated in 1984 by the U.S.G.S. as a multidisciplinary study of the composition and evolution of the Alaskan crust along the Trans-Alaska pipeline from Valdez to Prudhoe Bay (*Beaudoin et al., 1992*). TACT results place Moho at about 30 km under Fairbanks. It was also found that the Moho reflection (PmP) varied greatly in character beneath the profile suggesting that the Moho transition in this area is laterally heterogeneous (*Beaudoin et al., 1992*). The results of *Beaudoin et al. (1992)* agree well with magnetotelluric surveys of the area that were also part of the TACT program (*Stanley et al., 1990; Labson et al., 1988; Sampson, 1992*). The interpretation of the results of these studies was that the deeper crust of the YTT had been tectonically eroded and then underplated by Mesozoic flysch and possibly underthrust by portions of Wrangelia. This model is supported by the

existence of a triangular-shaped suture zone that lies between the Denali Fault and the next major terrane to the south, Wrangellia. This zone is composed of deformed Mesozoic flysch and slivers of terranes of unknown origin (*Coney et al., 1980; Jones et al., 1982*) and is believed to represent a collapsed oceanic basin that formed prior to the collision of the Talkeetna superterrane (an amalgamation of the Wrangellia, Peninsular and Alexander terranes) to the south (*Coney et al., 1980*).

To investigate the velocity structure beneath COL, a time-domain inversion of radial receiver functions was performed using the methods discussed by *Owens (1984)*. Forward modeling of the receiver functions was then attempted to better constrain the velocity structure and to attempt to investigate non-horizontal boundaries. Receiver functions have been successfully used to investigate the deep crustal structure in a variety of tectonic settings (*Langston, 1979; Owens 1984; Owens et al., 1984; Cassidy and Ellis, 1993; Mangino et al., 1993*). This study is motivated by the desire to determine the details of the deep crustal structure and thereby gain some insight to the physical processes that occur during collision, subsequent accretion, and the very large scale underthrusting that appears to have taken place.

We use P-waveforms from earthquakes at distances between 26° and 92° recorded by intermediate period instruments at station COL. A total of 57 earthquakes occurring between February 1982 and November 1985 were used in the final inversions. Events were limited to those having magnitudes between 4.6 and 7.0. Due to the large number of available data, data selection could be limited to events having simple sources and high signal-to-noise ratios.

3.3. Determination and Inversion of the Receiver Functions

We isolated the receiver functions using the method of *Langston (1979)* and *Ammon (1991)*. Once isolated, the receiver functions were grouped according to similar back-azimuth and distances. Receiver functions from a single back-azimuth and distance range were stacked to increase the signal-to-noise ratio and decrease the effects of scattering in the upper crust. A semblance test was used to determine the suitability of stacking for individual traces and to provide a guide to the back-azimuth and distance range for the stacks. Semblance is a time-domain coherence measure that has the property of being sensitive to amplitude variation. The semblance is given by (*Neidell and Taner, 1971*):

$$S = \frac{1}{2} + \frac{R_{12}(0)}{R_{11}(0) + R_{22}(0)}$$

where R_{12} is the cross correlation of an individual trace with the stack. R_{11} is the autocorrelation for the stack and R_{22} is the autocorrelation for the individual trace. The semblance ranges between 0 and 1, a semblance of 0 indicating no waveform match and a semblance of 1 being a perfect match. The direct P arrivals have the largest amplitude of any peak in the receiver functions and are always correlated in time from one trace to another. In order to keep the semblance calculations from being dominated by the direct P arrival, the calculations were performed using the waveform following the direct P.

The stack was first computed using all of the unweighted receiver functions within

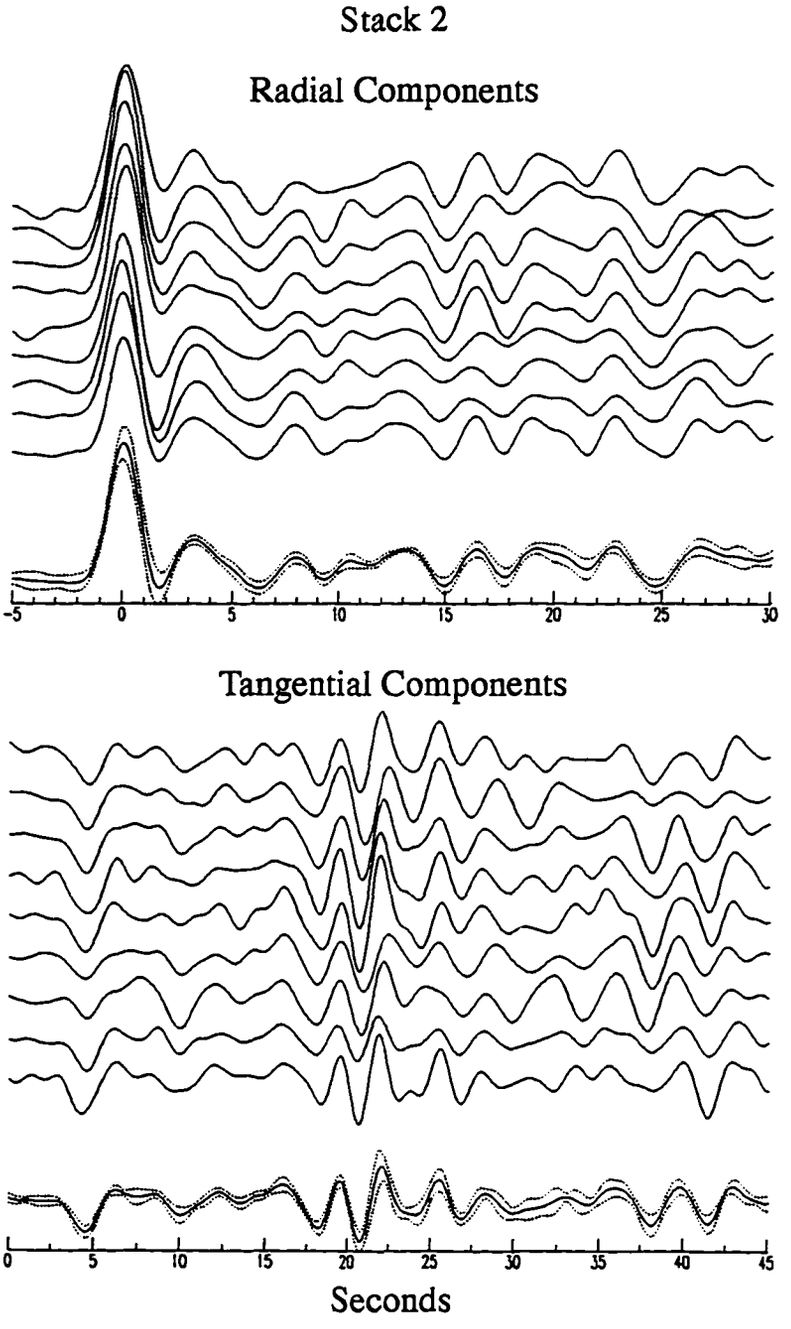

Fig. 3.2: Radial and tangential receiver functions that constitute stack 2 are shown. The resulting stacks and ± 1 standard deviation bounds (dashed traces) are shown following the receiver functions. The tangential receiver functions for this stack show strong coherency which is indicative of off-azimuth energy.

TABLE 3.1: List of Receiver Function Stacks for COL

stack	back-azimuth range	distance range	# in stack	semblance range
1	268 - 274	26 - 41	7	0.79 - 0.93
2	269 - 278	51 - 59	9	0.89 - 0.97
3	203 - 209	82 - 89	6	0.86 - 0.95
4a	224 - 231	83 - 86	4	0.87 - 0.93
4b	239 - 242	82 - 83	5	0.84 - 0.91
5	277 - 297	63 - 77	6	0.83 - 0.95
6	273 - 277	44 - 47	5	0.79 - 0.96
8	326 - 352	63 - 93	6	0.87 - 0.95
9	90 - 116	63 - 93	7	0.87 - 0.95

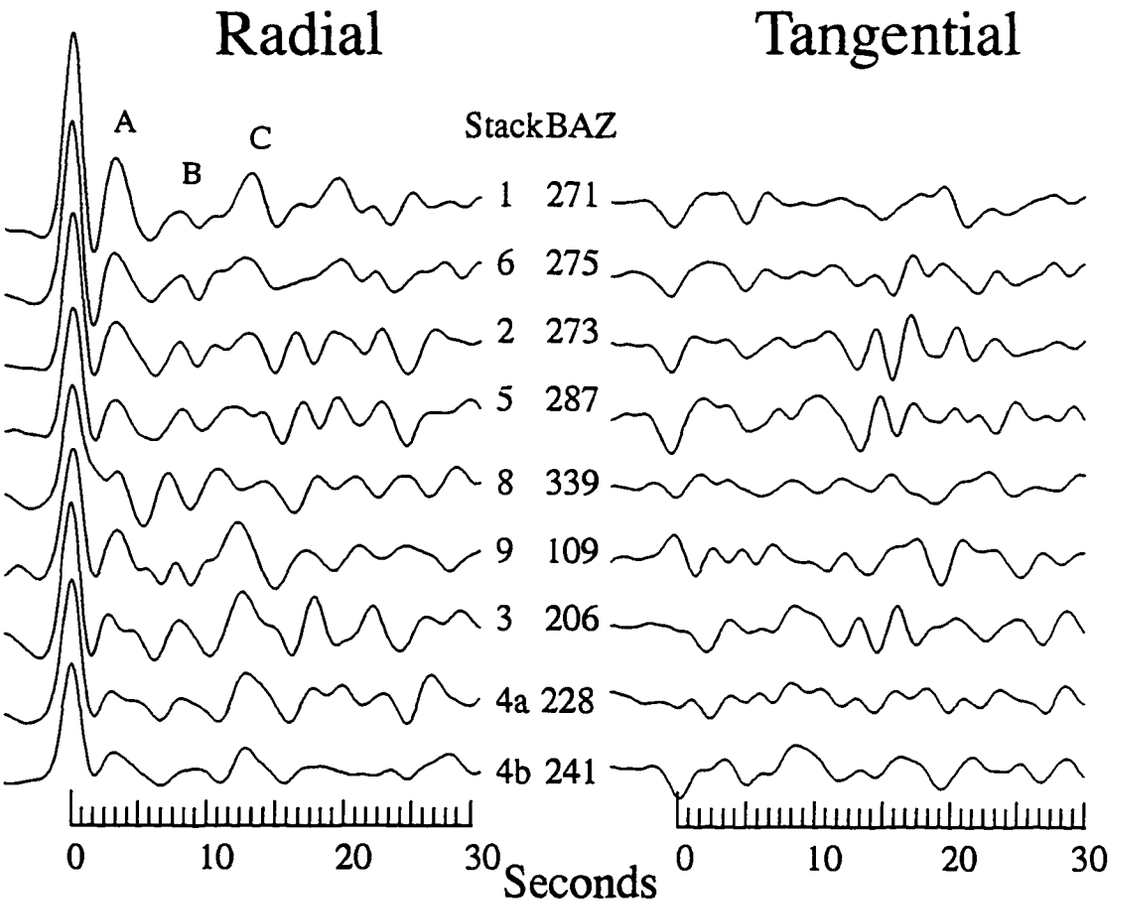

Fig. 3.3: Receiver functions for all stacks (clockwise from west). Radial receiver functions are shown on the left and the tangential receiver functions on the right. Labels A, B, and C indicate consistent phases. BAZ is the average back azimuth for the stack.

a given back-azimuth, distance range. The semblance of each receiver function was then calculated with respect to the stacked trace. Individual receiver functions with low semblances were then rejected and the remaining traces were restacked. This process was repeated until a stable stack existed. In practice, the first stack was formed from events in a broad back-azimuth, distance range (perhaps a quadrant), but after a few iterations it would become apparent that two or three stacks were required. Typically, semblances calculated for receiver functions in an initial stack would cluster together in value with the exception of one or two receiver functions falling well below the others. For example, the initial stack 2 had 16 traces with semblance values that ranged from 0.79 to 0.96 and two traces with semblance values of 0.62 and 0.70. These outliers were the traces that were rejected. In some cases outliers were found to fit better in a in nearby stack. The lowest semblance computed for any given trace used in the final inversion was 0.79 and the highest semblance was 0.97.

A total of nine stacks were used with 4 - 9 receiver functions in a given stack. Only one stack exists at an eastern azimuth due to a fewer number of earthquakes in our data set coming from that back-azimuth. Figure 3.2 shows the receiver functions that were selected for stack 2 as well as the stack they produced. The final stacks are listed in table 3.1. The variance is calculated during the stacking process and from this the ± 1 standard deviation bounds are calculated for the stack. All of the stacked receiver functions are displayed in figure 3.3.

The receiver functions were inverted using the methods outlined in *Ammon et al. (1990)*. In this process a smoothness trade-off parameter is used (*Ammon et al., 1990*).

The function of this parameter is to allow for a stable inversion and has the effect of minimizing the roughness in the model. An obvious result of using this parameter in the inversion process is to smooth out sharp velocity contrasts. Therefore we can, at best hope to model such contrasts as a velocity gradient. For this study a smoothness trade-off parameter of 0.3 was used.

The model parameterization in the inversion is limited to that of a horizontally layered model. Following this assumption, arrivals in the radial receiver function represent P to S wave conversions and reflections due to the earth structure. Another result of this assumption is that the tangential waveform should vanish. Coherent energy appearing on the stacked tangential waveforms represents the presence of off-azimuth energy that may be produced by non-horizontal structure, path effects, or anisotropy.

3.4. Receiver Functions

All of the tangential components of the receiver functions display high amplitudes. These amplitudes sometimes approach or even exceed the amplitudes of corresponding arrivals on the radial component. Such strong coherent arrivals on the tangential components indicate that the crustal structure beneath station COL deviates from simple horizontal layering and thus complicates the interpretation of the radial component arrivals. In spite of this observation, there is a remarkable similarity of the radial receiver functions regardless of back-azimuth and these consistent arrivals may be modelled.

Three arrivals consistently appear on all the radial receiver functions. These peaks

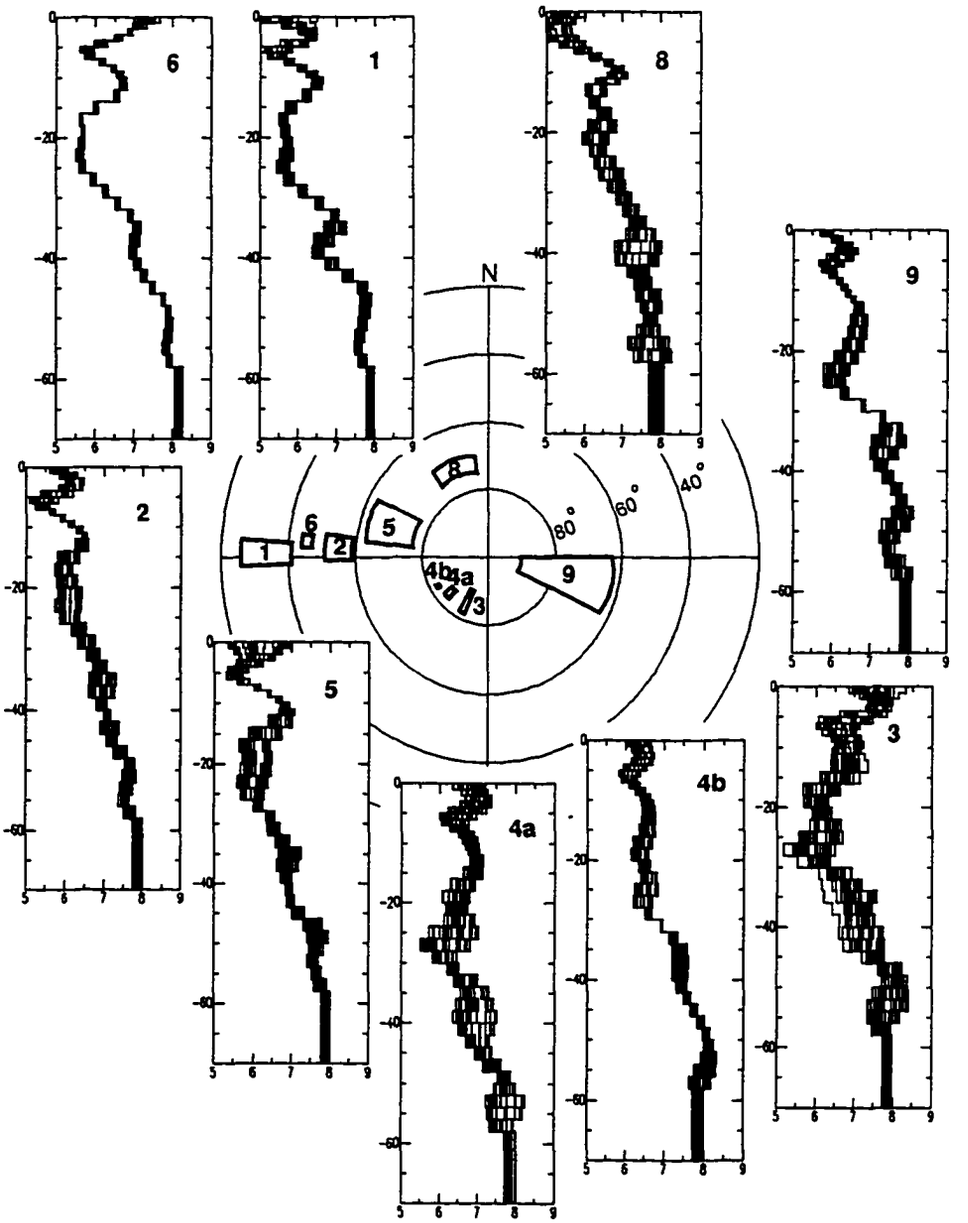

Fig. 3.4: Stereographic plot showing the locations of all the stacks and the inversion model produced for those stacks. Concentric circles on the stereographic plot represent distances in degrees. The vertical axis on individual model plots represents depth in kilometers, the horizontal axis represents p-wave velocity in kilometers per second. Bold faced numbers on both the model plots and stereograph are the stack numbers. There is a systematic increase in velocity attained by the gradient at ~32 km in the models as the back azimuth is changed from east to west.

are denoted as A, B, and C in figure 3. Peak A is interpreted as consisting mostly of energy from the P to S conversion at Moho (Ps) and peak C as a multiple from this same boundary. Peak B appears to be the result of a conversion from an intermediate layer. These peaks arrive approximately 3 seconds, 8 seconds, and between 10 and 15 seconds after the zero-lag peak. Peak B is typically of lower amplitude than peaks A or C. A trio of phases consistently arrive after peak C, between 15 and 20 seconds, however, strong coherent energy exists on the tangential components at this time interval so interpreting these arrivals is not straight forward.

Stack 8 consists of data from more northern back-azimuths. For this stack, Peak A is not as strongly defined and the receiver function has an overall ringing appearance that suggests complications possibly due to scattering. Arrivals from the east are contained in stack 9. Additional arrivals appear on this stack in the form of side lobes on peak A and peak C. In all cases the side lobes were not considered to be important features in the modeling process. Stacks 5, 8, 9, 3, 4a, and 4b contain receiver functions from similar distance ranges but change in back azimuth. There is a slight systematic move out of peak C with changing back-azimuth. There is also a systematic change in polarity and amplitude for the zero-lag arrival on the tangential components for these stacks (figure 3.3). These two observations provide some evidence for a dipping structure beneath station COL.

3.5. Inversion Results

The inversion results also show a great deal of consistency between stacks from different back-azimuths. We show the velocity models produced by the inversions in

figure 3.4. There appears to be a high-velocity layer (6.5 km/s) between depths of 10 km and 15 km. The results from all stacks contain an area of constant velocity between depths of 15 and 25 km. The models clearly show two regions of velocity increase below the region of constant velocity. The first gradient ranges in depth between 27 and 32 km and for the western back azimuths typically reaches a P wave velocity of 7.0 km/s. The model from the eastern back azimuth reaches a P wave velocity of 8.0 km/s in the first velocity increase. The second velocity gradient is located between 42 and 46 km. The western models reach a velocity of 8.0 km/s at the bottom of this feature. The models show a systematic increase in the velocity attained by the first gradient as the azimuth changes from west to east.

3.6. Forward Modeling

The receiver functions were forward modeled to extract details of the lateral velocity variations beneath station COL. In particular, we were interested in investigating the possibility of a dipping Moho. The forward modeling was performed by using a trial and error method to find a best fit to the stacked receiver functions. The depth, velocity contrast, strike and dip of planar dipping structures were varied to find the best fits to the data. Synthetic seismograms were computed using a ray-tracing code written by T. J. Owens and described in *Langston (1977)*. Synthetic receiver functions were then computed by the same process used for the data.

Due to the inherent nonuniqueness in modeling and the trade-off between layer velocity and depth, *a priori* information on the velocity structure is essential. Velocity and

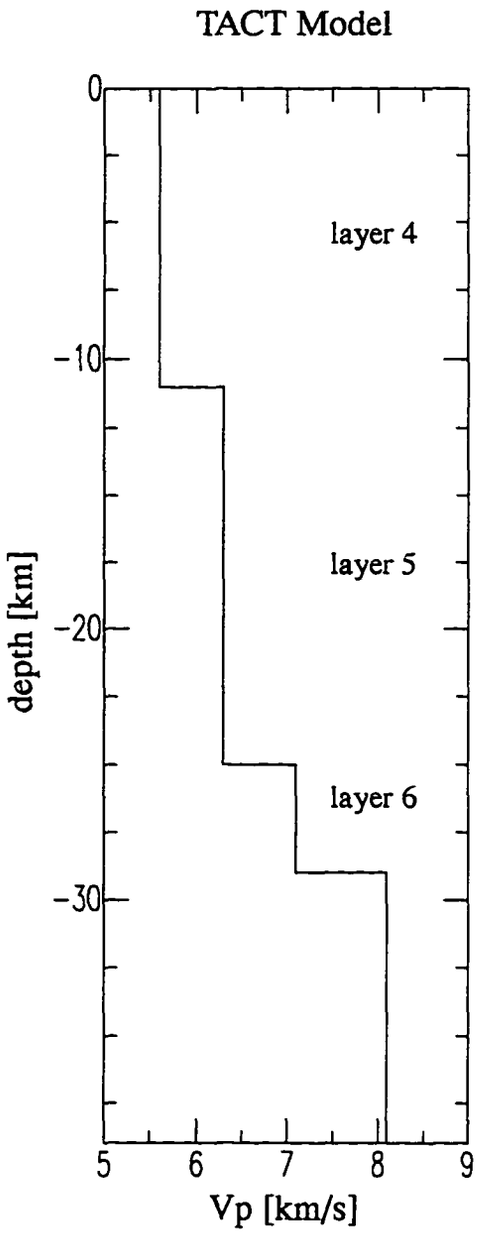

Fig. 3.5: Velocity model for station COL inferred from *Beaudoin et al. (1992)*. Layers are labelled to correspond with their interpretation. Layer 5 is interpreted to represent Mesozoic flysch.

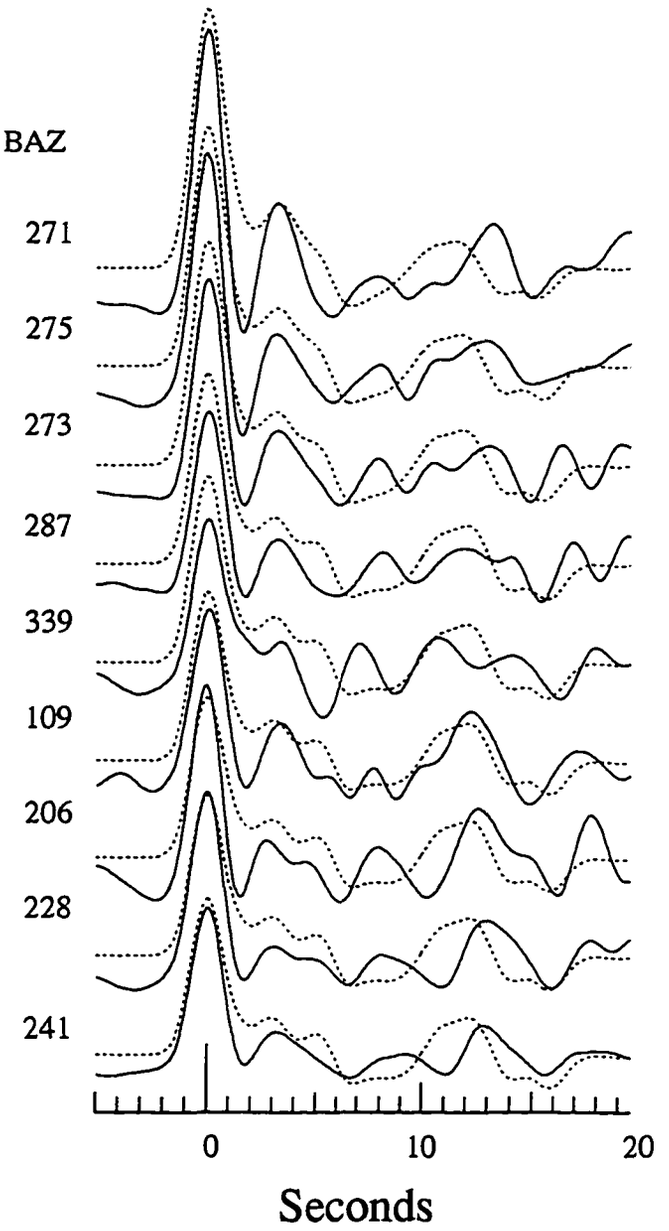

Fig. 3.6: Synthetic receiver functions produced by the TACT model (dashed trace) compared to the observed stacked receiver functions (solid trace).

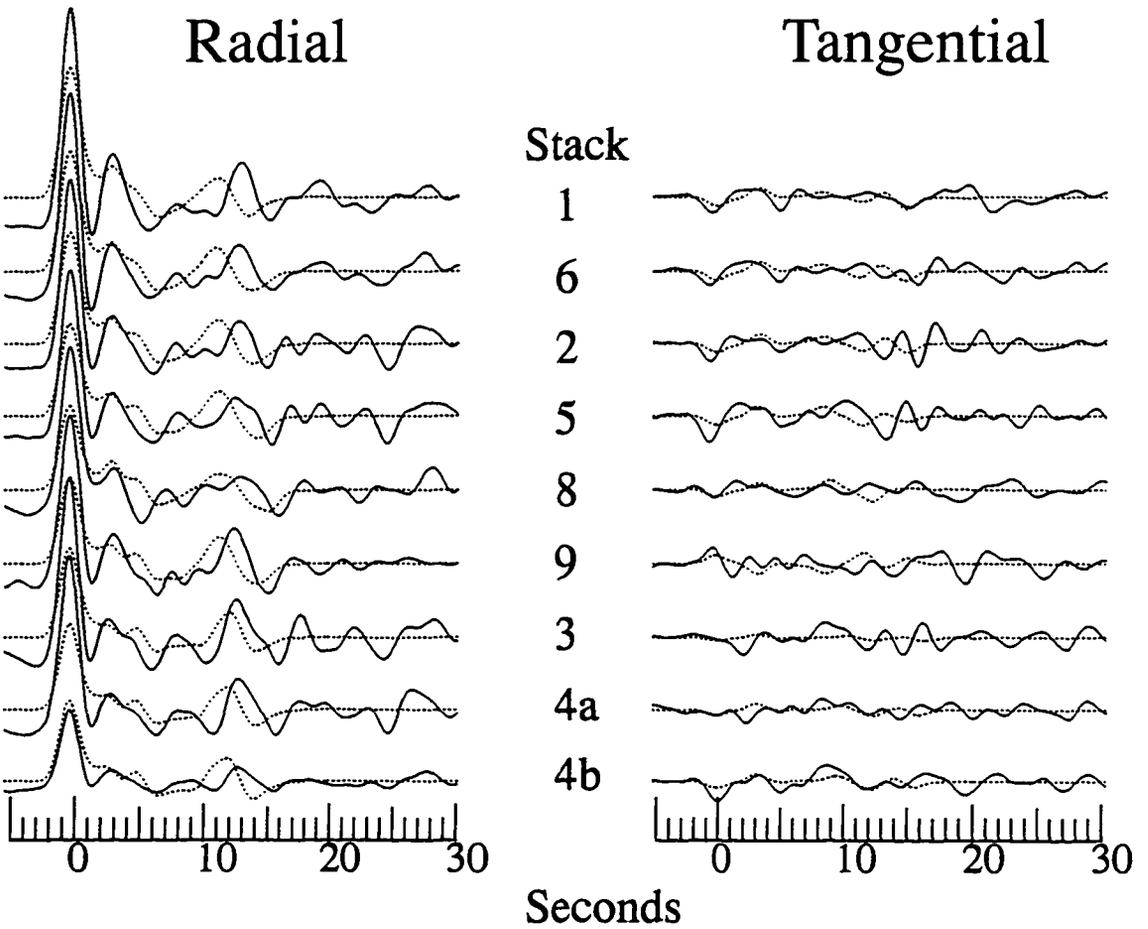

Fig. 3.7: Synthetic receiver functions produced by the TACT model with Moho dipping at 10° to the northeasta (strike 280°) compared to the observed stacked receiver functions.

depth information from the TACT profile results were used as a starting point in the forward modeling (*Beaudoin et al., 1992*). Furthermore, one of the constraints used in the forward modeling process was to try and keep the velocity model as close to well-constrained features in the TACT results as possible. The Poisson's ratios for the layers were also taken from TACT results and not varied due to the complicated nature of the model.

In figure 3.5 we show the TACT velocity model, taken from the northern most end of the south Fairbanks deployment (*Beaudoin et al., 1992*). The layers are labelled to correspond with those in the TACT model. In the TACT study, Poisson's ratio from the surface to a depth of 27.0 km was found to be 0.23 and below this depth, 0.25. In figure 3.6 we show the receiver functions generated for this model compared to the observed receiver functions. The observed receiver function arrivals show a slight shift in time for the Moho multiples with changing back-azimuth, most noticeable in peak C. There is also a systematic change in the polarity of the direct arrival on the tangential components for the same stacks. These observations suggest that the Moho in this area may be modeled as a planar dipping structure (*Langston, 1977*). The tangential polarities suggest that the Moho strikes between 235° and 320°, and dips to the north. In figure 3.7 we compare the radial and tangential receiver functions produced for the TACT velocity model in which Moho is striking 280° and dipping 10° to the north with the observed radial and tangential receiver functions.

The observed receiver functions show an arrival not present on the synthetics produced by the TACT model (peak B). This arrival may be modeled by inserting a low-velocity layer into the model. The models in the inversion results do not vary greatly from

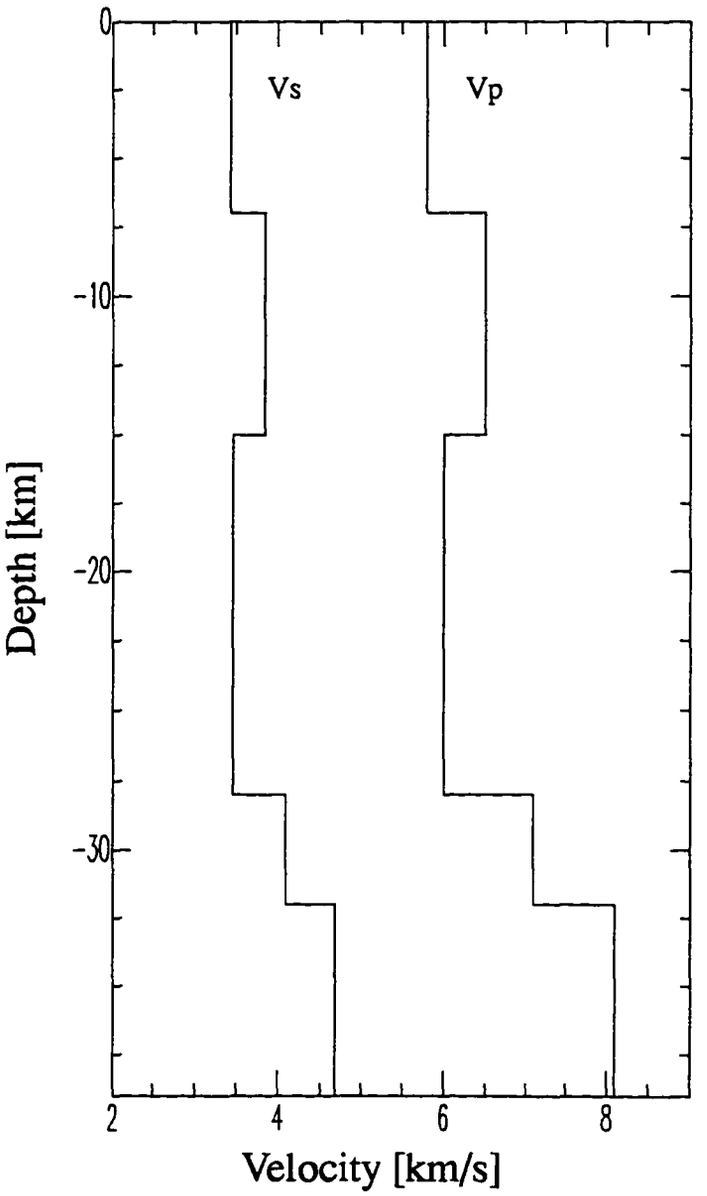

Fig. 3.8: Final velocity model. The gradients at depths of 28 km and 32 km are modeled as dipping 10° to the northeast (strike 280°).

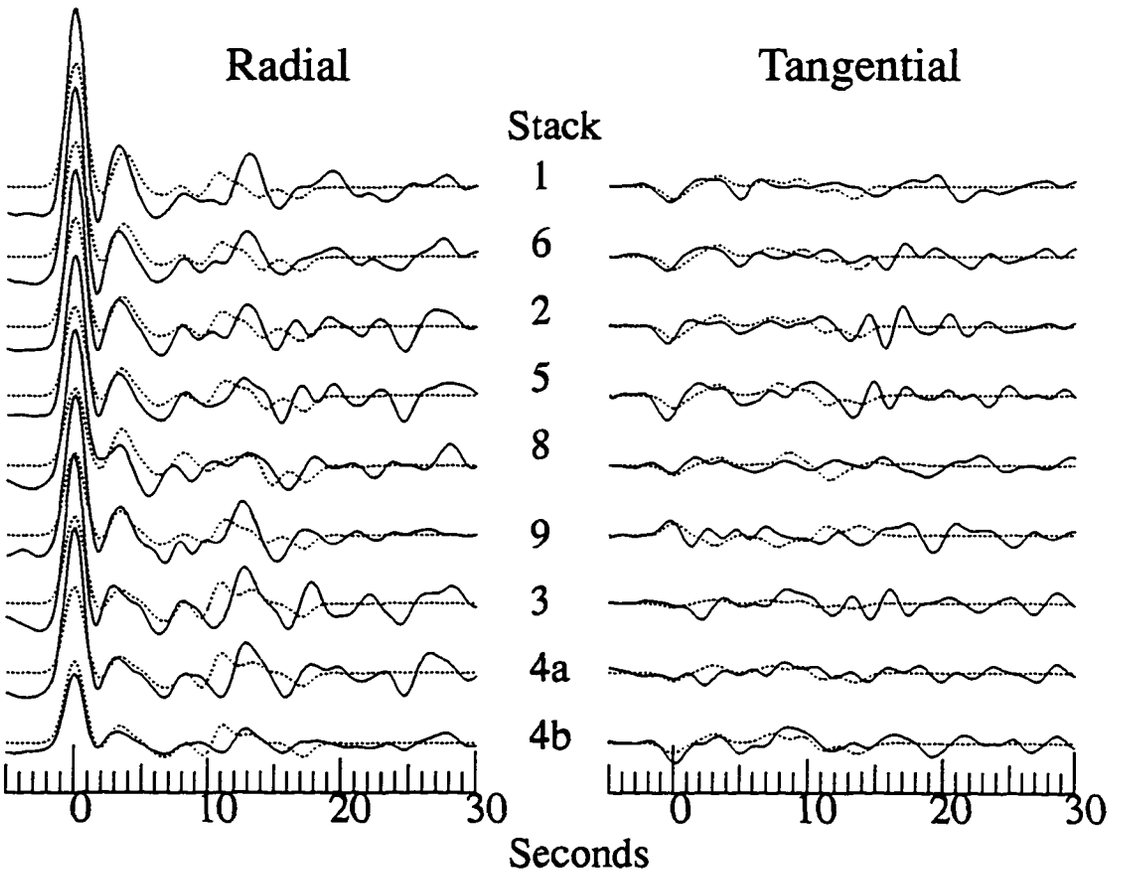

Fig. 3.9: Synthetic receiver functions produced by the final model (dashed trace) compared to the observed stacked receiver functions.

the TACT model with the exception of just such a low velocity-layer. Other velocity models were tried in an attempt to produce this arrival, however these models were not consistent with the TACT results or our inversion models. For the final model an average structure from the inversion results is used with the interfaces at 28 km and 32 km depths and having a strike of 280° and a dip of 10° to the north. Both interfaces were allowed to dip because we believe they represent a crust-mantle transition zone. In figure 3.8 we show the depths and velocities of the layers in the final model. The synthetic waveforms produced by this model are shown in figure 3.9.

3.7. Discussion

The placement of Moho at about 30 km in previous studies indicate that the Moho corresponds to the first gradient in our models. The fact that for the western models this first gradient does not reach the expected mantle velocity may indicate that energy was lost from the radial component to the tangential component. Such off-azimuth energy may be generated by dipping layers or other structural complication. The tangential receiver functions show a systematic change in polarity that is consistent with Moho dipping to the north by at least 10°. The receiver function models indicate a depth of about 32 km for Moho which is consistent with the earlier studies.

Hanson et al. (1968) and also *Woolard* et al. (1960) found that Moho dipped to the south under the Alaska range. This result apparently conflicts with our results which indicate that Moho dips to the north. A possible explanation for this conflict is that the Moho in the area may exhibit a large depth variation due to the collision and interaction of the

terranes. Such a depth variation was not considered in the earlier studies. A laterally heterogeneous crust-mantle transition has been suggested by *Beaudoin et al. (1992).*

The area of constant velocity between depths of 15 and 28 km found in the inversion results is roughly consistent with the results of a magnetotelluric study by *Stanley et al. (1990).* In this study a high conductivity unit was found between depths of about 10 km and 20 km. The refraction-reflection results of *Beaudoin et al. (1992)* indicated the existence of laterally discontinuous reflectors in this layer. Based on these studies this unit has been interpreted as underplated Mesozoic flysch (*Beaudoin et al., 1992; Stanley et al., 1990*). An intermediate peak (peak B) can be modeled by inserting a low velocity layer into the TACT model. This low-velocity layer could be interpreted to represent the layer of Mesozoic flysch found in the earlier studies.

The receiver functions exhibit later arrivals that are interpreted in the inversions as sub-Moho structure. While such structure is consistent with tectonic models of this area (underthrust Wrangellia, for example), these arrivals are somewhat suspect because strong coherent energy exists on the corresponding tangential components. Because of this, no attempt was made to forward model these arrivals.

The receiver functions recorded at COL are complex. The polarities of the first peak in the tangential waveforms and the move-out in peak C of the radial waveform are both consistent with dipping structure. S-wave anisotropy has been recognized as another possible cause of complexity in receiver functions (*McNamara and Owens, 1993*). While splitting from S-wave anisotropy has been observed beneath this area (*Silver and Chan, 1991*), it is believed to have its likely source in the mantle rather than the crust. Neverthe-

less the possibility that some of the complexity seen in the receiver functions at COL is due to crustal anisotropy can not be ruled out.

3.8. Conclusions

Receiver functions isolated from seismograms recorded at station COL in Fairbanks, Alaska were modeled to estimate the velocity structure. The existence of large amplitude, coherent arrivals on the tangential component of the receiver functions attest to structural complexity beneath station COL. The inversion and forward modeling results indicate that the depth of Moho is about 32 km which is consistent with previous studies (*Beaudoin et al., 1992; Hanson et al., 1968; Woolard et al. 1960*). Forward modeling of the receiver functions suggests that the Moho dips to the north at an angle of at least 10°. A low-velocity zone is found at depths between 15 km and 28 km that may correspond to the layers interpreted as being underplated Mesozoic flysch, identified in previous studies (*Beaudoin et al., 1992; Stanley et al., 1990; Labson et al., 1988*).

Chapter 3 References

Ammon, C. J., G. E. Randall, and G. Zandt, On the non-uniqueness of receiver function inversions, *J. Geophys. Res.*, *95*, 15,303-15,318, 1990.

Ammon, C. J. , The isolation of receiver effects from teleseismic P waveforms, *Bull. Seismol. Soc. Am.*, *81*, 2504-2510, 1991.

Beaudoin, B. C., G. S. Fuis, W. D. Mooney, W. J. Nokleberg, and N. I. Christensen, Thin, low-velocity crust beneath the southern Yukon-Tanana terrane, east central Alaska: results from Trans-Alaska Crustal Transect refraction/wide-angle reflection data, *J. Geophys. Res.*, *97*, 1921-1942, 1992.

Cassidy, J. F. and R. M. Ellis, S-wave velocity structure of the northern Cascadia subduction zone, *J. Geophys. Res.*, *98*, 4407-4421, 1993.

Churkin, M., Jr., C. Carter, and J. H. Trexler, Jr., Collision-deformed Paleozoic continental margin of Alaska-foundation for microplate accretion, *Geol. Soc. Am. Bull.*, *91*, 648-654, 1980.

Churkin, M., Jr., H. L. Foster, R. M. Chapman, and F. R. Weber, Terranes and suture zones in east central Alaska, *J. Geophys. Res.*, *87*, 3718-3730, 1982.

Clark, T. J. and P. G. Silver, A procedure for the systematic interpretation of body wave seismograms-I. Application to Moho depth and crustal properties, *Geophys. J. Int.*, *104*, 41-72, 1991.

Coney, P. J., D. L. Jones, and J. W. H. Monger, Cordilleran suspect terranes, *Nature*, *288*, 329-333, 1980.

Dusel-Bacon, C. and J. N. Aleinikoff, Petrology and tectonic significance of augen gneiss from a belt of Mississippian granitoids in the Yukon-Tanana terrane, east-central Alaska, *Geol. Soc. Am. Bull.*, *96*, 411-425, 1985.

Hanson, K., E. Berg, and L. Gedney, A seismic refraction profile and crustal structure in central interior Alaska, *Bull. Seismol. Soc. Am.*, *58*, 1657-1665, 1968.

Jones, D. L., N. J. Silberling, W. Gilbert, and P. Coney, Character, distribution, and tectonic significance of accretionary terranes in the central Alaska Range, *J. Geophys. Res.*, *87*, 3709-3717, 1982.

Labson, V. F., M. A. Fisher, and W. J. Nokleberg, An integrated study of the Denali Fault from magnetotelluric sounding, seismic reflection, and geologic mapping, (abstract), *Eos*, *69*, 1457, 1988.

Langston, C. A., The effect of planar dipping structure on source and receiver responses for constant ray parameter, *Bull. Seismol. Soc. Am.*, *67*, 1029-1050, 1977.

Langston, C. A., Structure under Mount Rainier, Washington, inferred from teleseismic body waves, *J. Geophys. Res.*, *84*, 4749-4762, 1979.

Mangino, S. G., G. Zandt, and C. J. Ammon, The receiver structure beneath Mina, Nevada, *Bull. Seismol. Soc. Am.*, *83*, 542-560, 1993.

McNamara, D. E. and T. J. Owens, Azimuthal shear wave velocity anisotropy in the Basin and Range Province using Moho Ps converted phases, *J. Geophys. Res.*, *98*, 12,003-12,017, 1993.

Mortensen, J. K., and G. A. Jilson, Evolution of the Yukon-Tanana terrane: evidence from southeastern Yukon Territory, *Geology*, *13*, 806-810, 1985.

Neidell, N. S., and T. Taner, Semblance and other coherency measures for multichannel data, *Geophysics, 36*, 482-497, 1971.

Owens, T. J. , *Determination of crustal and upper mantle structure from analysis of broad-band teleseismic P-waveforms*, Ph. D. dissertation, 146 pp., Univ. of Utah, 1984.

Owens, T. J., G. Zandt, and S. R. Taylor, Seismic evidence for an ancient rift beneath the Cumberland Plateau, Tennessee: A detailed analysis of broadband teleseismic P-waveforms, *J. Geophys. Res., 89*, 7783-7795, 1984.

Sampson, J. A., V. F. Labson, and C. L. Long, Electrical resistivity cross sections in east-central Alaska, in *Geologic studies in Alaska by the U. S. Geological Survey, 1990*, D. Bradley and A. Ford, Editors, *U. S. Geol. Surv. Bull. 1999*, 1992.

Silver, P. G., and W. W. Chan, Shear wave splitting and subcontinental mantle deformation, *J. Geophys. Res., 96*, 16,429-16,454, 1991.

Stanley, W. D., V. F. Labson, W. J. Nokleberg, B. Csejtey, and M. A. Fisher, The Denali Fault system and Alaska Range of Alaska: evidence for underplated Mesozoic flysch from magnetotelluric surveys, *Geol. Soc. Am. Bull., 102*, 160-173, 1990.

Stone, D. B., B. C. Panuska, and D. R. Packer, Paleolatitudes versus time for southern Alaska, *J. Geophy. Res., 87*, 3697-3707, 1982.

Stone, D. B., and W. K. Wallace, A geologic framework of Alaska, *Episodes, 10*, 283-289, 1987.

Tempelman-Kluit, D. J., Stratigraphic and structural relations between the Selwyn basin, Pelly-Cassiar platform, and Yukon Crystalline terrane in the Pelly mountains, Yukon, *Geol. Surv. Can. paper, 77-1A*, 223-227, 1977.

Woolard, G. P., N. A. Ostenso, E. Thiel, and W. E. Bonini, Gravity anomalies, crustal structure and geology in Alaska, *J. Geophys. Res.*, *65*, 1021-1037, 1960.

CHAPTER 4

Crustal Structure and Anisotropy in the Brooks Range, Alaska[1]

4.1 Abstract

Large scale structure and anisotropy of the crust in the Brooks Range, Alaska is investigated using the analysis of receiver functions and S-wave splitting phenomena. Data consisted of teleseismic earthquakes that were recorded at four temporary three-component seismic stations located along a stretch of the Dalton highway from Coldfoot, Alaska to just north of Atigun Pass. The analysis of the receiver functions included both an inversion for S-wave velocity structure as well as forward modeling. The depth to Moho estimated by this analysis correlates well with previous studies. Moho is determined to be at a depth of approximately 34 km at the southernmost station located near Coldfoot. Depth to Moho increases northward where it appears to be greatest (~54 km) for the third station located just south of Atigun Pass and shallows slightly (~50 km) at the northernmost station near Atigun Pass. S-wave splitting observed at these four stations indicate that polarization angles and time delays between fast and slow arrivals change significantly over relatively short distances. The fast directions determined at the southernmost station correlates well with regional foliations in the local crustal fabric - a large body of regionally deformed schist. The northernmost station also shows substantial S-

1. Chapter 4 is composed of the complete text and figures from the manuscript: *Crustal Structure and Anisotropy in the Brooks Range, Alaska*, by C. Searcy, D. Christensen, and M. Savage, to be submitted to *Bull. Seismol. Soc. Am*, June, 1996.

wave splitting, however, the fast direction is nearly perpendicular to that of the southern station. Based on these observations we speculate that the source of the S-wave splitting observed at these stations is due to crustal anisotropy.

4.2 Introduction

During the summer of 1990 four temporary seismic stations were deployed in the Brooks Range of northern Alaska. These stations were more or less evenly distributed along the Dalton Highway stretching from the town of Coldfoot, Alaska on the southern flanks of the Brooks Range to Atigun Gorge on the northern edge of the Brooks Range (figure 4.1). The purpose of this deployment was to record teleseismic earthquakes ($30° \leq \Delta \leq 120°$) for analysis of receiver functions and S-wave splitting phenomena. Stations labelled BS1, BS2 and BS4 each consisted of three intermediate period seismometers (Kinemetric SV1 and SH1 sets), while the station designated as BS3 was a three-component broadband instrument (Geralp CMG-3T). Data were collected on a digital recorder (Teledyne Geotech, Portable Data Acquisition System -PDAS) placed at each station and powered by batteries and solar panels. During the eight week deployment between 25 and 80 teleseismic events were recorded at each of these stations, although only a small subset of these records were adequate for further processing. In part, the motivation for looking at this region was the existence of the Trans-Alaska Crustal Transect (TACT), a seismic reflection and refraction experiment investigating the details of the crustal structure across Alaska. The TACT project was a joint USGS/University (spearheaded by Rice University) effort to produce detailed images of the crust and upper

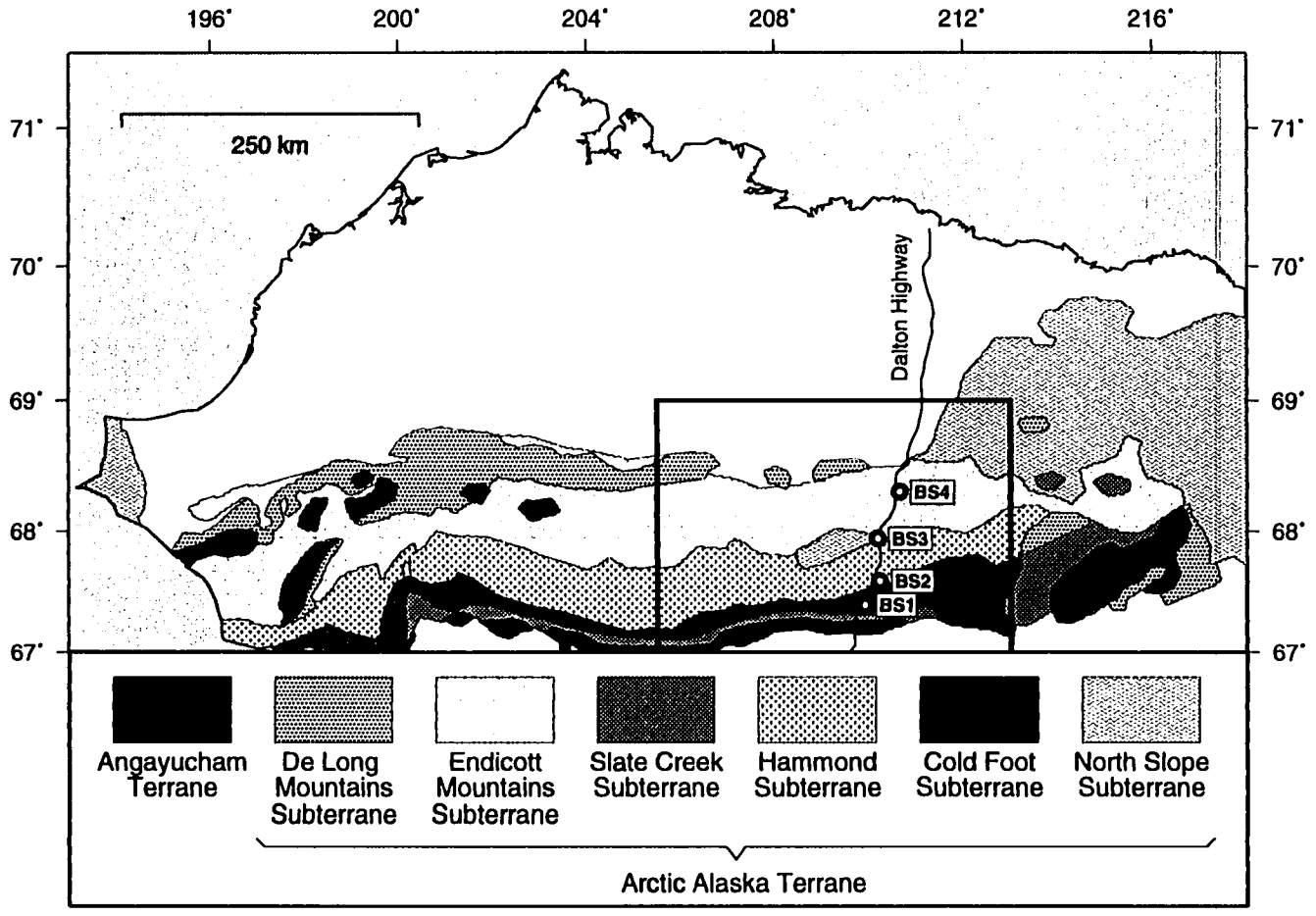

Fig. 4.1: Tectonic map showing the locations of the four temporary seismic stations in the Brooks Range (labelled BS1, BS2, BS3, BS4) at which data were collected for this study. The box indicates the borders of figure 4.9. Redrawn from *Moore and Mull (1989).*

mantle across Alaska. Results to date from this project may be found in *Fuis et al. (1995); Levander et al. (1994)*; and *Murphy et al. (1993)*. The goal of the receiver function study was to resolve the major velocity boundaries of the deep crustal structure, and in particular to determine the depth to Moho as an independent check on the TACT results. In addition to the receiver function investigation, S-wave splitting analysis was performed in order to obtain a preliminary estimate of anisotropy in the region.

The Brooks Range of Northern Alaska is a fold-and-thrust belt of late Jurassic to Cretaceous age. Uplift and deformation are believed to have been initiated by the impingement of an island arc on the northern continental margin of the Arctic Alaska (*Gottschalk, 1990*). The Brooks Range is comprised of the Arctic Alaska Terrane which is in turn composed of several subterranes distinguished by individual compositions and tectonic histories. The four stations used in this study sampled three of these subterranes. Stations BS1, BS2, and BS4 were located on the Coldfoot, Hammond and Endicott Mountains subterranes, respectively. Station BS3 resided on the 3-way juncture of the Hammond subterrane, the Endicott Mountains subterrane and a feature known as the Doonerak Fenster, which is a structural exposure of the basal North Slope subterrane. The Endicott Mountains subterrane consists of a 5-8 km thick sedimentary lens emplaced on Lisburne group limestone primarily associated with the North Slope subterrane to the north (*Fuis et al., 1995*). The Hammond and Coldfoot subterranes consist of metasedimentary and metavolcanic rocks. The Coldfoot subterrane is characterized by a schist layer (commonly referred to as the Schist Belt) extending to a depth of approximately 10 km (*Fuis et al., 1995*). The Doonerak Fenster is composed of Carbiniferous limestones of the Lis-

borne Group as well as metavolcanic basement rocks of the North Slope subterrane representing the top of a duplex structure (*Fuis et al., 1995*). Depth to Moho as determined from the TACT profiles (Fuis et al., 1995), ranges from 50 km beneath the central and northern Brooks Range to 37 km beneath the North Slope and Southern Brooks Range.

4.3 Receiver Function Analysis

Receiver functions represent P-to-S wave conversions due to crustal layers directly beneath a station. Receiver functions, therefore contain information primarily about the S-wave velocity structure in the crustal layers which they traverse. The horizontal seismograms are first rotated into the radial and tangential components. The receiver functions are then isolated from the raw data by deconvolving the vertical component seismogram from the radial and tangential component seismograms. For a more detailed explanation of receiver functions and the deconvolution process the reader is referred to *Langston (1979), Owens (1984)* and *Ammon (1991)*. For this study, analysis of the receiver functions employed both inversion techniques and forward modeling. The P-wave velocity structure is inferred from the S-wave velocity structure by assuming a Poisson's ratio of 0.25.

Due to the relatively short deployment period for the temporary stations only a small amount of high quality data were recorded. For this reason, we were able to compute receiver functions for only six to eight events at each site. For all stations, the best quality events came from the west (back azimuth range from 266° to 276°). Events from each individual site and in the back azimuth range mentioned above were stacked to

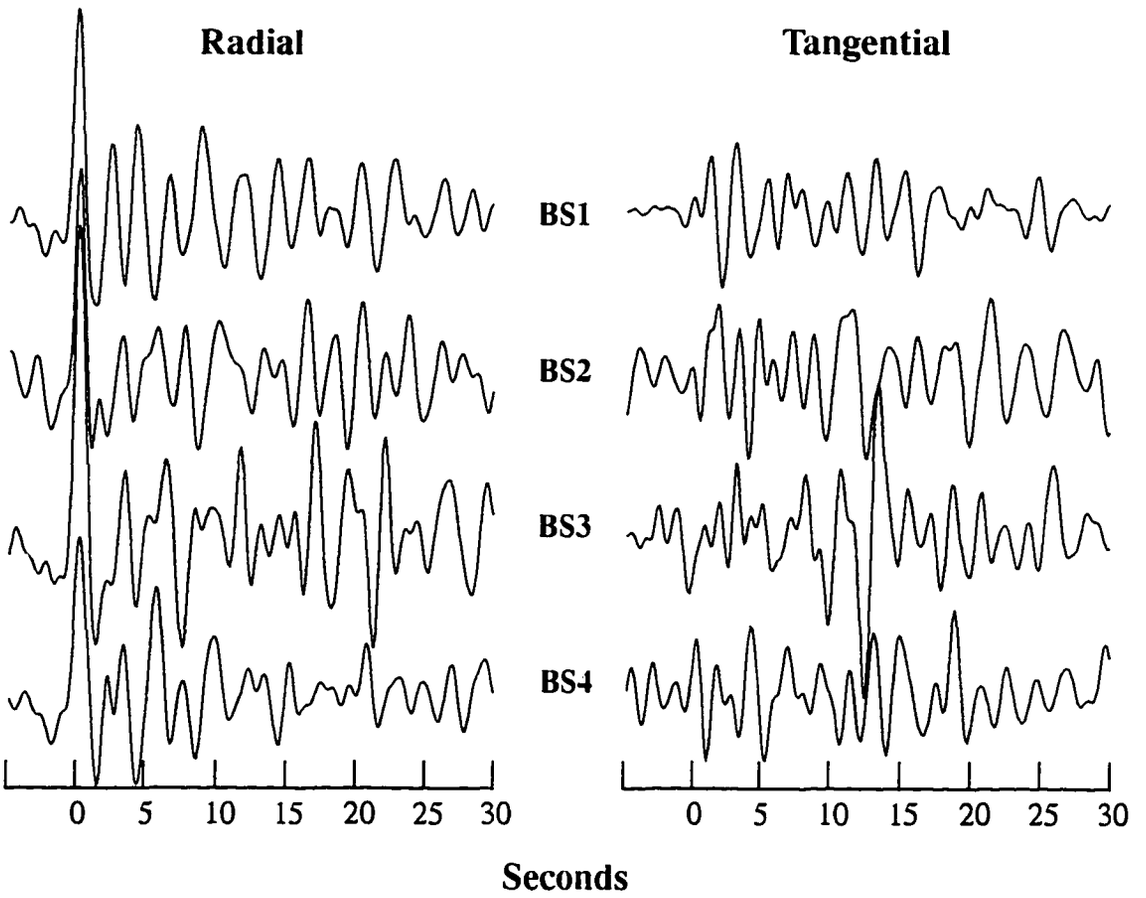

Fig. 4.2: Stacked radial and tangential receiver functions for stations BS1, BS2, BS3, and BS4. The locations of these stations are shown in figure 4.1.

increase the signal-to-noise ratio. Receiver functions determined in this study are shown in figure 4.2. Strong consistent arrivals on the tangential components of the receiver functions at each station indicate that the velocity structure in this region substantially deviates from a simple flat layered model. Because of the structural complications of the region, and the small amount of data available for this preliminary study, the goal of the receiver function analysis was to determine only very major velocity boundaries such as Moho.

The stacked radial receiver functions from each site were inverted for velocity structure using the methods of *Ammon et al. (1990)*. This inversion process uses a smoothness-trade-off parameter to stabilize the inversion and minimize roughness in the velocity model. One outcome of this inherent smoothing is that sharp velocity contrasts in the earth are commonly resolved as velocity gradients in the resulting models. Therefore, exact depths to such boundaries as well as their precise velocity contrast can only be estimated. In the inversion process, the model is parameterized as a flat layered structure. While this restriction undoubtedly introduces errors in the velocity models, we believe that prominent velocity contrasts are still resolvable in most instances. Twenty-four complete inversions were carried out for each site. Each of these inversions are performed using a starting model which is a slightly perturbed version of an initial model in order to gain a qualitative feel for the robustness of the resulting velocity models. If all twenty-four inversions yield very similar velocity models, the inversion is considered to be stable and the results well-constrained. On the other hand, if there exists a large spread in the individual models of an inversion, instability exists in the process and the results are considered ill-constrained. Receiver functions for stations BS1 and BS2 were inverted to a

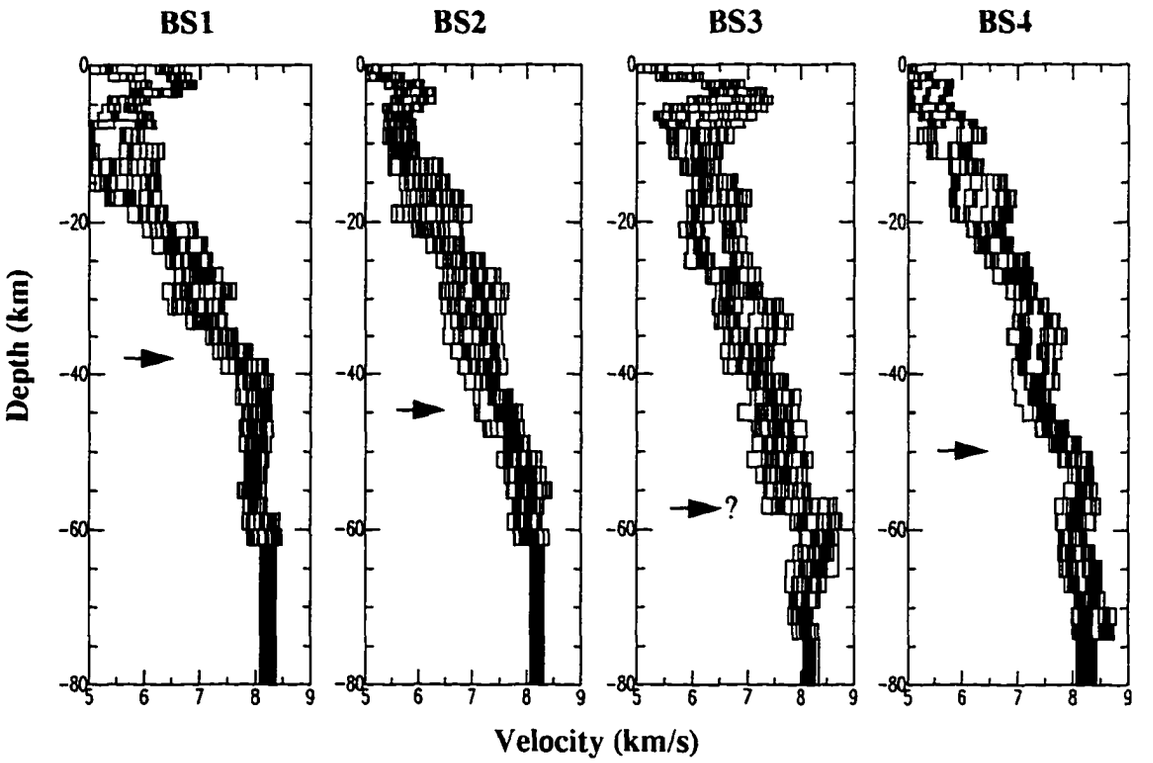

Fig. 4.3: Results of the receiver function velocity inversion. The stacked radial receiver function from each site is inverted for S-wave velocity structure. S-wave velocities are then converted to P-wave velocities assuming a Poisson's ratio of 0.25. A series of 24 inversions with different initial models were performed for each station. All 24 models resulting from these inversions are shown. Sites BS1 and BS2 were inverted to a depth of 62 km, while sites BR3 and BS4 were inverted to a depth of 74 km. Arrows indicate the interpreted depth to Moho. The inversion for station BS3 appears unstable, thus the interpretation for depth to Moho is questionable.

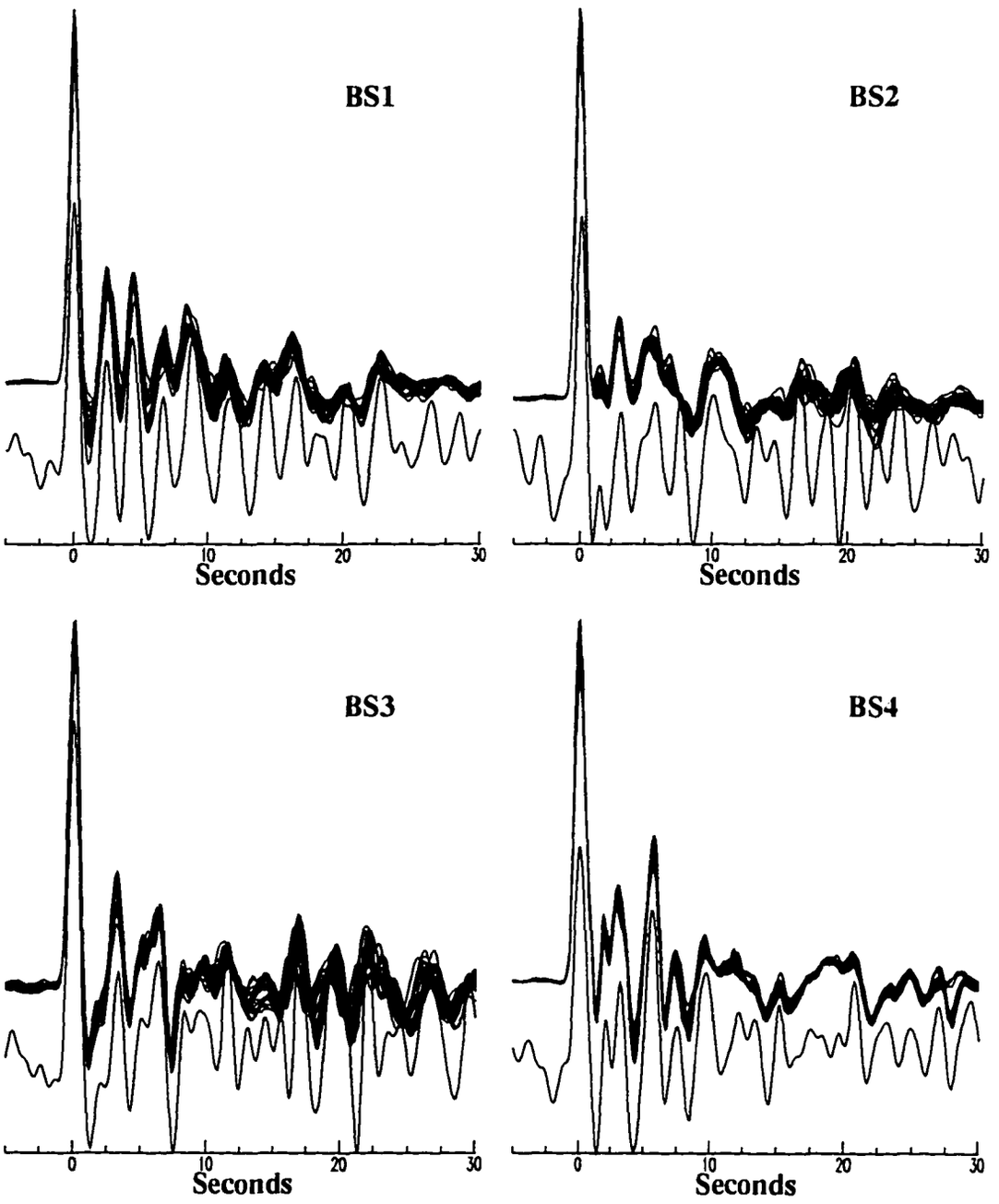

Fig. 4.4: Synthetic seismograms produced by the inversion models. The top series of traces for each site are the 24 synthetic seismograms produced from the inversion models shown in figure 4.3. The single bottom trace shown for each site is the stacked radial receiver function for that site.

depth of 62 km. For stations BS3 and BS4 it was found that better solutions were obtained if the inversions were carried out to a depth of 74 km. Inverting to deeper depths at these two sites seems justified since the depth to Moho as determined from the TACT results is deeper for BS3 and BS4. Velocity models determined for the four sites are shown in figure 4.3 and the synthetics produced from these models compared to the data are shown in figure 4.4.

Shallow velocity structure (<10 km) is poorly constrained by receiver function techniques because S-wave arrivals due to structure at these depths are usual overwhelmed by the direct P-arrival. For this reason, inversion results for structure at such depths are considered unreliable. Several consistent deep features appear in the inversion models that we believe represent interpretable structure. Station BS1 shows two regions of velocity gradients. The first occurs at a depth of about 20 km with a velocity change from ~6.0 km/sec to ~7.0 km/sec representing a boundary between a lower velocity upper crust and a higher velocity lower crust. The second occurs at a depth of about 38 km where the velocities increase from ~7.0 km/sec to ~8.0 km/sec representing the Moho discontinuity. Station BS2 also indicates two velocity gradients although less clearly than at station BS1. For station BS2 the first gradient occurs at approximately 25 km and the second at approximately 45 km. In general, seismograms recorded at station BS2 contained more noise than at any of the other three sites. This noise undoubtedly affected our ability to resolve the velocity structure from the receiver functions. The velocity models for station BS3 are poorly constrained and the solution for this site is not considered viable. The receiver functions from this site contained several consistent arrivals and it is not certain why the

inversion failed to adequately model them. There is however, a slight hint of a velocity jump at about 57 km which could indicate Moho at this location. Station BS4 again displays two prominent velocity gradients from ~6.0 km/sec to ~7.0 km/sec at a depth of ~30 km, and from ~7.0 km/sec to ~8.0 km/sec at a depth of ~50 km. These results compare well with the TACT velocity model especially for depths to Moho.

Forward modeling of the stacked receiver functions was carried out for each site to attempt to further surmise the structure of major crustal boundaries. We were particularly interested in attempting to model the receiver functions from station BS3 since inversion models for this site were so poorly constrained. Synthetic seismograms were computed using a ray-tracing code described in *Langston (1977)*. The beginning velocity model was taken from the TACT results (*Fuis et al., 1995*) and only depth to boundaries altered. It was found that depths to velocity boundaries only had to be varied slightly from those reported in the TACT results to achieve a good fit to the data. Due to the complex nature of the velocity structure in this area and the lack of arrivals from a variety of back azimuths, modeling of dipping boundaries was not attempted. The final velocity models as determined from forward modeling are shown in figure 4.5 and the synthetic receiver functions compared to the data are shown in figure 4.6. Our forward modeling suggests that depth to Moho is shallowest for station BS1 at 34 km, increases to 40 km at BS2, is deepest at BS3 with a depth of 54 km and rises to a depth of 49 km at BS4. These results compare very well with the inversion results noted above and are within about 5 km of those reported from the TACT profile (*Fuis et al. 1995*) which are approximately 37 km, 42 km, 50 km, and 50 km for BS1, BS2, BS3, and BS4 respectively.

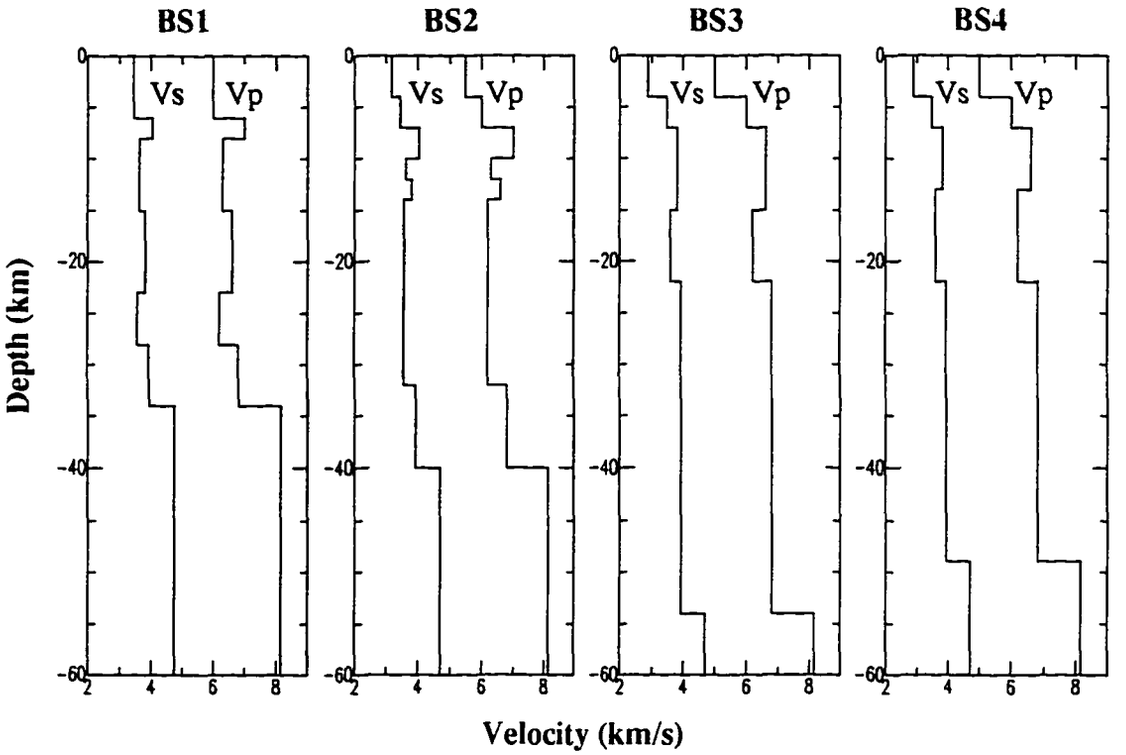

Fig. 4.5: Results of the receiver function forward modeling. The initial model for each station was taken from TACT results (*Fuis et al., 1995*) and only depth to boundaries varied.

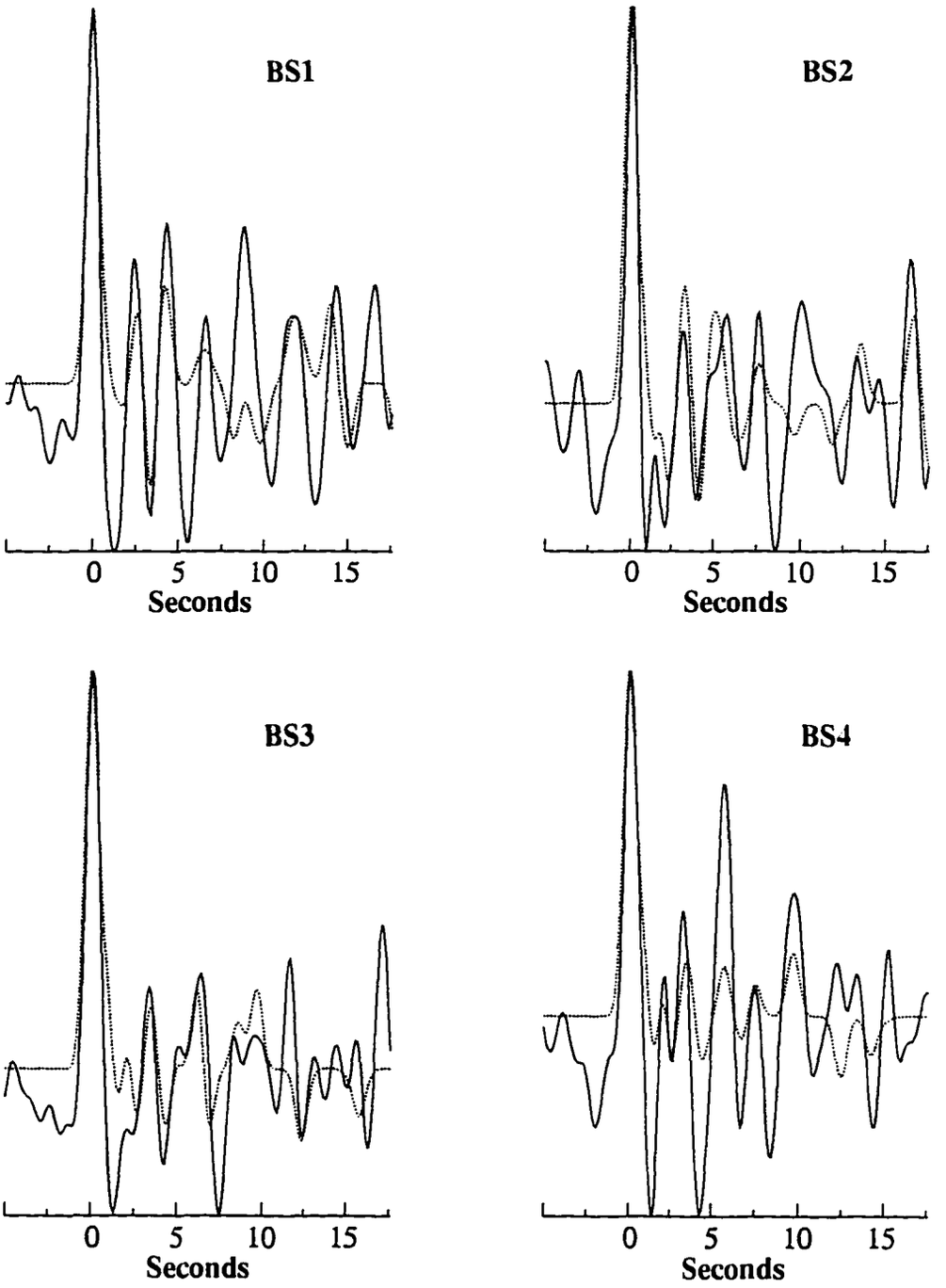

Fig. 4.6: Synthetic radial receiver functions (dashed trace) compared to observed stacked radial receiver functions for the four stations used in this study.

4.3 S-wave Splitting Analysis

When shear waves travel through an anisotropic medium they form two separate orthogonal waves, one polarized in the fast direction and the other polarized in the slow direction. Seismic anisotropy at each of the four stations was studied through S-wave splitting observations using the method of *Silver and Chan (1991)*. This method determines both the polarization angles and the delay times between fast and slow phases. Ideally, for S-wave splitting calculations, the shear waveforms need to be separated from other phases including depth phases. This restriction severely limits the useful epicentral distance ranges and depths to sources. For these studies, SKS phases are particularly useful since they have a nearly vertical travel path through the mantle in addition to a known radial polarization for the upward path. Because of the short deployment and restrictions on the waveforms used, only a few recordings could be used for S-wave splitting calculations. Nevertheless, occurrences of fairly strong S-wave splitting (from SKS phases) were recorded at three of the four stations. S-wave splitting at the southernmost station (BS1) located in the Coldfoot Subterrane was observed to have a fast direction of 61° and a delay time between the fast and slow S-wave arrivals of about 0.87 seconds. In figure 4.7, we show an example of S-wave splitting of waveforms recorded at station BS1. In this example, the rotated (fast and slow) and reconstructed SKS phase are presented. Station BS2, located about 25 km to the north of station BS1, had a similar fast direction (64°) but a delay time of only 0.4 seconds; about half of that recorded at station BS1. Station BS3, which is located just south of the crest of the Brooks Range and about 35 km to the north of station BS2, showed no, or at least inconclusive, S-wave splitting. The northern

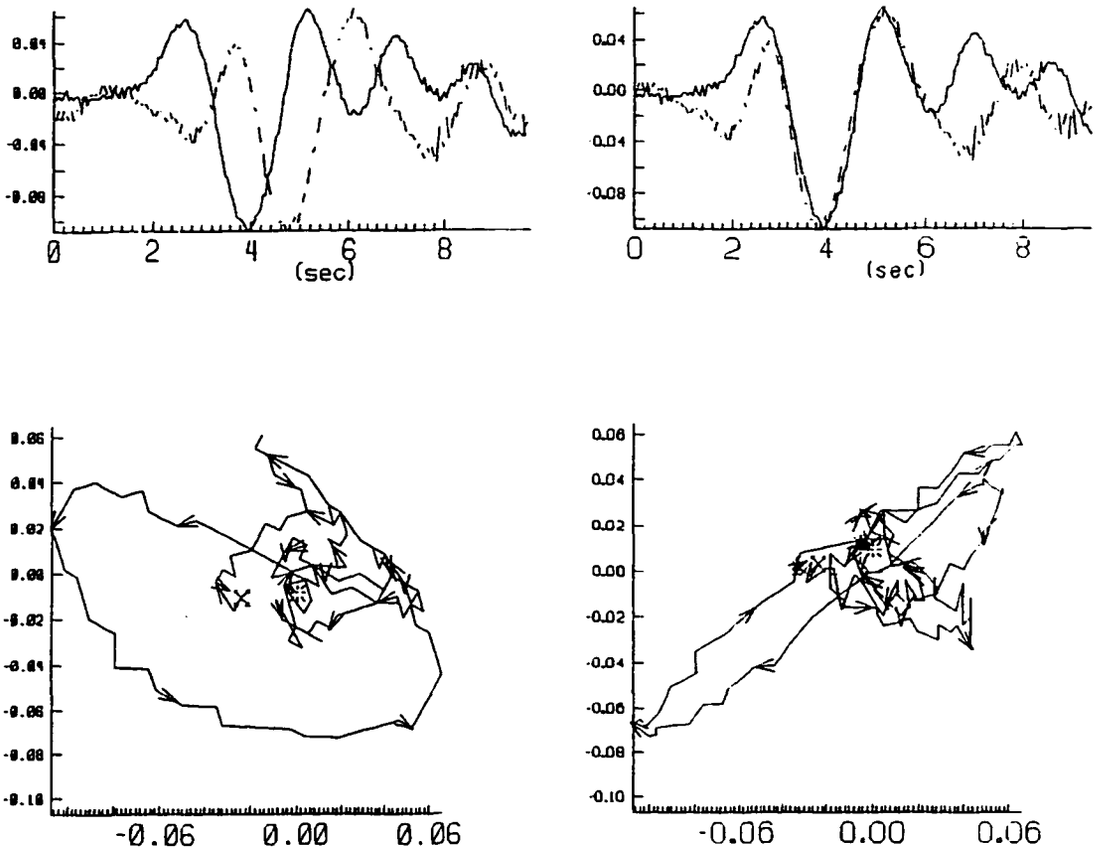

Fig. 4.7: Example of splitting for a SKS phase at station BS1, located in the Coldfoot subterrane. Top two traces show a superposition of fast and slow components uncorrected (left) and corrected (right). The bottom two plots show particle motion for the fast and slow components uncorrected (left) and corrected (right). For this example. the fast direction was found to be 61° with a delay time of 0.9 sec.

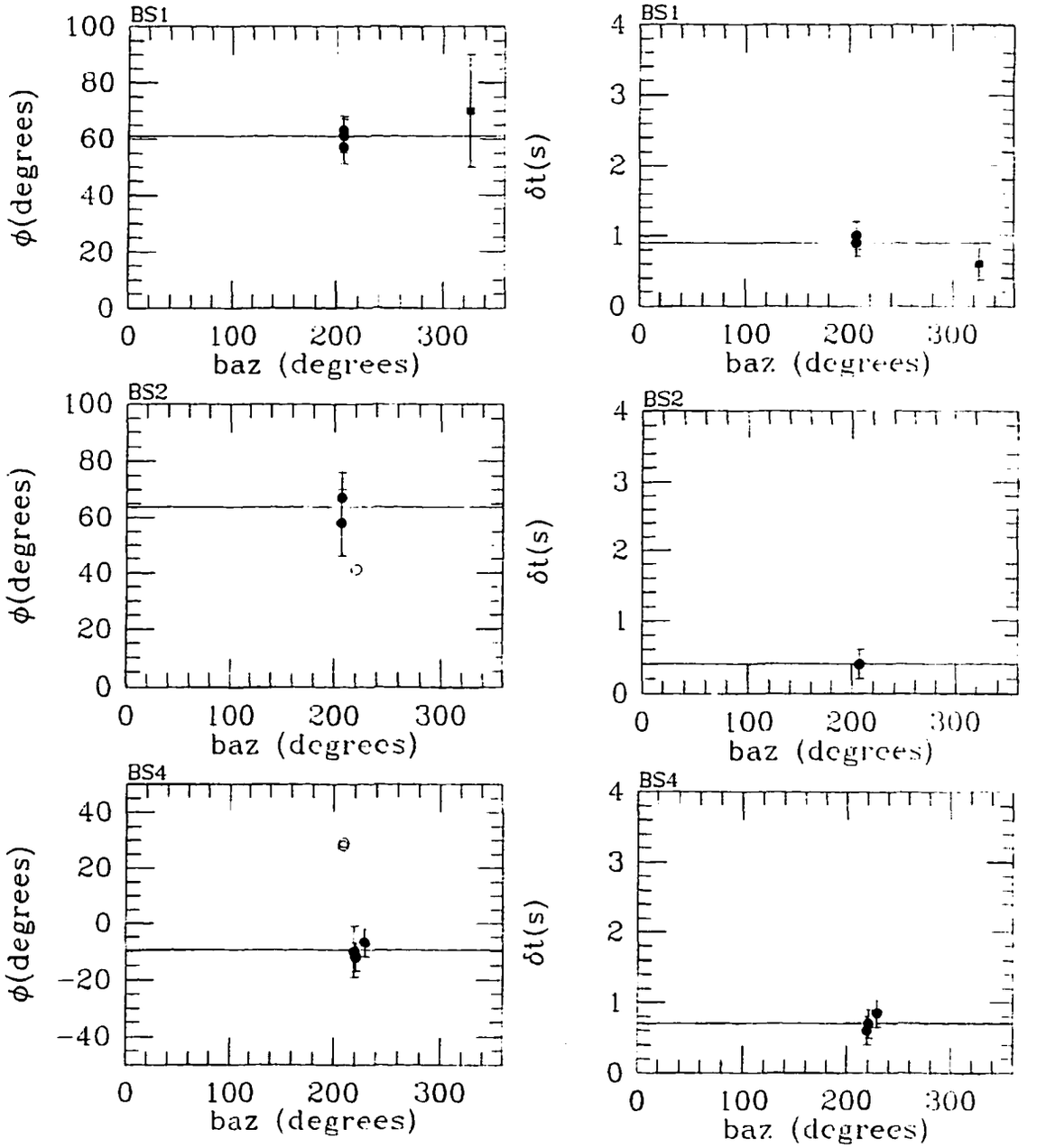

Fig. 4.8: Measurements of the polarization angle (ϕ) and delay time (δt) versus back-azimuth for stations BS1, BS2, and BS4 in the Brooks Range. Measurements of SKS phases are indicated by solid circles, S phases measurements are indicated by a solid square.

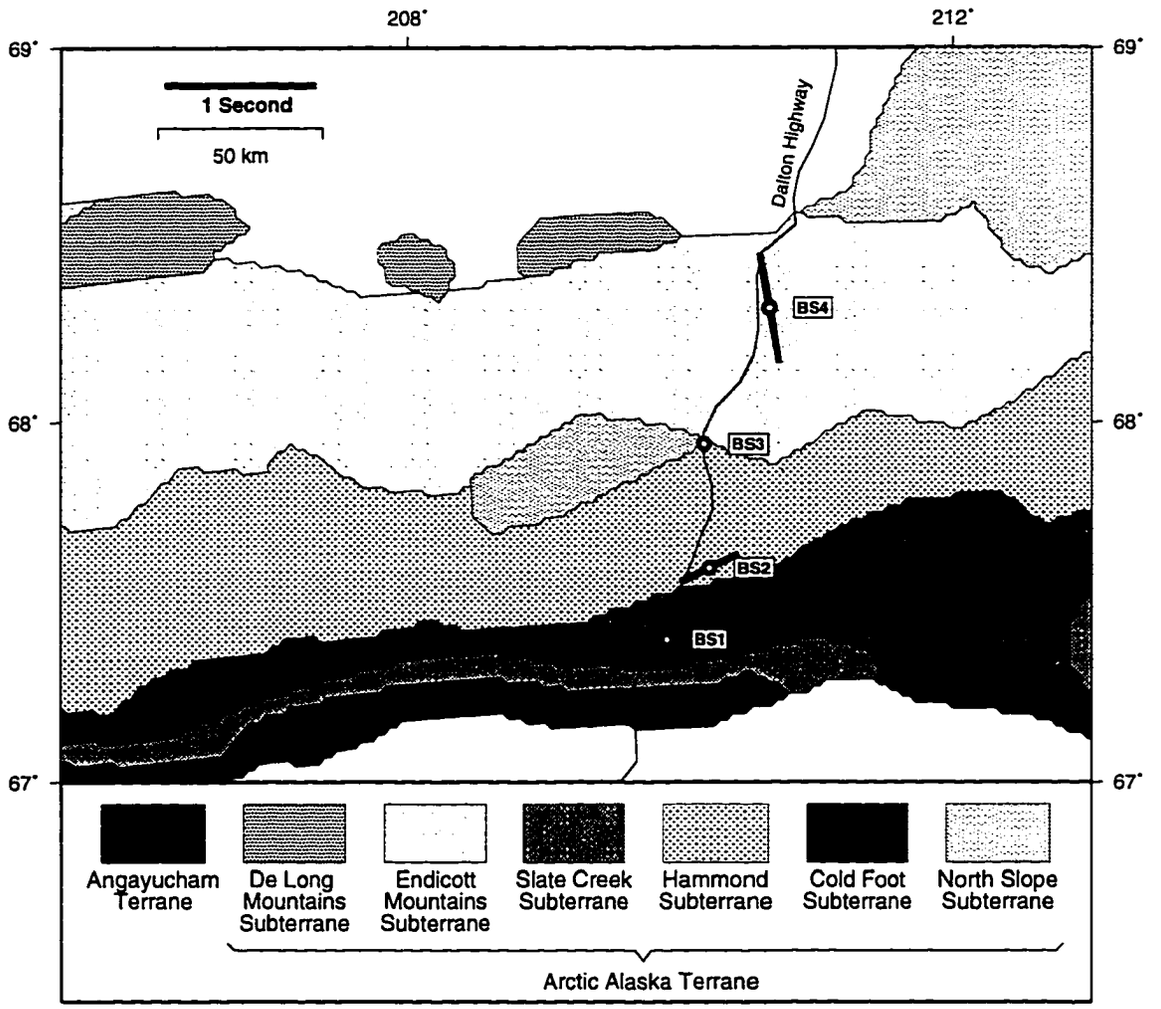

Fig. 4.9: Map showing summary of shear wave splitting results. The fast direction is shown by the orientation of the heavy bar at each site. The magnitude of the delay time is indicated by the length of the bar. No shear wave splitting was found for site BS3.

TABLE 4.1: Summary of Shear Wave Splitting Results

station	lat °N	long°W	ϕ	σ_ϕ	δt	$\sigma_{\delta t}$	nnull	nmeas
BS1	67.40	150.08	60.9	3.2	0.87	0.10	0	4
BS2	67.60	149.77	63.8	7.2	0.40	0.14	1	2
BS3	67.94	149.81	86	13	0.7	0.33	3	1
BS4	68.31	149.35	170.4	3.3	0.72	0.12	2	3

Table 4.1: Average shear-wave splitting measurements of SKS and S measurements at all stations used in this study. Columns are station name, station latitude, station longitude, average ϕ, standard deviation of ϕ, average δt, standard deviation of δt, number of null measurements (i.e., measurements of good signal/noise events that appear to show no anisotropy), and number of measurements used in average.

most station, BS4, had strong splitting (0.72 seconds), but with a fast direction (170.4°), nearly perpendicular to that found at stations BS1 and BS2. A summary of the splitting results is shown in figure 4.8. The polarization information is illustrated in map view in figure 4.9 and listed in table 4.1.

S-wave splitting results determined at the four sites in this study, have proven to be very intriguing, even though more data are needed. The main feature is a nearly 90 degree change in fast direction between the two southern stations and the northernmost station. Station BS3 is located between the southern stations and the northern station and displayed no apparent splitting, based on the small data set that was available. The results from station BS1 are particularly interesting in that the fast direction as observed through S-wave splitting is nearly parallel to a very strong regional foliation of the Coldfoot Schist Belt. This foliation is oriented approximately east-west. A hand-sample taken from the same area as station BS1 in the Coldfoot Subterrane (Coldfoot Schist Belt), showed particularly strong anisotropy (~30%, Nick Christensen, personal communications) with the fast direction parallel to this strong regional foliation (figure 4.10). Thus the fast direction inferred from the hand sample is consistent with the fast direction found from our S-wave splitting study. The orientation of the regional foliation extends laterally over several hundred kilometers. Furthermore, TACT results suggest that the depth of this formation could be as great or greater than 10 km. The correlation of the fast direction determined in our study with the regional foliation direction of the Schist Belt coupled with the depth extent of this body leads us to believe that the teleseismic splitting observed at this site may be related to the crustal fabric. This is an interesting result since crustal anisotropy is

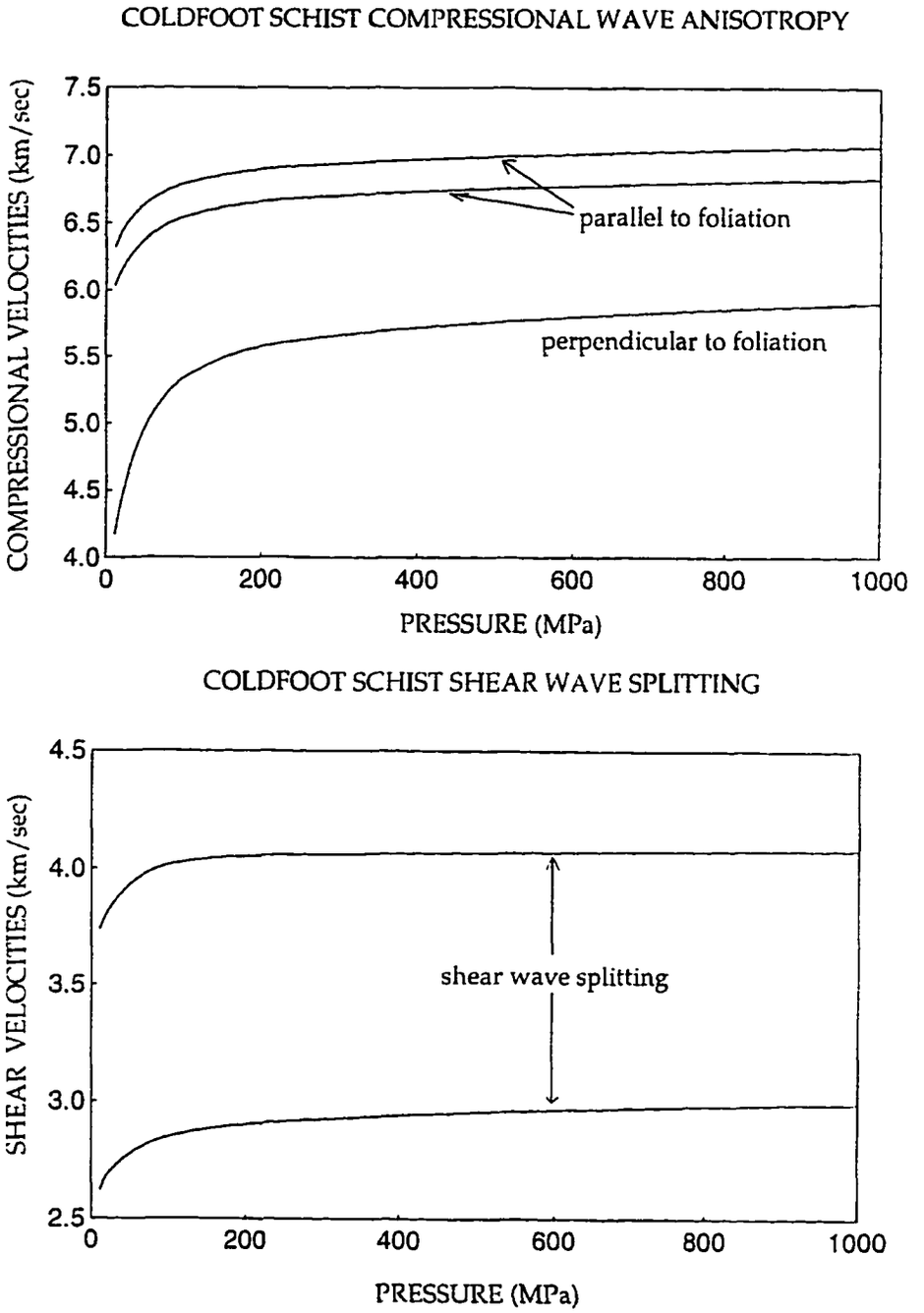

Fig. 4.10: Coldfoot schist compressional wave anisotropy is shown in the top plot. Velocity versus pressure is plotted both parallel to the foliation (fast direction) and perpendicular to the foliation (slow direction). The bottom figure illustrates shear wave splitting for the Coldfoot schist showing the fast and slow directions. (From N. Christensen, personal communication.)

not usually considered to be the source of teleseismic S-wave splitting observations.

Results from many studies clearly indicate that seismic anisotropy is evident in the polarization and splitting of S waves recorded from both local and teleseismic sources. Unfortunately, the cause, and location of the source region of this splitting are not clearly understood. Anisotropy has most commonly been attributed to either stress-induced fracture alignments in the crust (*Crampin, 1985; Crampin and Booth, 1985; Crampin, 1987*), and/or strain-induced lattice preferred orientation of minerals in the mantle (especially for olivine) and in the crust (*Nicolas and Christensen, 1987; Hess, 1964*). The essence of this controversy is elaborated in a paper by *Brocher and Christensen (1990)* with replies and comments by *Crampin (1991)* and *Brocher and Christensen (1991)*, respectively.

Seismic anisotropy determined from teleseismic shear-wave splitting is commonly assumed to represent lattice preferred orientation of minerals in the subcrustal mantle (e.g., *Silver and Chan, 1991*). This assumption is in part based on observations of shear wave splitting that exist for the crust (e.g., *Savage et al.,1989; McNamara and Owens, 1993; Crampin and Booth, 1985; Kaneshima and Ando, 1989; Kaneshima et al., 1988; Barruol and Mainprice, 1993*) which tend to have delay times of about 0.1 to 0.3 seconds; much smaller than typical teleseismic delay times that can approach 2.0 seconds. In addition the crust is commonly viewed as mineralogically complex and heterogeneously deformed which in general forms anisotropic medium. While these assumptions may be true in some or even most cases, they nevertheless need to be thoroughly examined. Strong anisotropy may develop in the crust if a consistent regional fabric is developed (*Barruol and Mainprice, 1993; Kern, 1990; Fountain and Christensen, 1989*). S-wave

splitting studies are now commonly performed whenever three-component data are available. Thus it is becoming more and more important to understand the constraints and limitations of splitting information.

4.5 Conclusions

Depth to Moho was determined from both the inversion and forward modeling of radial receiver functions. Both types of analysis yielded consistent results within the errors of the techniques. The forward modeling procedure took advantage of our knowledge of shallower velocity structure at each site from the TACT results. The depth to these boundaries were allowed to vary to match the data. The TACT results are confirmed by forward analysis since very little variation in the depth to boundaries was required to match arrivals in our data. The receiver functions analysis determined the depth to Moho to be shallowest at 34 km +/- 5 km under station BS1 located north of Coldfoot. The depth to Moho increases to 40 km +/- 5 km at station BS2 located approximately 25 km north of station BS1 along the Dalton Highway. Only forward modeling was used to determine depth to Moho for station BS3 since inversion results did not appear well constrained. At this site Moho appears to be deepest, 54 km +/- 5 km. BS3 is located approximately 60 km north of station BS1. At station BS4, located just north of Atigun Pass, the depth to Moho appears to shoal to a depth of 50 km +/- 5 km. A gravity study conducted by Smith et. al (1987) indicated that the maximum depth to Moho beneath the Brooks Range is 39 km, slightly less than the maximum depth found in our study.

S-wave splitting results through the Brooks Range indicate that polarization angles

and time delays between fast and slow arrivals change over relatively short distances (25-90 km) suggesting a shallow anisotropic source for the splitting. Independently, the seismic anisotropy of oriented rock samples near station BS1, collected by Nick Christensen (personal communications) was found to be particularly large (~30%) with the fast direction parallel to a well-established foliation in this major schist belt and very similar to the observed fast direction from S-wave splitting results at this location. The delay time determined at station BS2, located just 25 km north of station BS1, is half of that found at BS1. The fast direction detected for these two sites is the same. Although station BS2 is located on the Hammond subterrane, TACT results suggest that this region may by underlain by a substantial amount of Coldfoot Schist. These circumstances have led us to speculate that in this case, the teleseismic S-wave splitting results are due primarily to the orientation of minerals in the upper crust. The suggestion that strong foliations in crustal materials can effect S-wave splitting results is not particularly new, although its effect is generally considered to be minor compared to mantle anisotropy. The extremely large amount of anisotropy in these particular rocks, coupled with an observed strong regional foliation and the large size of this unit (thickness ~10 km), suggest that the crustal component of teleseismic S-wave splitting could be much larger than previously expected for certain locations.

Chapter 4 References

Ammon, C. J., G. E. Randall, and G. Zandt, On the non-uniqueness of receiver function inversions, *J. Geophys. Res.* ,*95*, 15,303-15,318, 1990.

Ammon, C. J. , The isolation of receiver effects from teleseismic P waveforms, *Bull. Seismol. Soc. Am.*, *81*, 2504-2510, 1991.

Barruol, G. and D. Mainprice, A quantitative evaluation of the contribution of crustal rocks to the shear wave splitting of teleseismic SKS waves, *Phys. Earth Planet. Inter.*, *78*, 281-300, 1993.

Brocher, T. M. and N. I. Christensen, Seismic anisotropy due to preferred mineral orientation observed in shallow crustal rocks in southern Alaska, *Geology*, *18*, 737-740, 1990.

Brocher, T. M. and N. I. Christensen, Comment and reply on "Seismic anisotropy due to preferred mineral orientation observed in shallow crustal rocks in southern Alaska", *Geology*, *19*, 859-860, 1991.

Crampin, S., Evaluation of anisotropy by shear-wave splitting, *Geophysics*, *50*, 142-152, 1985.

Crampin, S. and D. C. Booth, Shear-wave polarizations near the North Anatolian Fault, II, Interpretation in terms of crack-induced anisotropy, *Geophys. J. R. Astron. Soc.*, *83*, 75-92, 1985.

Crampin, S., Geological and industrial implications of extensive-dilantancy anisotropy, *Nature*, *328*, 491-496, 1987.

Crampin, S., Comment and reply on "Seismic anisotropy due to preferred mineral orientation observed in shallow crustal rocks in southern Alaska", *Geology, 19*, 859-860, 1991.

Fountain, D. M. and N. I. Christensen, Composition of the continental crust and upper mantle; a review, in *Geophysical framework of the United States, vol 172*, edited by L. Pakister and W. Mooney, Geological Society of America, 711-742, 1989.

Fuis, G. S., A. R. Levander, W. J. Lutter, E. S Wissinger, T. E. Moore, and N. I. Christensen, Seismic images of the Brooks Range, Arctic Alaska, reveal crustal-scale duplexing, *Geology, 23*, 65-68, 1995.

Gottschalk, R. R., Structural evolution of the schist belt, south-central Brooks Range fold and thrust belt, Alaska, *J. Struct. Geol., 12*, 453-469, 1990.

Hess, H. H., Seismic anisotropy of the uppermost mantle under oceans, *Nature, 203*, 629-631, 1964.

Kaneshima, S. and M. Ando, An analysis of split shear waves observed above crustal and uppermost mantle earthquakes beneath Shikoku, Japan: Implications in effective depth extent of seismic anisotropy, *J. Geophys. Res., 94*, 14,077-14,092, 1989.

Kaneshima, S., M. Ando, and S. Kimura, Evidence from shear-wave splitting for the restriction of seismic anisotropy to the upper crust, *Nature, 335*, 627-629, 1988.

Kern, H., Laboratory seismic measurements: an aid in the interpretation of seismic field data, *Terra Nova, 2*, 617-628, 1990.

Langston, C. A., The effect of planar dipping structure on source and receiver responses for constant ray parameter, *Bull. Seismol. Soc. Am., 67*, 1029-1050, 1977.

Langston, C. A., Structure under Mount Rainier, Washington, inferred from teleseismic body waves, *J. Geophys. Res.*, *84*, 4749-4762, 1979.

Levander, A., G. S. Fuis, E. S. Wissinger, W. J. Lutter, J. S. Oldow, and T.E. Moore, Seismic images of the Brooks Range fold and thrust belt, Arctic Alaska, from an integrated seismic reflection/refraction experiment, *Tectonophysics*, *232*, 13-30, 1994.

McNamara, D. E. and T. J. Owens, Azimuthal shear wave velocity anisotropy in the Basin and Range province using Moho Ps converted phases, *J. Geophys. Res.*, *98*. 12,003-12,017, 1993.

Moore, T. E. and G. Mull, Geology of the Brooks Range and North Slope, in Alaskan geological and geophysical transect, field trip guide book T104, edited by W. J. Nokleberg and M. A. Fisher, American Geophysical Union, Washington, D. C., 107-130, 1989.

Murphy, J. M., G. S. Fuis, A. R. Levander, W. J. Lutter, E. E. Criley, S. A. Henrys, I. Asudeh, and J. C. Fowler, Data report for the 1990 seismic reflection/refraction experiment in the Brooks Range, Arctic Alaska, *U.S. Geological Survey Open-File Report 93-265*, 128pp, 1993.

Nicolas, A., and N. I. Christensen, Formation of anisotropy in upper mantle peridotites - a review, in *Composition, structure and dynamics of the lithosphere-asthenosphere system vol. 16*, edited by Fuchs, K, and C. Froidevaux, Am. Geophys. Union, Washington, D. C., 111-123, 1987.

Owens, T. J., *Determination of crustal and upper mantle structure from analysis of broadband teleseismic P-waveforms*, Ph. D. dissertation, 146 pp., Univ. of Utah, 1984.

Savage, M. K., X. R. Shih, R. P. Meyer, and R. C. Aster, Shear-wave anisotropy of active tectonic regions via automated S-wave polarization analysis, *Tectonophysics. 165*, 279-292, 1989.

Smith, D.T., D. B. Stone, and J. T. Dillon, Bouguer gravity data and a north south gravity and magnetic profile from the Wiseman area, Brooks Range, Alaska, in *Alaskan North Slope geology*, edited by I. Tailleur, and P. Weimer, Pacific Section, Society of Economic Paleontologists and Mineralogists, Alaska Geological Society, Anchorage, Ak, 725-734, 1987.

Silver, P. G., and W. W. Chan, Shear wave splitting and subcontinental mantle deformation, *J. Geophys. Res., 96*, 16,429-16,454, 1991.

CHAPTER 5

Tomography Methods

5.1 Introduction

As seismic waves propagate through the earth, the physical characteristics of a wave are affected by changes in the material properties of the substance through which they pass. For example, the seismic velocity within the earth directly affects the travel time of a seismic wave. In this way, seismic waves carry with them valuable information about the deep structure of the earth. The methods of tomography can be used to determine these material properties by inverting observed characteristics of the wave forms (i.e. arrival time or amplitude) for specific material properties within the earth such as seismic velocity or attenuation. By definition, tomographic inversions provide solutions for these material properties in three dimensions. The most common type of tomographic problem in current use attempts to determine seismic velocities in a volume from arrival time information. For our studies, P-wave velocities are determined by the inversion of travel-time residuals which are determined from the first P-wave arrival times.

The complete tomographic problem can be divided into two steps, the forward problem and the inversion. In the forward problem, synthetic ray tracing is used through an initial model to compute theoretical travel-times. These theoretical travel-times are subtracted from the observed travel-times to obtain travel-time residuals (also called delay times by some texts). A set of residuals are then inverted in the second step to obtain

velocity corrections to the initial model that will reduce the residuals. It is clear that the tomographic problem is nonlinear in nature since the velocity structure, for which we are attempting to solve, directly affects the geometry of the ray paths along which the travel-times are computed. This nonlinearity requires an iterative approach to the problem. We are also aided by the fact that very accurate models of the earth's spherically symmetric velocity distribution (its strongest variation) exist such as the Jeffries-Bullen model (JB) and the Preliminary Earth Reference Model (PREM), (*Dziewonski and Anderson, 1981*). Thus by using such a spherically symmetric velocity model in the initial ray-tracing we can produce a close starting approximation to the true ray paths. For regions in which complex velocity variations exist, it is important to carry out three-dimensional ray tracing in the forward problem in order to obtain a closer approximation of the true ray paths.

The term tomography was adopted from medical terminology in the 1980's following the adaptation of iterative matrix solvers similar to those used in medical tomography. Prior to this, three-dimensional imaging of material properties in the earth was accomplished using direct methods to invert the derivative matrix *(Aki and Lee, 1976; Aki et al., 1977)*. The introduction of iterative matrix solvers allowed for a large increase in the number of model parameters that could be determined. This occurs because iterative solvers are able to take advantage of the sparseness of the matrix. Such sparseness is inherent in any tomographic technique that is applied to earth structure due to uneven and less than optimal ray-coverage. Iterative matrix solvers do have a disadvantage in that they are unable to solve for the covariance matrix explicitly, as is the case with direct inversion techniques. The covariance matrix provides a direct quantitative estimation of

the solution error. By contrast, iterative solvers typically must rely on the resolution of test models to estimate a qualitative solution error. Recently, methods have been developed to provide quantitative estimates of the model variance for iterative matrix solvers (i.e. jackknifing and bootstrapping, *Efron and Gong, 1983*), but in each case the task becomes computationally expensive for a large number of model parameters. In spite of the drawbacks, the ability of iterative solvers to solve for many model parameters efficiently has rendered it a valuable technique. Without it, global velocity inversions such as those performed by *Dziewonski and Anderson (1984); Tanimoto and Anderson (1984);* and *Woodhouse and Dziewonski (1984)* could not have been accomplished given today's computer systems. In this study we attempt velocity inversions on a regional scale, more explicitly for south central Alaska. The number of model parameters for these model spaces requires the use of an iterative matrix solver.

We have chosen to use the LSQR algorithm (*Paige and Saunders, 1982*). LSQR is a conjugate gradient method that was introduced to seismology by *Nolet (1985)* who showed that it was superior to other iterative matrix solvers such as ART (Algebraic Reconstruction Technique, *Tarantola, 1987)* or SIRT (Simultaneous Iterative Reconstruction Technique, *Humphreys and Clayton, 1988)* because it had a higher rate of convergence and suppressed the propagation of data errors (*Nolet, 1985; Spakman and Nolet, 1988).* More details on the fundamental differences between LSQR, SIRT and ART may be found in *Nolet (1993).* Because of the large amount of data in our studies, a series of inversions on independent subsets of the data are completed and then averaged in a process analogous to a bootstrap procedure, except the data set is not resampled. Each subset

is thus treated as an independent data set. We find that the resolution for our model space is improved by adding this small modification in that random noise in the velocity perturbations is suppressed to some extent by the averaging process.

5.2 Model Parameterization

In a tomographic problem, the model space for which we wish to determine a velocity structure must be made discrete for representation in a computer. The most common type of model space parametrization is one in which the model space is divided into blocks of constant velocity. Model corrections, typically in the form of velocity perturbations from the initial model, are applied to the entire block. In determining the optimal block size, there is a trade-off between resolution and ray coverage. If ray-coverage is not dense enough to accommodate sufficiently small block sizes, then this type of parametrization lacks flexibility in representing non-horizontal velocity boundaries such as a subducting plate. We use a similar but more flexible model parametrization where model velocities are defined at a series of grid points in three-dimensional space. Model corrections are determined for the grid points in the form of velocity perturbations from the initial model velocities. For the purposes of ray tracing, velocities in the space between grid points, $V(x, y, z)$, is determined by three-dimensional interpolation from the surrounding grid points (x_i, y_j, z_k) as given by *Thurber (1983)*:

$$V(x, y, z) = \sum_{i=1}^{2}\sum_{j=1}^{2}\sum_{k=1}^{2} V(x_i, y_j, z_k)\left[1 - \frac{|x - x_i|}{x_2 - x_1}\right]\left[1 - \frac{|y - y_j|}{y_2 - y_1}\right]\left[1 - \frac{|z - z_k|}{z_2 - z_1}\right] \tag{5.1}$$

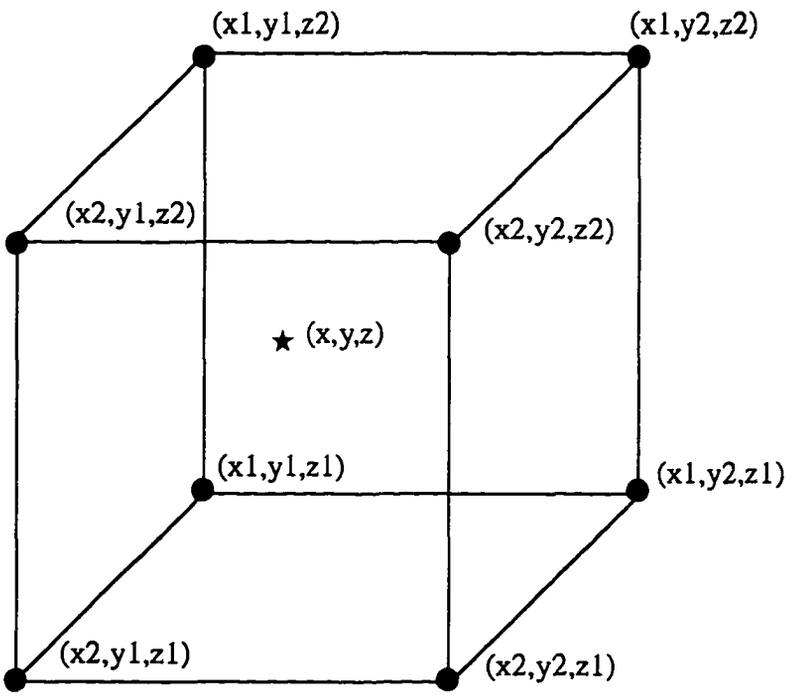

Fig. 5.1: Diagram showing the location and indices of the velocity model grid points (indicated by a "●") used in equations 5.1. The "★" indicates the point at which a velocity is being found by interpolating from the velocity at the surrounding node points.

A diagram of the grid point positions and their corresponding indices appear in figure 5.1. Grid spacing in our models were approximately 25 km in all dimensions and extended to a depth of 500 km. Our initial model was the spherically symmetric Preliminary Reference Earth model (PREM) determined by *Dziewonski and Anderson (1981)*.

5.3 Ray Tracing

The resolution of a tomographic problem is, in part, dependent on the accuracy of ray tracing. For this reason, the ray tracing must be sufficiently accurate for the problem undertaken. This means that for very large scale problems, such as global inversions or inversions for horizontal structure, two-dimensional ray tracing is often adequate. To resolve more complex structures, such as are found in subduction zone environments, three-dimensional ray tracing is required (*Nolet, 1993; Hirahara, 1993*). Unfortunately, three-dimensional ray tracing is also a very computer intensive step in the inversion procedure and one that must be performed repeatedly. Thus for this study, we require an accurate but efficient three-dimensional ray tracing method. We use an algorithm developed by *Zhao (1990)* in which ray tracing is accomplished using a combination of Snell's law and *Um and Thurber's (1987)* pseudo-bending. The idea of combining a bending method with Snell's law at velocity discontinuities was suggested earlier by *Julian and Gubbins (1977)*. A brief explanation of the pseudo-bending technique is given here followed by *Zhao's* adaptation.

Pseudo-bending differs from other bending techniques in that it does not directly solve the ray equations. This algorithm uses a geometric approach to minimize the travel

time along ray path segments. The true ray path being defined by Fermat's principle as the path of stationary time. Defining the vector end points along ray path segments as $\vec{X}_{k-1}$, $\vec{X}_k$, and $\vec{X}_{k+1}$ as shown in figure 5.2, a new position for the midpoint vector, $\vec{X}_k'$, is sought that reduces the travel time. To define this new position, a direction ($\hat{n}$) and a magnitude of offset (R) is determined with respect to a point midway between the ray path end points, $\vec{X}_{mid}$. The ray equation derived from Fermat's principle (*Pereyra et al., 1980*) is given by:

$$-\left(\frac{d^2\vec{r}}{ds^2}\right) = \frac{1}{V}\left(\nabla V - \frac{dV}{ds}\frac{d\vec{r}}{ds}\right) \tag{5.2}$$

where $\vec{r}$ is the position vector along the ray path, V is the velocity and s is a segment of the path length. The second term on the right hand side of equation 5.2 is the component of ∇V that is parallel to the ray path. (to see this it is helpful to recognize that $\frac{dV}{ds}$ may be expanded to $\nabla V \bullet \frac{d\vec{r}}{ds}$.) Therefore, the left hand side of equation 5.2 represents the component of ∇V that is perpendicular to the ray path. $\frac{d^2\vec{r}}{ds^2}$ is the equation for the ray path curvature, hence the component of ∇V perpendicular to the ray path is always antiparallel to the ray path curvature. This yields the proper direction $\hat{n}$. Referring to figure 5.2 we have:

$$\hat{n} = \nabla V - [(\nabla V)\cdot(\vec{X}_{k+1} - \vec{X}_{k-1})]\frac{\vec{X}_{k+1} - \vec{X}_{k-1}}{\left|\vec{X}_{k+1} - \vec{X}_{k-1}\right|^2} \tag{5.3}$$

The unit vector $\hat{n}$ is then normalized. The magnitude of the offset (R) is found by

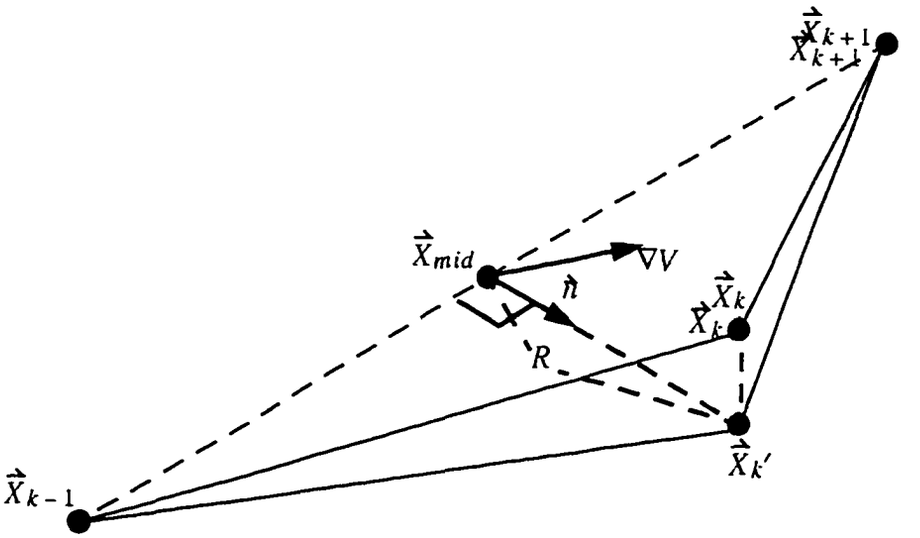

Fig. 5.2: *Um and Thurber's* three point perturbation technique. The initial ray path is represented by the end points of the vectors: $\vec{X}_{k-1}, \vec{X}_k, \vec{X}_{k+1}$. A new point $\vec{X}_{k'}$ is sought that minimizes the travel time as explained in the text. Redrawn from *Um and Thurber (1987).*

minimizing the travel time along the segments defined by $\vec{X}_{k-1}$, $\vec{X}_{k'}$, and $\vec{X}_{k+1}$ The travel time, T is given by:

$$T = \frac{1}{2}\left\{\left|\vec{X}_{k'} - \vec{X}_{k-1}\right|\left(\frac{1}{V_{k'}} + \frac{1}{V_{k-1}}\right) + \left|\vec{X}_{k+1} - \vec{X}_{k'}\right|\left(\frac{1}{V_{k+1}} + \frac{1}{V_{k'}}\right)\right\} \quad (5.4)$$

The velocity at $\vec{X}_{k'}$ is estimated by a Taylor's series expansion about the velocity at the mid point, $\vec{X}_{mid}$. R is given by:

$$R = -\frac{cV_{mid} + 1}{4c\hat{n} \cdot (\nabla V)_{mid}} + \left[\left(\frac{cV_{mid} + 1}{4c\hat{n} \cdot (\nabla V)_{mid}}\right)^2 + \frac{L^2}{2cV_{mid}}\right]^{1/2} \quad (5.5)$$

where $c = \frac{1}{2}\left(\frac{1}{V_{k+1}} + \frac{1}{V_{k-1}}\right)$ and $L = \left|\vec{X}_{k+1} - \vec{X}_{mid}\right|$. For details on the derivation of R the reader is referred to *Um and Thurber (1987).*

The pseudo-bending algorithm requires a smooth velocity gradient throughout the model space. *Zhao (1990)* modified the pseudo bending technique by alternately solving for ray path points at velocity discontinuities using Snell's law and then solving for ray path points between the velocity discontinuities using the pseudo-bending method described above. This procedure is iteratively carried out until a set convergence criteria has been reached in minimizing the travel time.

An attempt to ray trace through our model space using pseudo bending alone failed due to the large scale of our model space. By applying Snell's law at PREM boundaries for our model space, it was found that ray paths converged satisfactorily. *Zhao's* ray tracing method used in this manner is similar to the approach taken by *Thurber and Ellsworth*

(1980) where a ray path estimate is first found using a two-dimensional ray tracing technique and then the pseudo bending algorithm is applied to perturb the ray estimate in three-dimensions. For our studies, the conclusion as to whether a ray path converged satisfactorily was based on comparisons of the ray paths with those traced using a scheme that directly solved the ray equations. The most accurate method for ray tracing is to solve the first order differential equations derived from the eikonal equations along the ray path using, for example, a Runge-Kutta type integration (*Aki and Richards, 1980)*. While such an integration method is too computer intensive to use in our tomographic inversion, it is a very useful method for testing the pseudo bending and combined pseudo bending and Snell's law methods for our model space.

5.4 Velocity Inversion

The goal of the velocity inversion is to estimate velocity corrections to our initial model from the observed travel times of the ray paths. Expressing the observed travel time for a given ray path in a Taylor's series expansion yields:

$$T = T_0 + \sum_{n=1}^{N} \frac{\partial T}{\partial V_n} \Delta V_n + e \qquad (5.6)$$

Where T_0 is the theoretical travel time of the ray path computed from the initial velocity model. $\frac{\partial T}{\partial V_n}$ is the partial derivative of the travel time with respect to the n^{th} model parameter, and e represents the higher order terms in the expansion and data errors. In

theory, the partial derivatives arise from integrating along the ray path:

$$\frac{\partial T}{\partial V_n} = \int \left[\frac{1}{V(s)}\right]^2 \frac{\partial}{\partial V_n} V(s) ds \tag{5.7}$$

To simplify computations, partial derivatives with respect to slowness $U_n = \frac{1}{V_n}$ are computed. Taking the integral of discrete parts by dividing the ray path into M segments we have.

$$\frac{\partial T}{\partial U_n} = \sum_{i=1}^{M} \frac{\partial}{\partial U_n} U_i(s) \Delta S_i \tag{5.8}$$

Here $U_i(s)$ is the slowness at the midpoint of segment i and ΔS_i is the step length of that ray path segment. $\frac{\partial}{\partial U_n} U_i(s)$ is calculated by using the interpolation function defined in equation 5.1. Subtracting T_0 from both sides of equation 5.6, the left hand side of the equation becomes the travel time residual. In the case of teleseismic ray paths, the relative travel time residual is substituted for $T - T_0$ as discussed in section 5.7. We may now write equation 5.6 for the entire data set of ray paths as:

$$A\vec{x} = \vec{d} \tag{5.9}$$

Where $\vec{d}$ is a column vector containing the entire set of N travel time residuals, $\vec{x}$ contains the M model correction parameters we wish to solve for, and A is an N X M matrix containing the partial derivatives shown in equation 5.8. To solve equation 5.9 we have

chosen the conjugate gradient algorithm LSQR developed by *Paige and Saunders (1982)*. The basic idea of LSQR is to use a Lanczos type iteration to build an orthonormal basis in the model space ($\vec{\mu}_k$) while simultaneously constructing an orthonormal basis in the data space ($\vec{\rho}_k$). $\vec{\rho}_1$ is found by simply normalizing $\vec{d}$, $\alpha_1\vec{\rho}_1 = \vec{d}$. $\vec{\mu}_1$ may then be found by a simple back projection of $\vec{\rho}_1$:

$$\beta_1\vec{\mu}_1 = \boldsymbol{A}^T\vec{\rho}_1 \tag{5.10}$$

The next basis vector in the data space is then found by a forward projection of $\vec{\mu}_1$ which is made orthogonal to $\vec{\rho}_1$ and normalized to yield:

$$\alpha_2\vec{\rho}_2 = \boldsymbol{A}\vec{\mu}_1 - \alpha_1\vec{\rho}_1 \tag{5.11}$$

Continuing on in a series of projections and back projections the entire sets of basis vectors are constructed. In general these equations take the form:

$$\begin{aligned} \alpha_{k+1}\vec{\rho}_{k+1} &= \boldsymbol{A}\vec{\mu}_k - \beta_k\vec{\rho}_k \\ \beta_{k+1}\vec{\mu}_{k+1} &= \boldsymbol{A}^T\vec{\rho}_{k+1} - \alpha_{k+1}\vec{\mu}_k \end{aligned} \tag{5.12}$$

Where α_k and β_k represent normalization constants. With this construction of the basis vectors in mind, the next step, is to expand the model correction vector in terms of its

basis:

$$\vec{x} = \sum_{j=1}^{k} m_j \vec{\mu}_j \tag{5.13}$$

Substituting this into the original equation 5.9, we have:

$$\sum_{j=1}^{k} m_j A\vec{\mu}_j = \alpha_1 \vec{\rho}_1 \tag{5.14}$$

Rearranging equation 5.11 and substituting it into 5.14:

$$\sum_{j=1}^{k} m_j(\alpha_{j+1}\vec{\rho}_{j+1} + \beta_j \vec{\rho}_j) = \alpha_1 \vec{\rho}_1 \tag{5.15}$$

We may now make use of the orthogonality of the basis vectors and take the inner product of $\vec{\rho}_l$ with both sides of this equation to obtain the model correction value:

$$m_1 = \frac{\alpha_1}{\beta_1} \qquad \text{for } l = 1$$

$$m_l = -\frac{m_{l-1}\alpha_l}{\beta_l} \qquad \text{otherwise} \tag{5.16}$$

Thus we are able to compute the model corrections without having to actually invert A. The LSQR algorithm reduces the matrix A to a lower bidiagonal form in order to take advantage of its sparseness and reduce computations for the multiplications by A and A^T. For a more detailed explanation of LSQR, the reader is referred to *Paige and Saunders*

(*1982*), *van der Sluis and van der Vorst* (*1987*), and *Nolet* (*1993*).

Typically model basis vectors and their corrections are computed for the entire data set and the model corrections are then applied to the initial model for the final solution. A small modification was made to this procedure by dividing the ray paths up into seven subsets based on the outcome of a random number generator. The subsets were created after the forward problem on the entire data set had been completed, thus all the derivatives for matrix $\boldsymbol{A}$ were computed for the entire data set with respect to a common initial model. Model basis vectors and model corrections for each subset were then individually computed. The model corrections from the inversion of each subset were then averaged to obtain the final composite solution.

5.5 Resolution Determination

Errors in tomographic solutions arise from two sources. First, there are data errors and second there are inversion errors. The data vector ($\vec{d}$) in equation 5.9 can be expanded to include data errors ($\vec{e}$): $\vec{d} = \vec{d}' + \vec{e}$. The errors in the tomographic solution can then be represented as (*Nolet, 1987*):

$$\vec{x} - \vec{x}_{true} = (\boldsymbol{A}^{-1}\boldsymbol{A} - \boldsymbol{I})\vec{x}_{true} + \boldsymbol{A}^{-1}\vec{e} \qquad (5.17)$$

Here, $\boldsymbol{I}$ is the identity matrix. $\boldsymbol{A}^{-1}\vec{e}$ represents the data errors from, for example, mislocated earthquakes. $(\boldsymbol{A}^{-1}\boldsymbol{A} - \boldsymbol{I})\vec{x}_{true}$ represents inversion errors that arise in the tomographic solution due to uneven ray path coverage, model parametrization effects and

algorithm performance (*Spakman and Nolet, 1988*). Separating the effects of the different type of errors on the tomographic solution is often difficult. If no large systematic errors exist in the data set then one can reduce the data errors by having a large and redundant data set. Unfortunately, this is not always the case. For example, sometimes there are systematic mislocations of earthquakes that may not be averaged out. This can be a particular problem in subduction zone environments since often the models used to locate the events do not include effects of the slab. A more detailed discussion of the estimation of data errors for ray paths used in our tomographic inversions can be found in the following section on data.

Since iterative matrix solvers such as LSQR do not directly solve for $\boldsymbol{A}^{-1}$ it is not possible to exactly solve for $\boldsymbol{A}^{-1}\boldsymbol{A}$ and thus a rigorous quantitative estimation of model errors is not possible. *Nakanishi and Suetsugo (1986)* proposed to construct $\boldsymbol{G} = (\hat{\boldsymbol{a}}_1, \hat{\boldsymbol{a}}_2, \ldots, \hat{\boldsymbol{a}}_n)$, a generalized inverse of $\boldsymbol{A}$ by solving $\boldsymbol{A}\hat{\boldsymbol{a}}_i = \hat{\boldsymbol{n}}_i$ where $\hat{\boldsymbol{n}}_i$ are unit vectors. This technique requires the same number of inversions as there are data and thus becomes prohibitively computer intensive for a large data set (*Nolet, 1987*). Another approach to determining model resolution is to employ a resampling technique. Resampling techniques are statistical methods for evaluating model variance that are insensitive to the data variance *(Tichelaar and Ruff, 1989)*. In such a method, multiple data sets are constructed from one measured data set. Model estimates derived from the individual resampled data sets are then combined for a "best model" and standard error. The two main techniques are jackknifing and bootstrapping. In a jackknife method multiple resampled data sets have a fewer data as compared to the whole data set and a datum does not appear

twice within the same resampled data set, although it will often appear in the other resampled data sets. In other words, the data set is divided into k subsets each of which have $\frac{1}{k}$ of the data randomly removed. Information about the model that derives from missing data in the *jth* subset may be expressed in terms of the results of an inversion on that subset ($\tilde{\vec{x}}_j$) as:.

$$\tilde{x}_j = k\tilde{\vec{x}}_{full} - (k-1)\tilde{\vec{x}}_j \tag{5.18}$$

where $\tilde{\vec{x}}_{full}$ represents model corrections due to an inversion of the full data set and n is the total number of data. $\tilde{x}_j$ has been called a pseudo-inversion by *Lees and Crosson (1989)*. The jackknife estimate of the "best model" is the average of the pseudo-inversions and the model variance is given by:

$$\upsilon = \frac{1}{k-1}\sum_{j=1}^{k}\left(\tilde{x}_j - \frac{1}{k}\sum_{m=1}^{k}\tilde{x}_m\right)^2 \tag{5.19}$$

The bootstrap method is very similar to the jackknife method except that resampled data sets in a bootstrap method have the same number of data as the original data set and a datum will often appear more than once in the same resampled data set. The model variance in a bootstrap technique is simply given by:

$$\nu = \frac{1}{N-1}\sum_{j=1}^{N}\left(\tilde{\vec{x}}_j - \sum_{m=1}^{N}\tilde{\vec{x}}_m\right)^2 \tag{5.20}$$

For more details on jackknife and bootstrap methods the reader is referred to *Efron (1981)*, *Efron and Gong (1983)*, and *Cressie (1993)*. The difficulty with resampling methods is that they require a large number of data sets to be inverted in order to obtain a statistically significant error analysis and again the problem becomes computer intensive. We employed a bootstrap type approach to attempt to understand the model variability in our inversions. Since we were unable to complete an inversion on our entire data set in one step, the bootstrap procedure was applied to subsets of the data in the following manner. The data were divided into seven subsets by the outcome of a random number generator as described previously and inversions carried out for those subsets. After saving the results, the original data set was once again divided into seven new subsets for which inversions were completed. This procedure was repeated seven times resulting in 49 total inversions for the model space. The standard error was then computed from the model variance given by equation 5.20. In figure 5.3 we show a histogram of the estimated average model standard error for each depth in the model space. The estimated average errors for all layers is less than 0.25%. The highest average errors exist for the two boundary layers of the model space (0-25 km and 475-500 km). Overall these errors indicate that our approach of dividing the data up into seven subsets is a valid one for the given model space and ray path coverage since the variability of the model correction parameters vary on average less than 0.25% from one inversion to the next.

In order to test the resolution of our tomographic inversions, we employed an image reconstruction technique in which the travel times from ray paths traced through a synthetic velocity structure are considered as data and inverted. The resultant images are

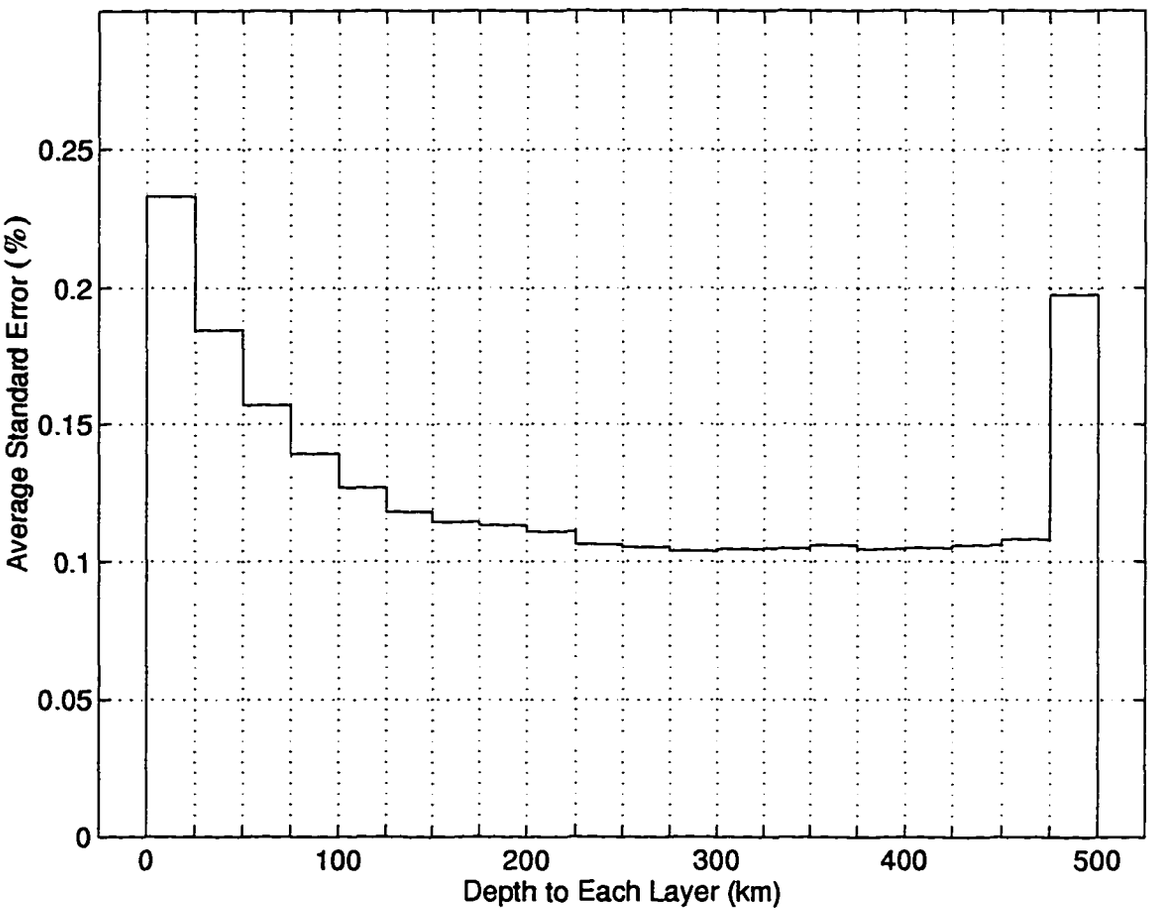

Fig. 5.3: Histogram of the average standard error in percenti for each model space layer n depth. Standard errors were computed over 49 total velocity inversions for the model space. Each datum was used seven times as described in the text. The low variability of the model correction values between inversions indicates that the practice of dividing the data set into seven subsets for inversions is a valid one for this particular ray path coverage in the model space.

then compared to the original synthetic structure. The purpose of these tests is to determine the ability of the given ray paths to resolve structure in the model space. Since uneven ray path coverage is a common problem in most tomographic studies of the earth, resolution is not expected to be even throughout the model. An image reconstruction test can point out areas in the model space where resolution is poor or conversely very good, and thus the actual inversion results can be interpreted accordingly. In our studies, resolution test inversions were carried out on an initial model containing a slab-like structure of +6% velocity perturbation in the approximate location where the subducting Pacific plate is believed to exist based on hypocenter locations. The slab-like structure is extended to the bottom of the model space (500 km) with the same dip as the lower portion of the plate inferred from earthquake locations. Resolution tests were also carried out on this same slab structure that terminated abruptly at a depth of 200 km. The subducting Pacific plate is the strongest velocity anomaly in our model space and the feature we are most interested in resolving. Therefore these initial models were chosen to determine the ability and depth to which the ray paths in our data sets are able to resolve just such structures. Results of the resolution tests are presented in chapter 6.

5.6 Local data

In our velocity inversions three types of data sets were used: arrival times from local ray paths from (*Zhao et al., 1995*); arrival times from teleseismic ($30° \leq \Delta \leq 90°$) ray paths of earthquakes that occurred in Alaska and were recorded on the global network (outgoing data set); and arrival times from teleseismic ray paths of earthquakes that

occurred world wide and were recorded by the Alaska Seismic Network (incoming data set). The teleseismic data is described in section 5.7.

Local data consisted of travel time residuals derived from 12,237 relocated hypocenters taken from *Zhao et al. (1995)*. In *Zhao's* study the relocations were carried out jointly with a velocity inversion which assumed the presence of a high velocity subducting slab in the initial model. The importance of including slab features when locating earthquakes in a subduction zone environment has been stressed by *Hauksson (1985)*, who reported mislocations of up to 40 km for deep events determined by a local seismic array in the Shumagin Islands. In *Zhao's (1995)* study most of the hypocenters relocate a few kilometers shallower. In addition the Wadati-Benioff zone becomes thinner after relocation. Given this refined data set we opted not to relocate local events in the velocity inversion.

5.7 Teleseismic Data

The outgoing teleseismic data set consisted of 335 earthquakes that occurred within the model space (between 55° to 67° north latitude and 140° to 167° west longitude). These events were relocated with respect to PREM using a two-dimensional ray tracing scheme in order to be consistent with the velocity inversion, which uses PREM as the reference model. Slab effects were not taken into account in this relocation procedure. *Engdahl et al. (1977)* located hypocenters with a subducting slab model in the Kuril region and compared the locations to those obtained using a spherically symmetric earth velocity model. They found that as a result of the relocations only small changes in the

azimuth of teleseismic ray paths were predicted. Nevertheless, for the outgoing teleseismic data set, it would have been better to use hypocenter locations based on the local Alaska Seismic Network. Unfortunately, these events occurred between January 1964 and August 1987 for which reliable, high quality locations were not uniformly available from this network.

The incoming teleseismic data set consisted of ray paths from 359 earthquakes that occurred world-wide. These events were recorded by the Alaska Seismic Network and hand picked using the program XPICK *(Robinson, 1991)*.

Teleseismic ray paths have an advantage over local ray paths in that they sample greater depths within the earth. By contrast, local ray paths penetrate to maximum depths of ~200 km. In our studies, we were interested in obtaining velocity perturbation information about the subducting slab at depths greater than the known seismicity which is also about 200 km.

In a teleseismic tomographic problem in which we wish to solve for velocity perturbations on a regional scale, the goal is to solve for the velocity structure of a region for which only part of the teleseismic ray paths traverse. It is therefore necessary to remove path effects due to structure outside of the model space prior to the velocity inversion. *Aki et al. (1977)* proposed the use of relative residuals to remove these effects as well as errors due to hypocenter mislocations and station corrections. The relative residual for the *ith*

ray path is given by

$$R_i = (T_{obs} - T_{th})_i - \frac{1}{n}\sum_{j=1}^{n}(T_{obs} - T_{th})_j \qquad (5.21)$$

Where T_{obs} is the observed travel time and T_{th} is the theoretical travel time. For the incoming data set, j is summed over all the ray paths from one earthquake; for the outgoing data set, j is summed over all the ray paths recorded at one station. Mislocations of the hypocenters for the incoming data set is therefore less important than mislocations of hypocenters in the outgoing data set or the local data set, since these errors will be removed in the relative residual computations *(Hirahara, 1993)*. Unwanted systematic effects due to anomalous structure outside of the model space are removed because ray paths associated with a common receiver in the outgoing data set or a common earthquake in the incoming data set, traverse nearly the same path in the lower mantle. When the ray paths enter the upper mantle, they begin to diverge such that individual ray paths sample different velocity structures within the model space *(Dueker et al., 1993)*. As a result of using relative residuals, only relative velocity perturbations within the model space can be determined in the velocity inversion instead of absolute velocity values *(Thurber and Aki, 1987)*. A schematic diagram of these ray paths is presented in figure 5.4.

Because the three-dimensional ray-tracing algorithm of *Um and Thurber (1987)* is a two point bending scheme, it is necessary to compute the exit points of the teleseismic ray paths from the model space. Once the exit point is found, it is possible to carry out the three-dimensional ray tracing for only that portion of the teleseismic ray path that

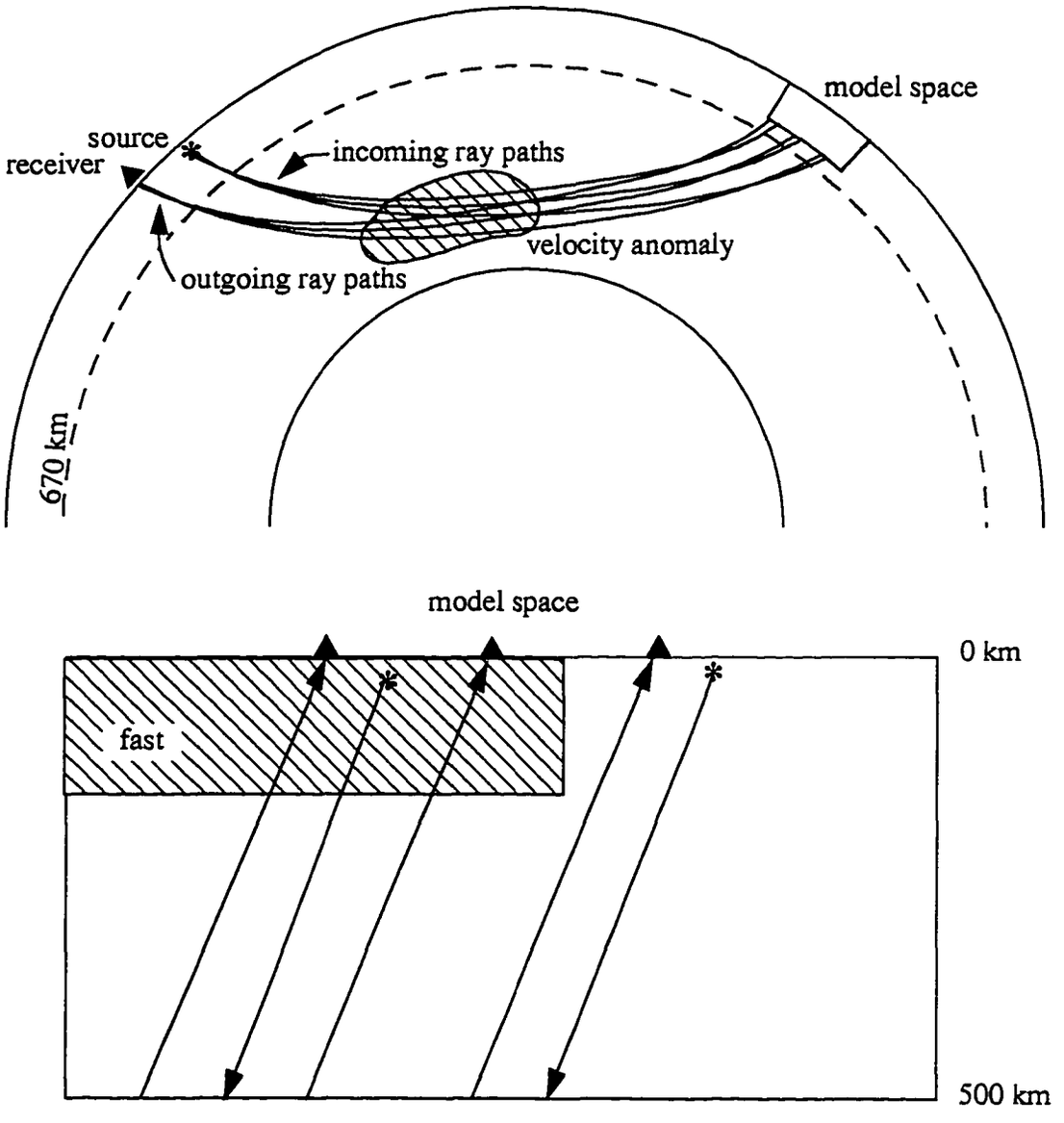

Fig. 5.4: A schematic of teleseismic ray paths. Ray paths from a common source in the incoming data set and a common receiver in the outgoing data set traverse nearly the same path in the lower mantle and thus effects due to low frequency velocity heterogeneities in the lower mantle are removed by subtracting out the average travel time residual for a source (incoming data) or a receiver (outgoing data). Velocity information is preserved for the upper mantle since ray paths begin to diverge at this point due to higher frequency velocity variations. Redrawn from *Dueker et al. (1993)*.

traverses the model space. A two-dimensional exact ray-tracing technique through PREM was used in which the eikonal equation is integrated along the ray path until the outer boundary of the model space is reached. Exit points were found for a depth of 700 km. This is deeper than the model space for which the velocity inversion was carried out (500 km) to avoid having a fixed point at the base of the model space. Thus the point of the ray path at a depth of 500 km is allowed to move as the velocity inversion required.

Teleseismic ray paths have near vertical trajectories within the model space. This lack of horizontally crossing ray paths causes a smearing of the velocity anomalies in the direction of the ray paths. In figure 5.5-a we show the results of a velocity inversion along a cross section through Kodiak Island, Alaska. A contoured plot of the hit counts is shown in figure 5.5-b. A hit count is the number of ray paths that pass in the vicinity of a given model node point and is a direct measure of the ray path coverage. Hit counts within the dashed rectangular area derive from a set of teleseismic ray paths that originate just off Kodiak Island and exit the model space at a steep angle to the northeast. These particular ray paths are not crossed by any other ray paths below a depth of ~150 km. The corresponding rectangular area in the velocity perturbation model (figure 5.5-a) shows a high velocity anomaly elongated in the direction of these ray paths. This anomaly is caused by the teleseismic ray paths smearing high velocities associated with the Pacific slab at the surface along their trajectories. This velocity anomaly is entirely an artifact of the ray path coverage and is an example of an artificial velocity anomaly showing up in the inversion results. A very similar artifact appeared in the resolution test inversions.

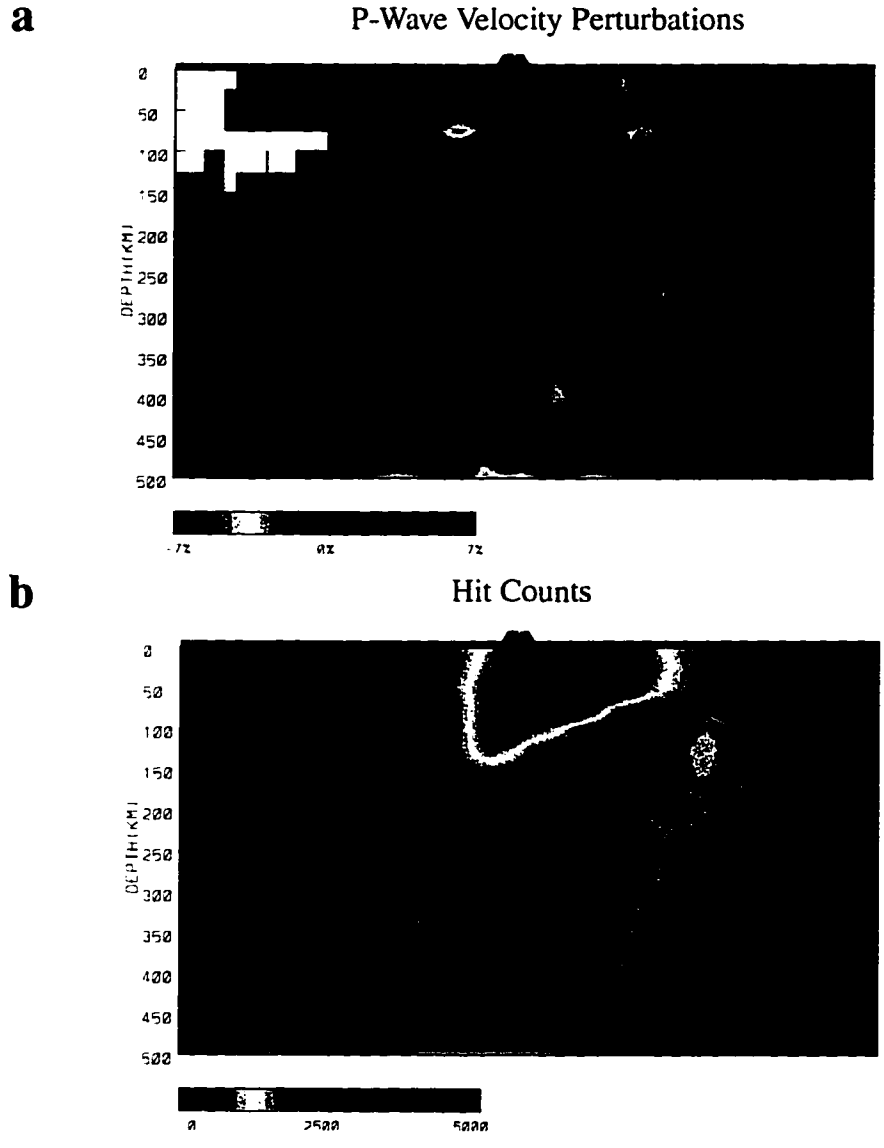

Fig. 5.5: Example of teleseismic smearing. Image (a) is the velocity perturbations in percent from PREM for a cross section through Kodiak Island. The rectangular box encloses a high velocity anomaly. Image (b) is the contoured hit counts for the same cross section as in (a). The rectangular box is in the same location as in (a) and shows a region of high hit counts for this part of the mantle. These hit counts derive from a set of teleseismic ray paths that occur just south of Kodiak Island and exit the model space at a steep angle to the northeast. The high-velocity anomaly in (a) is interpreted as an artifact due to the teleseismic ray paths smearing high velocities associated with the Pacific Plate at the surface along their trajectories.

5.8 Joint Inversions of Local and Teleseismic Data

The velocity perturbation images presented in chapter 6 are the result of a joint local and teleseismic velocity inversion. In the joint inversions, relative residuals are used for the teleseismic data and raw (not relative) residuals are used for the local data. This approach is justified since presumably the relative residuals of the teleseismic data represent only velocity variations within the model space (*Hirahara, 1993*).

The use of teleseismic ray paths is very important to the investigation of deeper velocity structure in subduction zones (*Hirahara, 1993*). It is hoped that the local ray paths are able to provide strong constraints on the upper 200 km of the model space so that the teleseismic data can provide a better estimate of the deeper structure than would be possible without the use of local data. Furthermore, resolution tests indicate that the combination of local and teleseismic ray paths provide a better resolution of the upper 200 km in the model space than inversions using the local data alone. This is most likely simply due to having a larger data set in the joint inversion as compared to the local inversion.

In our velocity inversions, the data were divided into seven roughly equally sized data sets and each set was inverted separately. Model corrections for each individual inversion were then averaged for the final solution. Each ray path was assigned to a given data set (1-7) based on the outcome of a random number generator. Therefore, for a given inversion, local and teleseismic ray paths were combined.

5.9 Summary

A subduction zone is a favorable candidate for a tomographic velocity inversion. There exists strong velocity variations and often a high rate of seismicity. Furthermore the location of the Wadati-Benioff zone can often provide some control on the resolution of the inversions since it is believed to occur in the relatively cold, brittle regions of the slab. In our studies, we use the algorithm LSQR (*Paige and Saunders, 1982*) to accomplish a P-wave velocity inversion for central Alaska. LSQR is a computationally efficient iterative type matrix solver that allows for the solution of a large number of velocity perturbations for a given model space. The primary disadvantage of an iterative matrix solver is that the covariance matrix can not be directly constructed. Thus in many instances, error analysis is restricted to qualitative image reconstruction techniques.

It is important to use a three-dimensional ray tracing scheme when conducting a velocity inversion in any region in which a large amount of lateral velocity variation is believed to exist. A subduction zone is just such an environment, with the primary velocity anomaly being high velocities associated with the subducting slab. Since ray paths must be computed repeatedly in a tomographic velocity inversion, another requirement of the ray tracing method is that it be computationally efficient. The ray tracing technique of *Zhao (1990)* which combines pseudo-bending (*Um and Thurber, 1987*) with Snell's law satisfies all the above criteria. This method has the added benefit of being very flexible with regards to model parametrization since both velocity gradients and velocity boundaries may be used. Furthermore, we have found that for large regions, pseudo-bending used alone failed to converge. With the added constraint of Snell's law placed at selected

boundaries with depth, *Zhao's* method converges satisfactory. For our studies, Snell's law was used at the boundaries defined by the global velocity reference model PREM (*Dziewonski and Anderson, 1981*) which was also used as the initial model for the velocity inversions.

Data for the velocity inversion of central Alaska consisted of both local and teleseismic P-wave arrival times. Two types of data made up the teleseismic set, those from incoming ray paths and those from outgoing ray paths. For all teleseismic data, relative residuals are computed and used in the velocity inversion. The outgoing data set suffers from the disadvantage that hypocenters cannot be relocated during the inversion process and thus location errors exist in that data. This is not a problem for the incoming data set since the hypocenters occur outside of the model space. In this case, location errors are removed in the computation of the relative residuals. All teleseismic ray paths traverse very nearly vertical paths within the model space. For this reason, velocity anomalies in regions covered only by teleseismic ray paths tend to be smeared in the vertical direction. The primary advantage of teleseismic ray paths is that they sample all depths of the model space and are therefore the only data containing information on velocity structure beneath the bottoming-out depths of the local ray paths. Local ray paths tend to have more crossing rays and are therefore better at determining lateral velocity variations. Local hypocenters may also be relocated during the velocity inversion. In our case, arrival times of relocated hypocenters from *Zhao et al. (1995)* were used for the local data. By combining local and teleseismic data in a joint velocity inversion, we are able to take advantage of the strengths of both data types.

Potential exists for improved tomographic velocity studies of the central Alaska region in the future. First, resolution tests using synthetic data suggests that the resolution of the subducting slab could be improved with more data. In particular, more teleseismic data would be helpful. It would be a benefit to add more recent data to the outgoing data set, for which hypocenter locations are available from the Alaska Seismic Network. The incoming data set is considered to be of exceptionally high quality since events were hand-picked. Second, inclusion of S-wave arrival times would add more data and also more information on the velocity structure. Finally the incorporation into the inversion of later phases, particularly P reflections off of the subducting slab, would provide strong constraints on the location the subducting slab.

Chapter 5 References

Aki, K., and W. H. K. Lee, Determination of three-dimensional velocity anomalies under a seismic array using first P arrival times from local earthquakes, Part 1. A homogeneous initial model, *J. Geophys. Res.*, *81*, 4381-4399, 1976.

Aki, K., A. Christofferson, and E. S. Husebye, Determination of the three-dimensional seismic structure of the lithosphere, *J. Geophys. Res.*, *82*, 277-296, 1977.

Aki, K., and P. G. Richards, *Quantitative seismology: theory and methods. Vol. 1*, 557 pp., W. H. Freeman and Co., New York,1980.

Cressie, N. A. C., *Statistics for spatial data*, 900 pp., John Wiley and Sons, Inc., New York, 1993.

Dueker, K., E. Humphreys, and G. Biasi, Teleseismic imaging of the western United States upper mantle structure using the simultaneous iterative reconstruction technique, in *Seismic tomography, theory and practise*, edited by H. M. Iyer and K. Hirahara, Chapman and Hall, London, 265-298, 1993.

Dziewonski, A. M., and D. L. Anderson, Preliminary reference Earth model, *Phys. Earth Planet. Inter.*, *25*, 297-356, 1981.

Dziewonski, A. M., and D. L. Anderson, Seismic tomography of the Earth's interior, *Am. Sci. 72*, 483-494, 1984.

Efron, B., Nonparametric estimates of standard error: the jackknife, the bootstrap and other methods, *Biometrika*, *68*, 589-599, 1981.

Efron, B. and G. Gong, A leisurely look at the bootstrap, the jackknife, and cross-valida-

tion, *Am. Stat., 37*, 36, 1983.

Engdahl, E. R., N. H. Sleep, and M. Lin, Plate effects in North Pacific subduction zones, *Tectonophysics, 37*, 95-116, 1977.

Hauksson, E., Structure of the Benioff zone beneath the Shumagin Islands, Alaska: Relocation of local earthquakes using three-dimensional ray tracing, *J. Geophys. Res., 90*, 635-649, 1985.

Hirahara, K., Tomography using both local earthquakes and teleseisms: velocity and anisotropy - theory, in *Seismic tomography, theory and practise*, edited by H. M. Iyer and K. Hirahara, Chapman and Hall, London, 493-518, 1993.

Humphreys, E., and R. W. Clayton, Adaptation of back projection tomography to seismic travel time problems, *J. Geophys. Res., 93*, 1073-1085, 1988.

Julian, B. R. and D. Gubbuns, Three dimensional seismic ray tracing, *J. Geophys. 43*, 95-114, 1977.

Lees, J. M. and R. S. Crosson, Tomographic inversion for three-dimensional velocity structure at Mount St. Helens using earthquake data, *J. Geophys. Res., 94*, 5716-5728, 1989.

Nakanishi, I, and D. Suetsugo, Resolution matrix calculated by a tomographic inversion method, *J. Phys. Earth, 34*, 95-99, 1986.

Nolet, G., Solving or resolving inadequate and noisy tomographic systems, *J. Comput. Phys., 61*, 463-482, 1985.

Nolet, G., Seismic wave propagation and seismic tomography, in *Seismic tomography: with applications in global seismology and exploration geophysics*, edited by G.

Nolet, D. Reidel Publishing Company, Dordrecht, 1-23, 1987.

Nolet, G., Solving large linearized tomographic problems, in *Seismic tomography, theory and practise*, edited by H. M. Iyer and K. Hirahara, Chapman and Hall, London, 227-247, 1993.

Paige, C. C., and M. A. Saunders, LSQR: An algorithm for sparse linear equations and sparse least squares, *ACM Trans. Math. Software, 8*, 43-71, 1982.

Pereyra, V., W. H. K. Lee, and H. B. Keller, Solving two-point seismic-ray tracing problems in a heterogeneous medium; part 1. a general adaptive finite difference method, *Bull. Seismol. Soc. Am., 70*, 79-99, 1980.

Robinson, M., XPICK script, Geophysical Institute, University of Alaska, Fairbanks, Alaska 99775-0800, 1991.

Spakman, W. and G. Nolet, Imaging algorithms, accuracy and resolution in delay time tomography, in *Mathematical Geophysics*, edited by N. J. Vlaar, G. Nolet, M. J. R. Wortel, and S. A. P. L. Cloetingh, D. Reidel Publishing Company, Dordrect, 155- 187, 1988.

Tanimoto, T., and D. L. Anderson, Mapping convection in the mantle, *Geophys. Res. Lett., 11*, 287-290, 1984.

Tarantola, A., *Inverse problem theory: Methods for data filtering and model parameter estimation*, 613 pp., Elseiver, New York 1987.

Thurber, C. H., and W. L. Ellsworth, Rapid solution of ray tracing problems in heterogeneous media, *Bull. Seismol. Soc. Am., 70*, 1137-1148, 1980.

Thurber, C. H., Earthquake location and 3D crustal structure in the Coyote Lake area, Cal-

ifornia, *J. Geophys. Res.*, *88*, 8226-8236, 1983.

Thurber C. H. and K. Aki, Three-dimensional seismic imaging, *Ann. Rev. Earth Planet. Sci.*, *15*, 115-139, 1987.

Tichelaar, B. W., L. J. Ruff, How good are our best models?, *Eos*, *70*, 593,1989.

Um, J., and C. H. Thurber, A fast algorithm for two-point seismic ray tracing, *Bull. Seismol. Soc. Am.*, *77*, 972-986, 1987.

Van der Sluis, A. and H. A. van der Vorst, Numerical solution of large, sparse linear algebraic systems arising from tomographic problems, in *Seismic tomography*, edited by G. Nolet, D. Reidel Publishing Company, Dordrecht, 49-83, 1987.

Woodhouse, J. H., and A. M. Dziewonski, Mapping the upper mantle: Three-dimensional modeling of earth structure by inversion of seismic wave forms, *J. Geophy. Res.*, *89*, 5953-5986, 1984.

Zhao, D. A *Tomographic Study of Seismic Velocity Structure in the Japan Islands*, Ph.D. Thesis, Tohoku Univ., 301 pp., 1990.

Zhao, D., D. Christensen, and H. Pulpan, Tomographic imaging of the Alaska subduction zone, *J. Geophys. Res.*, *100*, 6487-6504, 1995.

CHAPTER 6

Tomographic Inversion for P-wave Velocity Structure in the South-Central Alaska Subduction Zone[1]

6.1 Abstract

A tomographic P-wave velocity inversion for structure beneath southern Alaska is performed with the primary objective of imaging the subducting Pacific plate in this region. Data consist of travel time residuals from ~142,000 local ray paths and relative residuals from ~18,000 teleseismic ray paths. The initial velocity model contained one-dimensional spherically symmetric velocity variations and did not contain a subducting plate structure. The forward problem employed an accurate and efficient three-dimensional ray tracing scheme. The inversion was carried out using an iterative least-squares method. Model corrections take the form of velocity perturbations from the initial model. After the computation of the residuals and relative residuals, the data were divided up into seven nearly equal subsets based on the output of a random number generator. Inversions were carried out independently on each subset and the resultant model corrections from the inversion of each subset were averaged for the final solution. The resulting velocity perturbations indicate that the positive velocity anomaly of a slab-like structure, in the expected location of the subducting Pacific plate, extends to a maximum depth of ~225 km in the Kodiak Island region. We see no evidence of a high velocity anomaly at depths

1. Chapter 6 is composed of the complete text and figures from the manuscript: *Tomographic Inversion for P-wave Velocity Structure in the South-Central Alaska Subduction Zone*, by C. K. Searcy and D. H. Christensen, to be submitted to *J. Geophys. Res, July 1996.*

greater than 250 km anywhere in the model space. The dip of the imaged plate is very shallow in the Prince William Sound region, forming a broad contact zone with the over-riding North American plate. A thickening of the velocity anomaly beneath the Kenai Peninsula may be evidence that a portion of the Yakutat Terrane is being subducted along with the oceanic plate in this area. An abrupt change in the depth of the anomaly appears in the vicinity of the RM-1 line possibly indicating an offset in the subducting plate.

6.2 Introduction

Alaska possesses an interesting tectonic framework because of the accretionary nature of its land-mass due to the translation of terranes from the south and the possible effects of these terranes on the subduction of the Pacific plate. The nature of plate interactions change from classic (normal) subduction from Prince William Sound westward through the Aleutians to a transform fault system in the east, bordering on the North American continent. In the transition zone between these two types of plate boundaries, relative plate motions are more obscure. The transitional geometry of the subducting plate in this region along the Gulf of Alaska is not well known. The Yakutat Terrane is in the process of docking and impinging on the continental mass, transferring stresses landward. It is hypothesized that this terrane is disrupting the subduction regime and possibly causing a repositioning of the subduction zone (*Stone and Wallace, 1987; Lahr et al., 1988*). If so, it is perhaps possible that such repositionings have occurred previously in the history of this region, assuming similar scenarios existed for other accreted terranes that comprise Alaska. This accretionary process appears to have affected the locus of subduction by dis-

placing the trench southward as terranes became accreted to the land mass (*Jacob et al., 1977*).

The trench-volcano gap is approximately 170 km in the central Aleutians and widens to 570 km in the Gulf of Alaska region (*Jacob et al., 1977*). Coincident with this widening is a decrease in the dip angle of the shallow (0-40km) subducting plate from ~ 17° beneath the Central Aleutians to ~5° in the Gulf of Alaska (*Jacob et al., 1977*). In figure 6.1 we show the location of volcanoes in our study area as well as contours of the Wadati-Benioff zones associated with the subducting Pacific plate. At approximately 59°*N* latitude (near the Cook Inlet), the strike of the Aleutian volcanic line abruptly changes by about 15° bending northward, as does the corresponding Wadati-Benioff zone (*Pulpan and Frohlich, 1985*). In the Cook Inlet region the plate plunge is not parallel to the direction of plate convergence as it is in the segments to the northeast and southwest of this zone (*Kienle et al., 1983*). Another bend of the Wadati-Benioff zone occurs further inland at approximately 62°*N* latitude (near Denali) bending it back southward again. Seismicity associated with the Aleutian subduction regime ends abruptly along a linear boundary that parallels the relative plate motion vector of the Pacific plate with respect to the North American plate. This line is sometimes represented in figures as the RM-1 line (*Stone, 1983*), since it is parallel to the hypothetical tracks of the Pacific plate about the Euler poles as defined by *Minster et al., (1974)*. A weak Wadati-Benioff zone has been observed beneath the Wrangell Volcanoes to the east (*Stephens et al., 1984; Page et al., 1989*). A large difference in the strike of the Wrangell Wadati-Benioff zone and its steeper dip as compared to the eastern edge of the Aleutian Wadati-Benioff zone has lead to speculation

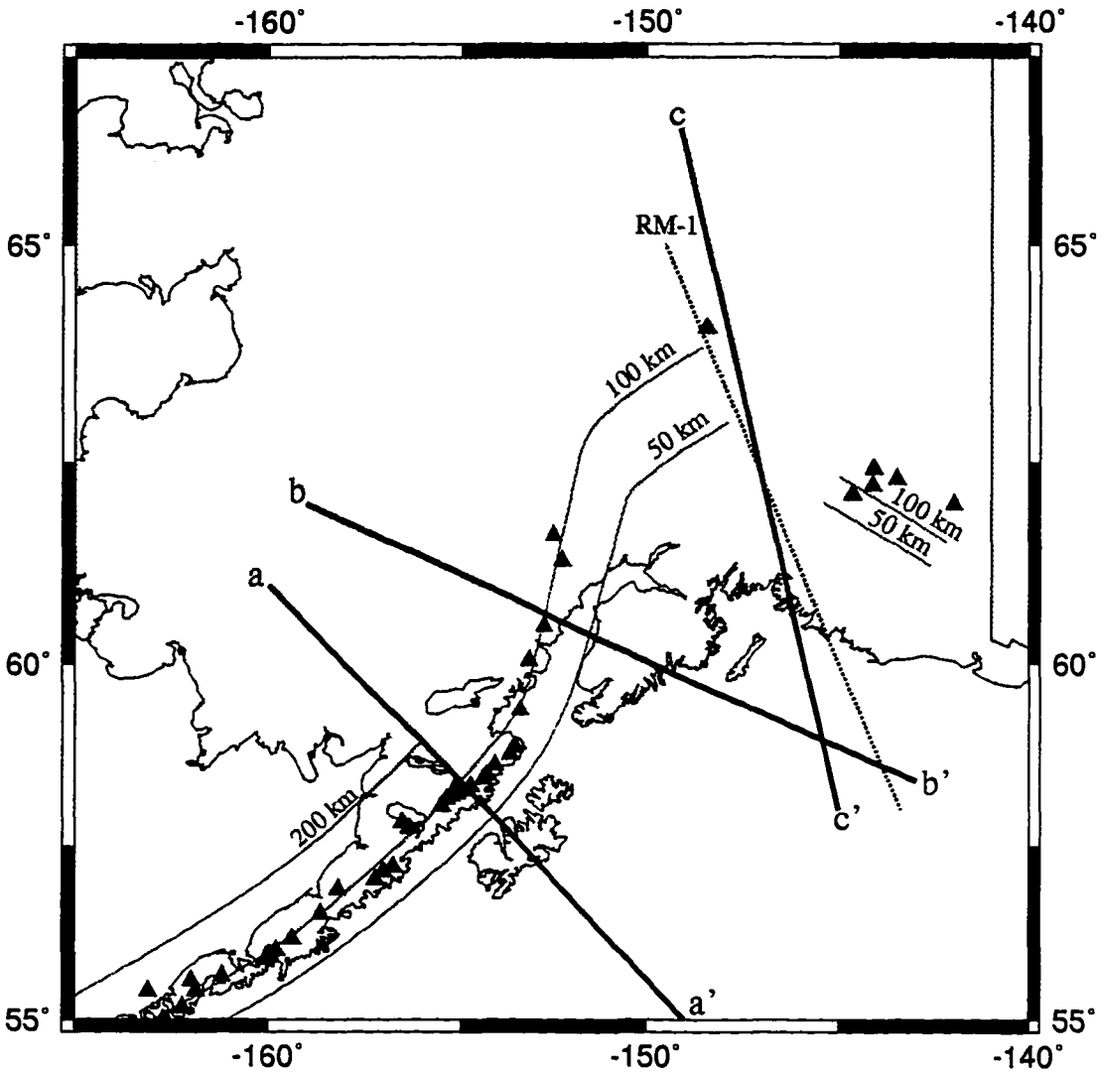

Fig. 6.1: Location of the study area. Black triangles represent volcanoes. Contours of the Wadati-Benioff zone are plotted as thin black lines (from *Page et al., 1989*). Heavy black lines indicate the location of cross sections shown in figures 6.8 and 6.9. The dashed line represents the RM-1 line (*Stone, 1983*).

that the plate may be torn in this region (*Stephens et al., 1984*). Although there is no evidence for an offset in seismicity south of about 61°*N* (*Page et al., 1989*). Nevertheless, this conclusion seems plausible considering the sharp truncation of the eastern edge of the Aleutian Wadati-Benioff zone and the sparseness of seismicity in the region between the Aleutian Wadati-Benioff zone and the Wrangell Wadati-Benioff zone. Geometrical studies by *Yamaoka et al. (1986)* concluded that in most cases, the shape of the world's Wadati-Benioff zones can be simulated by a simple bending of the lithospheric plate However, they note that regions occur in which a good fit can be achieved by placing a tear along a trace of low seismicity. In any case, if the plate is not torn it must undergo a severe contortion in this region.

The depth to which the Pacific subducting plate extends beneath Alaska has not been clearly established. *Delong et al. (1978)* report that there has been continuous underthrusting at the Aleutian trench since at least 40 to 50 m.y. ago. They estimate that 900 to 1000 km of oceanic floor has been subducted since 30 to 35 m.y. ago, which is when the Kula Ridge was consumed. The maximum depth of earthquakes associated with the Aleutian Wadati-Benioff zone in the study area is 150 - 225 km (*Page et al., 1991; Page et al., 1989; Pulpan and Frohlich, 1985*). For the less well defined Wrangell Wadati-Benioff zone, seismicity extends to a depth of 100 km (*Stephens et al., 1984; Page et al. 1989*). Results from a simultaneous travel time/earthquake location inversion for the Central Aleutians carried out by *Engdahl et al. (1987)* suggests that the slab extends about 100 km below the deepest seismicity to a depth of ~275 km. *Jacob et al. (1977)* reasoned that the Pacific plate lithosphere at a depth of 150 km beneath Denali has been subducting for

approximately 10 m.y. which may be consistent with the thermal equilibrium of a down-going slab so that it no longer displays seismicity nor a high velocity anomaly. The time constant of 10 m.y was arrived at by *Isacks et al. (1968)* by comparing the lengths of the world's seismic zones with their estimated slip rate.

In this paper, a tomographic velocity inversion for Alaska is described in which P-wave travel time residuals from local and teleseismic events are inverted to obtain a velocity structure beneath Alaska to a depth of 500 km. The boundaries of the study area are shown in figure 6.1. The method used is similar to that of *Zhao et al. (1995)*, which uses the LSQR (*Paige and Saunders, 1982*) algorithm to carry out least-square inversions of the data. Primary differences between the study presented here and the *Zhao et al. (1995)* study are: the nature of the initial velocity model used in the inversions and the inclusion of teleseismic data. The final results for the *Zhao et al. (1995)* study were based on an inversion in which the initial model contained a high velocity slab structure. For the study presented here the initial velocity model is spherically symmetric and contains no such slab-like structure. While the Zhao et al. (1995) study produced interesting results, we feel that the inclusion of a high velocity slab anomaly in the initial model inhibits the ability of the velocity inversion to resolve the geometry of the subducting slab. In such a case, it is unclear which part of the high velocity anomaly in the images derive from the data and which part exists due to the initial model.

6.3 Data

The data for the velocity inversion presented here consist of both teleseismic

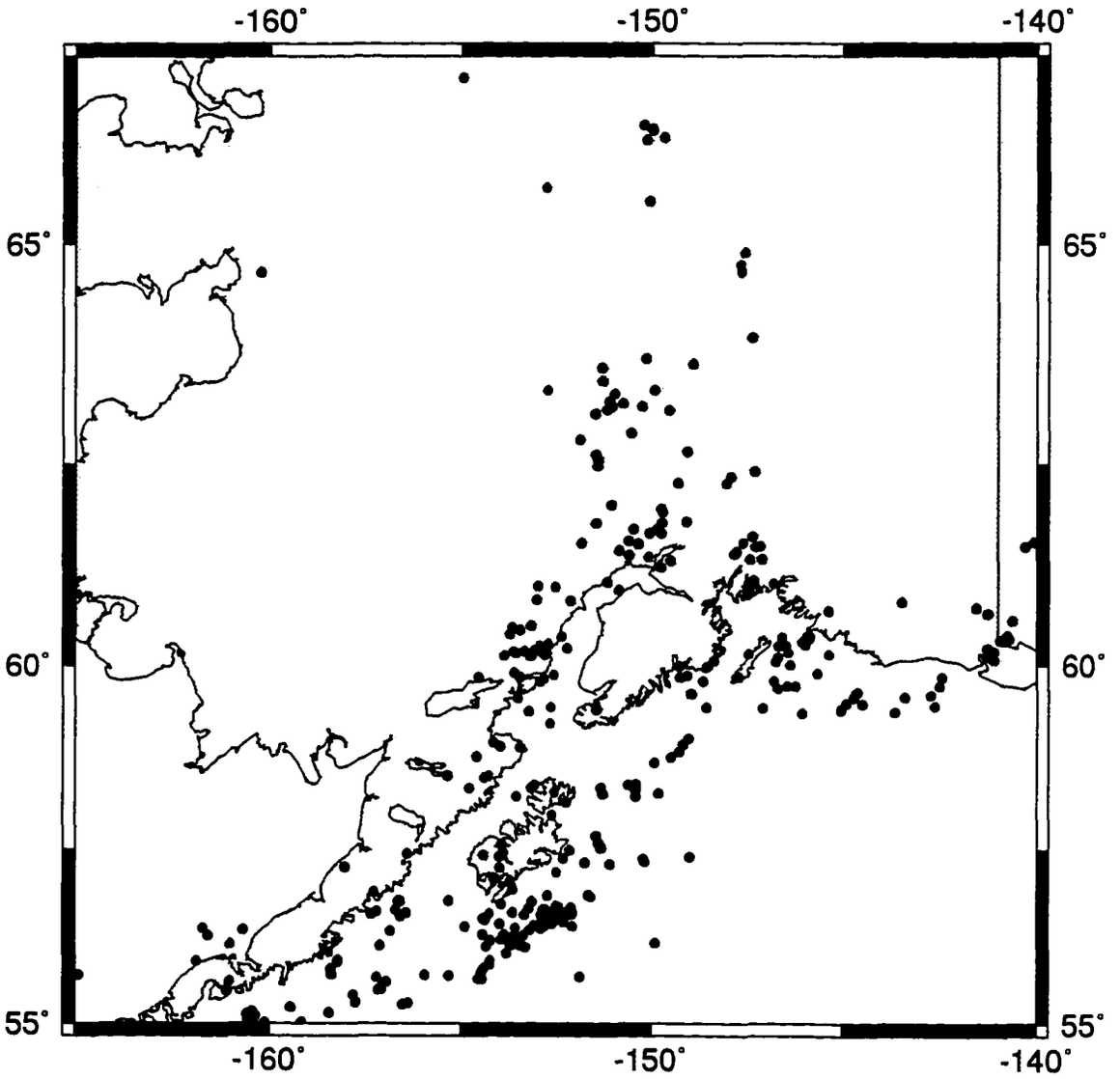

Fig. 6.2: Epicentral location of earthquakes that comprise the outgoing teleseismic data set. Relative residuals from these events as well as those from an incoming teleseismic data set were combined with residuals from a local data set shown in figure 6.3 for the final velocity inversion.

($30° \leq \Delta \leq 90°$) and local P-wave arrival times. Teleseismic data consist of 167 events that occurred in Alaska and were recorded on world-wide stations (outgoing data set) as well as 320 events that occurred world-wide and were recorded on the Alaska Seismic Network (incoming data set). Earthquakes used for the outgoing teleseismic data set are shown in figure 6.2. Relative residuals as proposed by *Aki et al. (1977)* were used for teleseismic data. A relative residual for the ith ray path is defined as:

$$R_i = (T_{obs} - T_{th})_i - \frac{1}{n}\sum_{j=1}^{n}(T_{obs} - T_{th})_j$$

Where T_{obs} is the observed travel-time and T_{th} is the theoretical travel-time. For the incoming data set, j is summed over all the ray paths from one earthquake, for the outgoing data set, j is summed over all the ray paths recorded at one station.

Local data consist of travel time residuals derived from relocated hypocenters taken from *Zhao et al. (1995)*. In their study, the relocations were carried out jointly with a velocity inversion assuming the presence of a high velocity subducting slab in the initial model. The total number of local events was 12,237. The epicentral location of these earthquakes are shown in figure 6.3. The location of Alaska stations at which both the incoming teleseismic data set and the local data set were recorded are shown in figure 6.4.

While the number of data used in this study is large (~150,000 ray paths), ray path coverage is not uniform throughout the model space. Most local and outgoing teleseismic events are confined to the upper crust or the Wadati-Benioff zone associated with the subducting slab above a depth of ~200 km. There are some events in the Wadati-Benioff zone

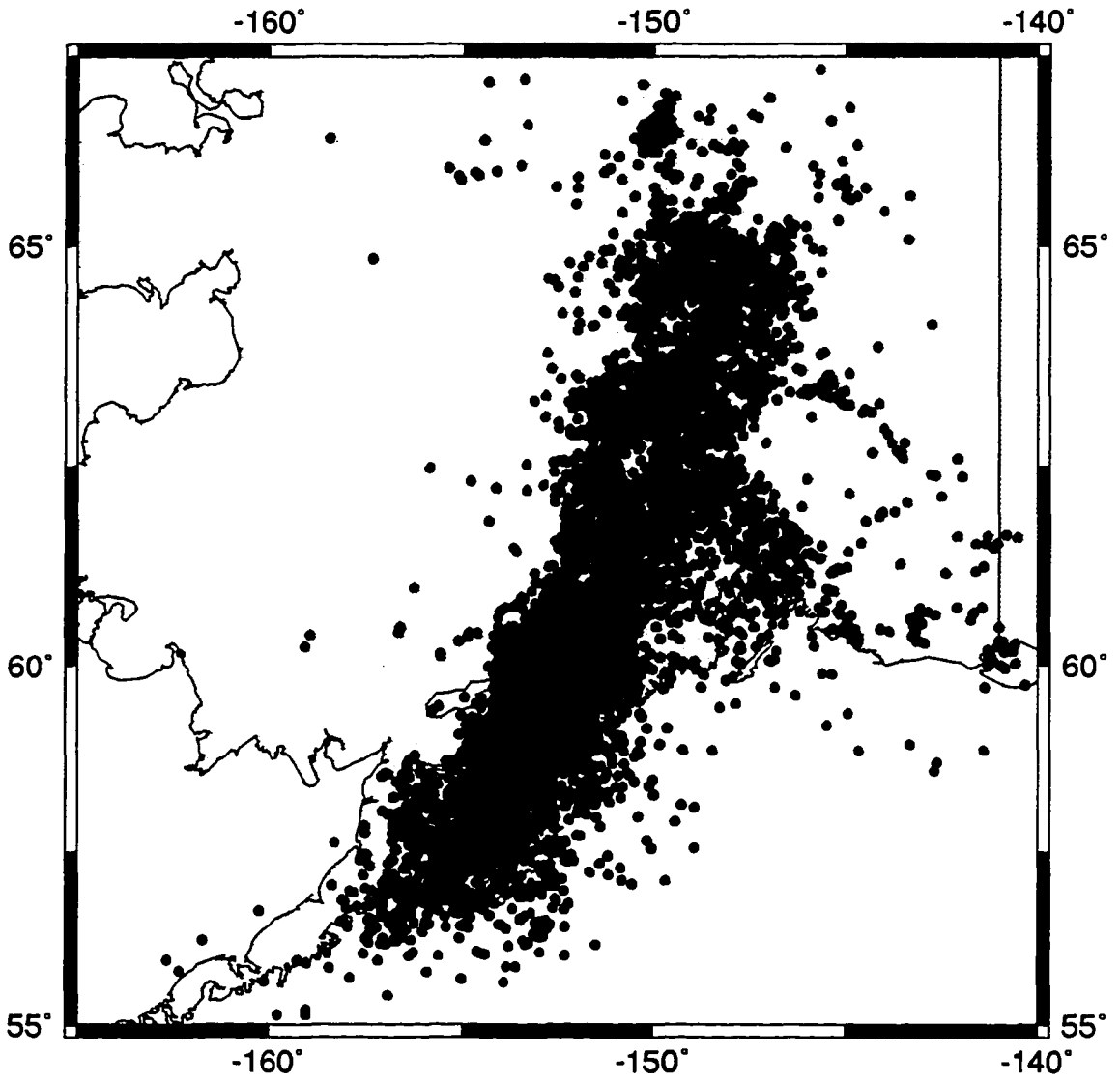

Fig. 6.3: Epicentral location of local earthquakes taken from *Zhao et al. (1990)*. These events were recorded on stations located in Alaska.

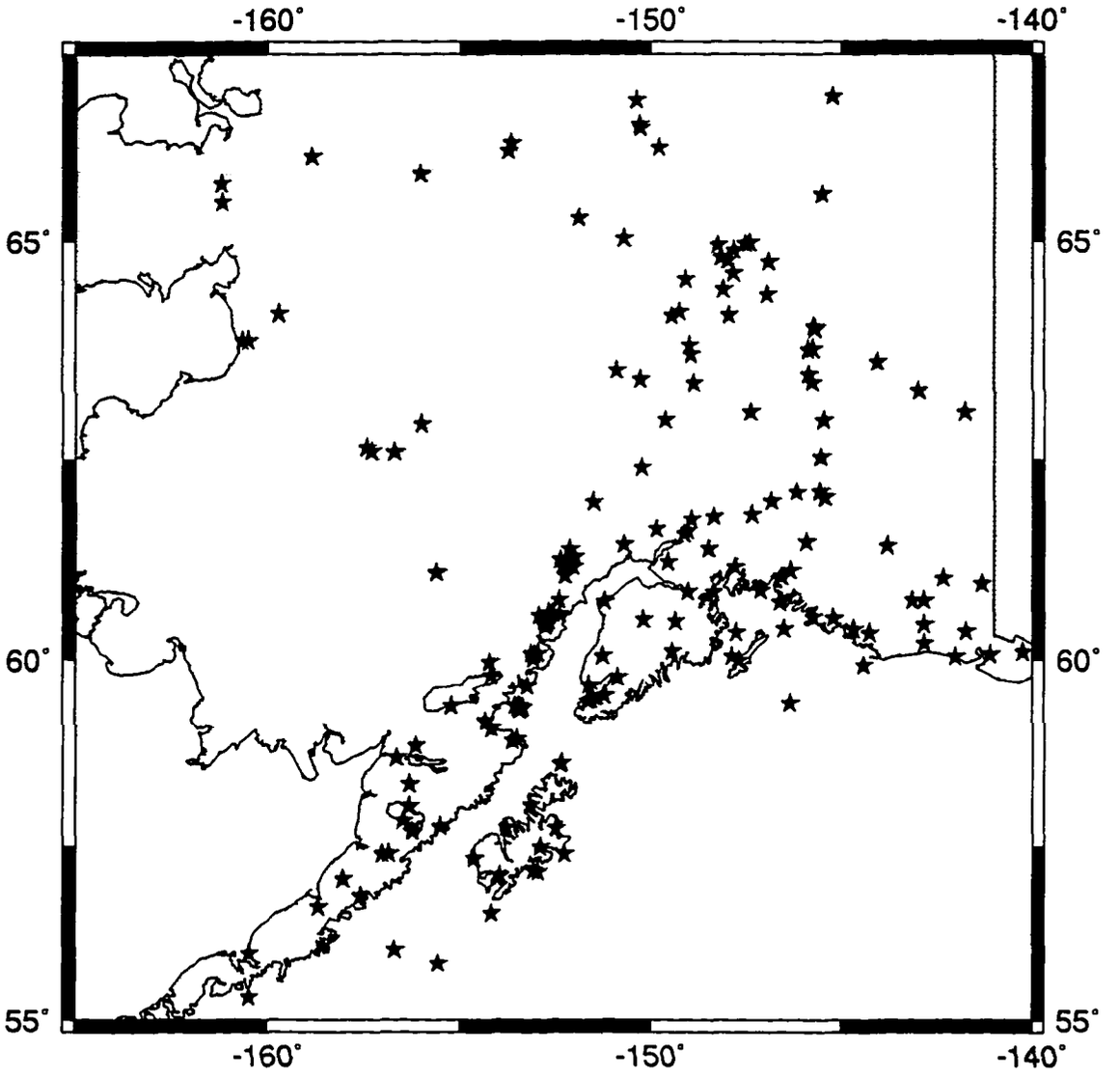

Fig. 6.4: The location of 237 Alaska stations at which incoming teleseismic earthquakes as well as local earthquakes were recorded.

in the depth range of 200 to 250 km. Accuracy of the local arrival time picks, as reported by *Zhao et al. (1995)* is estimated to be 0.1-0.2 s. For the outgoing teleseismic data set P-wave, arrival picks were taken from the International Seismic Center (ISC) catalog and only events with reported errors of 0.1 s or less were selected. P-wave arrival times for the incoming teleseismic data set were hand-picked from seismograms recorded at the Geophysical Institute using the program XPICK (*Robinson. 1991*). Only the most impulsive events were selected for this set and picking errors are believed to be less than 0.1 s.

6.4 Methods

Ray tracing was accomplished with an algorithm developed by *Zhao (1990)* which uses a combination of Snell's law and *Um and Thurber's (1987)* pseudo-bending method. Pseudo-bending is a two-point bending approach that uses a geometric interpretation of the ray equations to find a ray path that minimizes travel times in a velocity gradient model. *Zhao (1990)* developed the technique of combining the methods to take advantage of the speed and efficiency of pseudo-bending while retaining the ability of the ray tracing to accommodate velocity boundaries. *Zhao's* method consists of alternately finding the position of points along the ray path, at velocity boundaries using Snell's law and between the boundaries using pseudo-bending. Model parameterization for this study took the form of grid points spaced approximately 25 km in three dimensions. The initial model used for this study was the Preliminary Reference Earth Model (PREM) developed by *Dziewonski and Anderson (1981)*. For the purposes of ray-tracing, PREM boundaries within the model space were considered to be velocity discontinuities at which Snell's law

was applied. Because of the scale of our model space, ray tracing using pseudo-bending alone failed to converge. In test cases, it was found that the added constraint of Snell's law at PREM boundaries provided an approximation to the true ray paths within our observational error. True ray paths being those determined by solving the first order differential equations derived from the eikonal equation along the ray path.

The velocity inversion was carried out using the conjugate gradient algorithm, LSQR developed by *Paige and Saunders (1982)*. Typically, the LSQR algorithm is used to compute model corrections for the entire data set and these corrections are then applied to the initial model for the final solution of a single iteration. A small modification was made to this procedure by dividing the observations into groups, after the forward problem on the entire data set had been completed. Thus all of the model derivatives for the matrix were computed for the entire data set with respect to a common initial model. Model corrections were then individually computed on subsets of the data. The model corrections from each subset were then averaged to obtain a final composite solution.

To assure even coverage of the ray paths within each subset, the data were binned based on the outcome of a random number generator. Hit counts on individual model grid points generated by the ray paths were then visually compared. A hit count is the number of ray paths that pass in the vicinity of a given model node point and is a direct measure of the ray path coverage. We initially chose this averaging technique because the prohibitively large size of the derivative matrix caused computation problems with our computer systems. However, this procedure is analogous to averaging or stacking the velocity corrections. Thus strong signal corrections are enhanced and corrections due to random noise

are diminished. It is evident that errors will be reduced to some extent by averaging, provided that the problem is strongly over-determined as it is in our case (Dr. Ron Berry, personal communication). A rigorous answer as to whether there is a large enough error reduction in using such an averaging procedure as to warrant its use, when not required by computational limits is not addressed in this paper. It was possible to complete a velocity inversion for the local data alone without dividing it into subsets. We attempted to resolve a known velocity structure using first the non-divided local data and then the local data divided into subsets. The local inversion completed by averaging inversion models from data subsets showed a slightly improved ability to reconstruct known images over the inversion obtained from the single complete local data set.

6.5 Resolution and results

In order to test the resolution of our tomographic inversions we chose to use an image reconstruction technique. Travel times from ray paths traced through a synthetic velocity structure are considered as data and then inverted in the same method described for the real data. The resultant images are then compared to the original synthetic structure. Checkerboard image reconstruction tests were performed by *Zhao et al. (1995)* on the local ray paths used in this study. They found the resolution of their velocity model (based on these ray paths) to be 30-60 km, decreasing in resolution as one moves from the center to the fringes of the model space. Their model space extended to a depth of 200 km. We expect the same or slightly better resolution (due to the inclusion of more data from teleseismic ray paths) for the upper 200 km of our model space. Resolution for the

deeper structure, sampled only by teleseismic ray paths will be worse.

In our study, resolution tests were carried out on an initial model containing a slab-like structure of +6% velocity perturbation in the approximate location where the subducting plate is believed to exist based on seismicity. The slab-like structure is extended to the bottom of the model space (500 km) with the same dip as the lower portion of the plate inferred from seismicity. This initial model was chosen to determine the ability and depth to which the ray paths in our data set are able to resolve just such a structure. Resolution inversions were carried out for the combined local and teleseismic data sets (joint data set) and the local data set alone. A cross-section of the synthetic model used in these resolution inversions is shown in the top figure 6.5. Results from the resolution inversion using the joint data set for this same cross section is shown in the middle of figure 6.5. The results from the resolution inversion using the local data set alone for this cross section is shown on the bottom of this same figure. On the top of figure 6.6 we show the same synthetic velocity model in map view at a depth of 200 km. In the bottom left of this figure we show results from the local inversion and on the right results from the joint inversion. More ray paths exist in the local data set (~120,000) compared to the teleseismic data set (~37,000) and it was therefore expected that resolution for shallower structure (< 200 km) would be better than for deeper structure as previously mentioned. This was indeed found to be the case, however inversions using the joint data set were able to resolve portions of the slab model in the deeper regions. In the center of our model space the anomaly is reconstructed all the way to the bottom of the model space. Furthermore, resolution of the anomalous structure at shallow depths is enhanced by inclusion of the

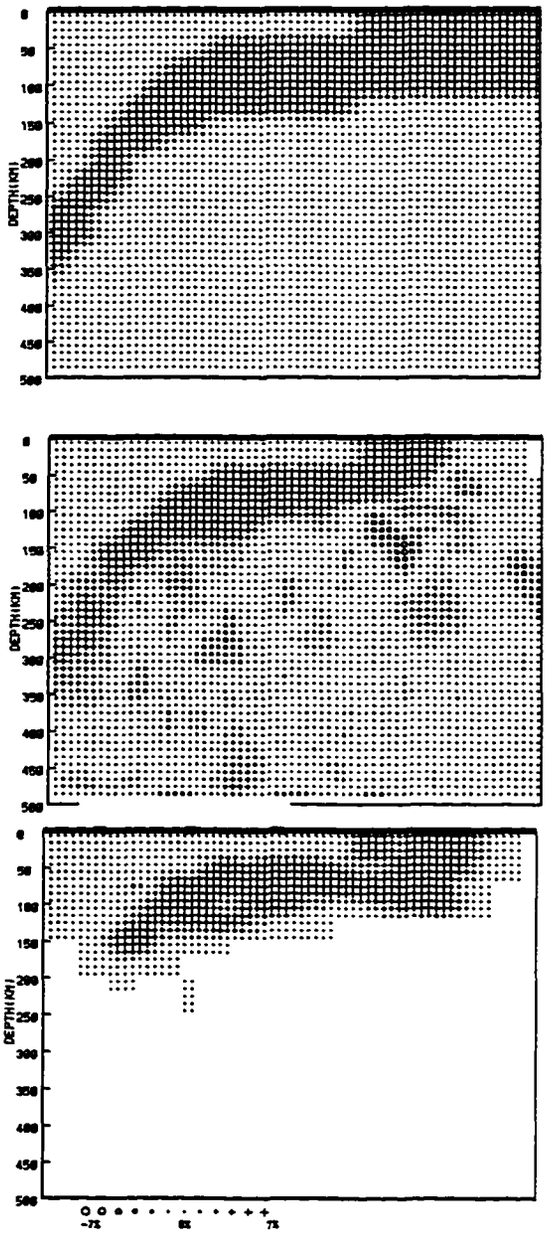

Fig. 6.5: Resolution tests. The top figure is a cross-section of the synthetic model used in the resolution tests. This model extends to the bottom of the model space (500 km). The middle figure is the result from the joint (local and teleseismic data) inversion for this structure. The bottom figure is the result from the local inversion. Plotted are velocity perturbations from PREM in percent. Blank regions represent areas of the model space for which the velocity inversion was not carried out due to a lack of ray path coverage. The resolution is best for depths < 200 km. Although the joint inversion is able to image some structure beneath this depth. Features on the top boundary are well resolved to 200 km.

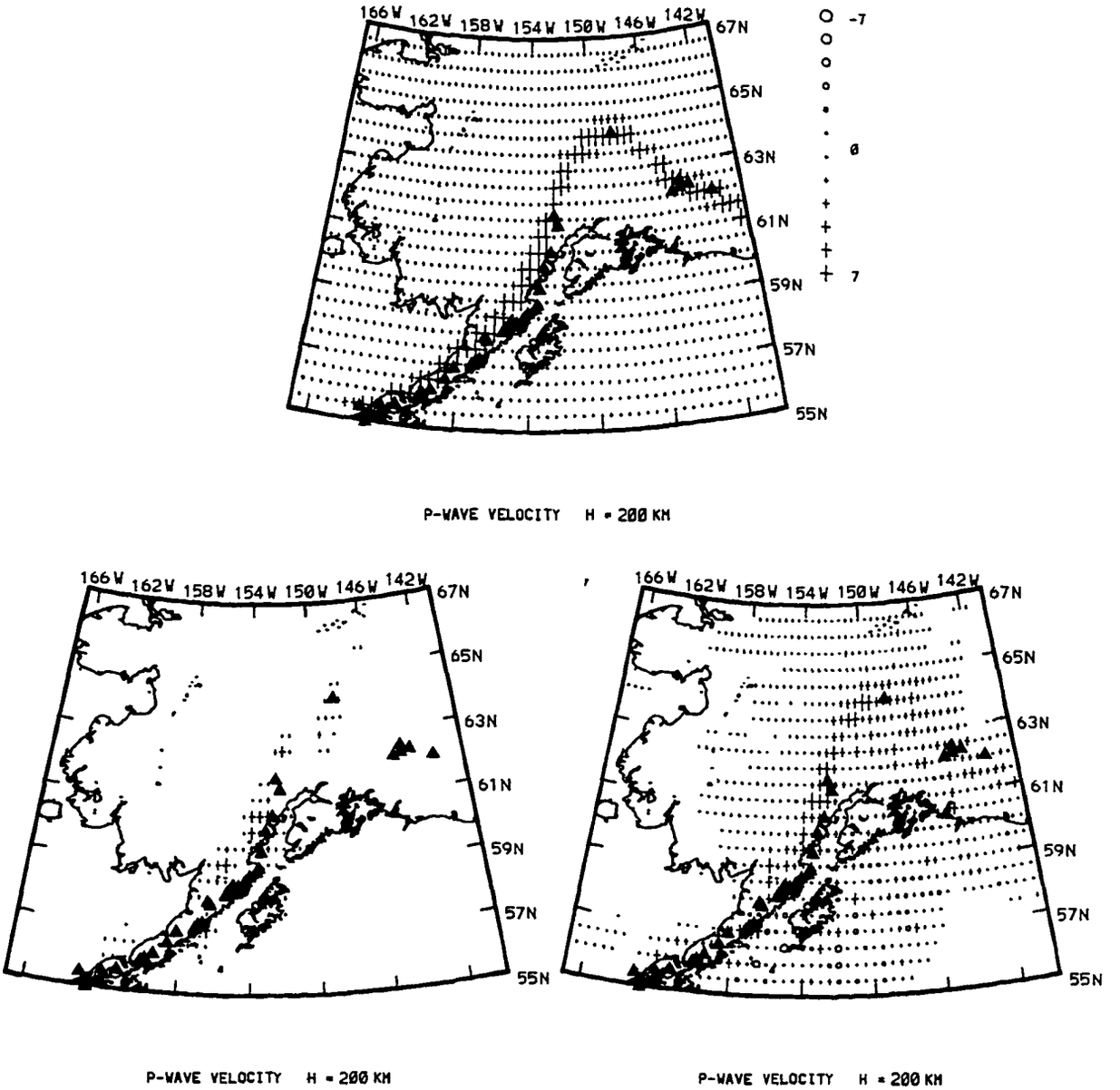

Fig. 6.6: Map view of resolution tests. The top figure is a map view at 200 km depth of the synthetic velocity model used in the resolution inversions. Results from the local inversion are shown in the bottom left figure and results from the joint inversion are shown in the bottom right figure. Blank regions represent areas of the model space for which the velocity inversion was not carried out due to a lack of ray path coverage. Resolution of the deeper velocity structure is improved by the inclusion of teleseismic data.

teleseismic data. Most notably, structure on the top of the slab-like anomaly is well resolved to a depth of approximately 200 km. The structure on the bottom side of this anomaly is not well resolved. Inclusion of the teleseismic ray paths does introduce some noise in the solution due to vertical smearing of the anomaly. This effect is noticeable when a large number of ray paths follow very similar trajectories without the benefit of crossing ray paths. This noise manifests itself in anomalous streaking in the mantle region of the velocity perturbation images.

These tests indicate the ray path coverage from our data set will not be able to resolve the lower boundary of a subducting plate but should be able to reasonably resolve structure on the upper boundary of this plate for depths less than 200 km. While we are unable to resolve details of any structure below 200 km we are able to pick up some indications of the existence of strong anomalies below this depth. A resolution test was also carried out using a synthetic model in which the high-velocity plate anomaly abruptly ends at a depth of 200 km. We were primarily concerned with teleseismic ray path smearing along dip of a plate structure causing the imaged structure to appear to terminate at a deeper depth than the actual anomaly. The results from these inversions showed very little and in some cases no smearing of the high velocity anomaly into deeper depths along the dip of the actual anomaly. Although, in most cases the edge of the anomaly at 200 km is not sharply imaged but rather appears fuzzy.

The joint velocity inversion was able to image the subducting plate in the region from a longitude of about $158°W$ to $142°W$. The region beneath the Wrangell volcanoes in the southeastern part of the state was not resolved due to a lack of ray path coverage in

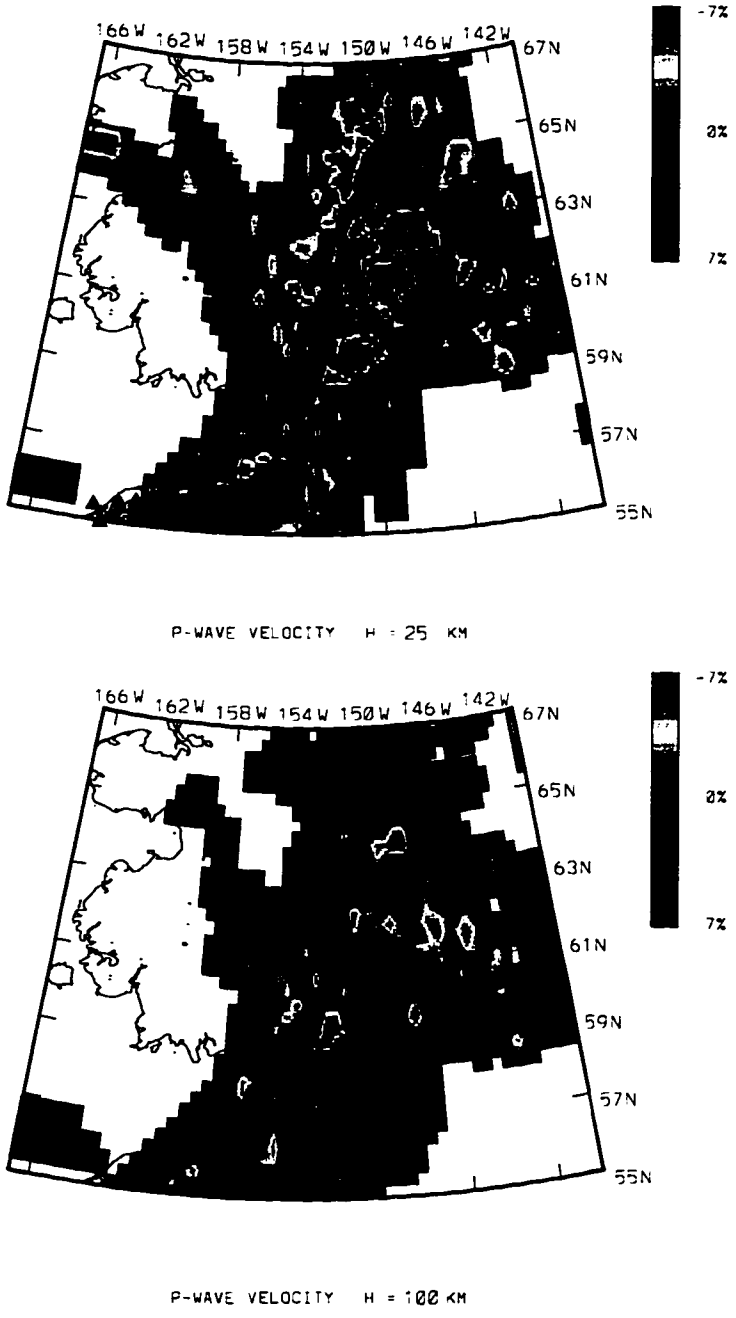

Fig. 6.7: Results of the velocity inversion for 25 km (top figure) and 100 km (bottom figure). Plotted are P-wave velocity perturbations from PREM in per cent. The solid triangles in the top figure indicate the locations of volcanoes. Blank areas represent regions of the model space for which the inversion was not carried out due to a lack of adequate ray path coverage.

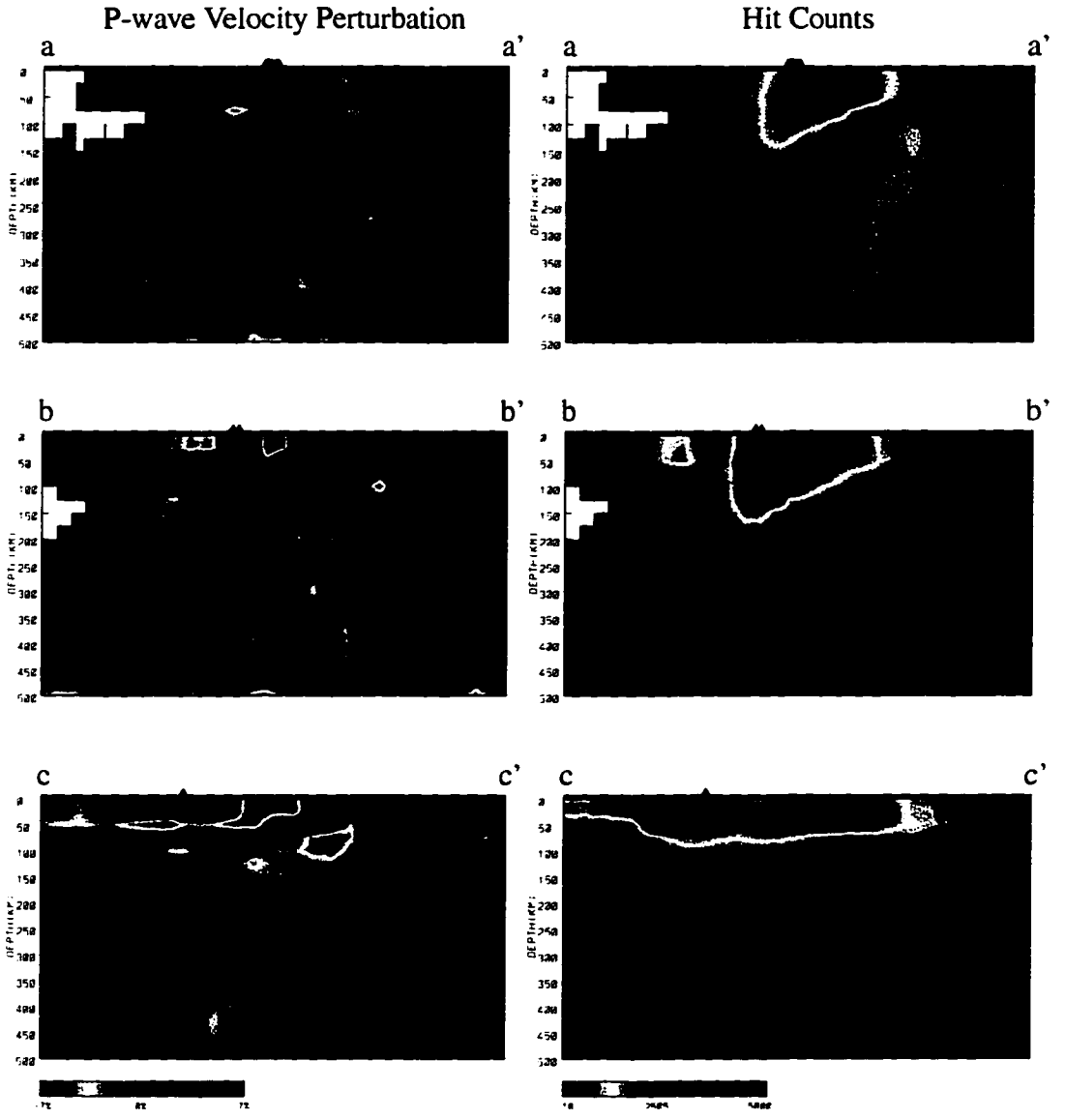

Fig. 6.8: Cross sections of the velocity inversion results and contoured hit counts for the model grid points. Locations of these cross sections are shown in figure 6.1. Plotted on the left are P-wave velocity perturbations in percent from PREM. Cross section **a-a'** shows a velocity anomaly to a depth of ~225 km. There appears to be a steepening of the dip angle at about 75 km. The fast anomaly imaged beneath the plate is artificial due to teleseismic smearing. This region is indicated by an "*" in both the velocity perturbation and hit count plots. For cross section **b-b'**, the slow region just to the south of the volcanoes corresponds to Cook Inlet. This image shows a thickening of the high velocity anomaly associated with the subducting plate beneath the Kenai Peninsula. The slight offset in the high velocity anomaly near the center of **c-c'** corresponds to the intersection of the approximate location of the RM-1 line and the cross section.

that area. In figure 6.7, we show the results of our velocity inversion for two depths (25 km and 100 km) in map view. We present the results of the velocity inversion for three cross sections in figure 6.8. Next to the velocity perturbations for each cross section is a plot showing the contoured hit counts for the model nodes in that cross section. Hypocenter locations of events used in this study in each cross section are plotted in figure 6.9. The locations of these cross sections are shown in figure 6.1. In figure 6.8-a, we show a cross section taken through the Kodiak Island area. Portions of the subducting plate are clearly resolved as a positive velocity perturbation of 3-7% from the surrounding mantle. Images of the plate beneath the Kodiak Island area indicate a dip of about 30° with an increase in dip to about 60° at a depth of approximately 75 km. The depth to the end of the slab anomaly in this region is about 225 km. The prominent fast anomaly occurring beneath the image of the slab (indicated by a "*" in figure 6.8-a) is due to anomaly smearing from a set of teleseismic ray paths originating just off Kodiak Island and exiting the model space at a steep angle to the northeast. A three-dimensional examination of the hit counts for the region surrounding each nodal point confirmed that this set of ray paths had very few crossing ray paths especially at depth.

Moving from west to east along the Alaskan coast from Kodiak Island to Prince William Sound, the dip angle of the imaged plate lessens until it is nearly horizontal beneath South Central Alaska. Our images do not indicate a continuous deep slab structure as one sweeps from the region north of Kodiak Island through the Kenai Peninsula to South Central Alaska or at least not one of simple geometry. A cross section through the center of the Kenai Peninsula is shown in figure 6.8-b. The slow region at the surface of

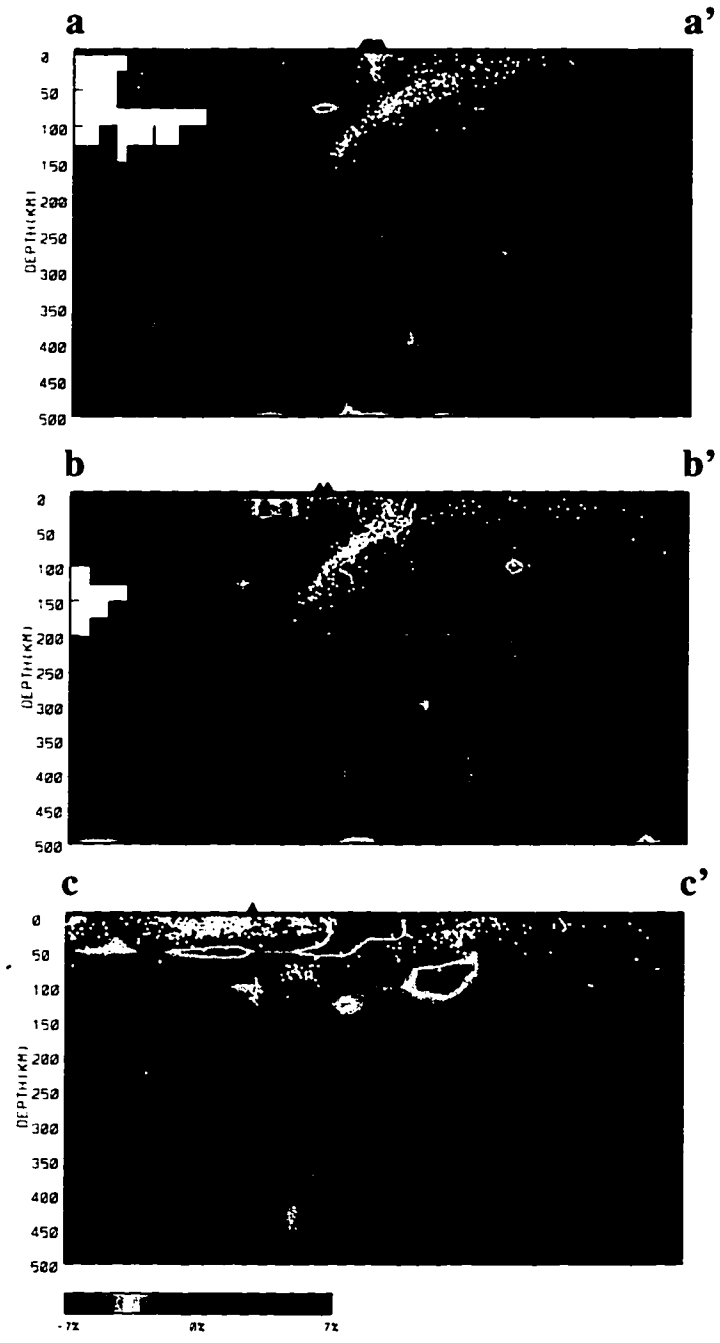

Fig. 6.9: Hypocenter locations of earthquakes used in this study. Cross section locations are shown in figure 6.1.

this cross section corresponds to the Cook Inlet Basin. There appears to be a prominent, isolated thickening of a fast anomaly beneath the Kenai Peninsula and Cook Inlet that we believe is associated with the subducting slab. The anomaly in this area appears to be between 70 to 100 km thick.

In figure 6.8-c we show a cross section of our velocity inversion results taken through the South Central Alaska region. The extremely slow region imaged at the surface corresponds to the surface expression of the Copper River Basin. The image of the plate in this cross section is horizontal except for a step offset that occurs beneath the slow anomaly. This offset drops the center of the imaged anomaly from about 50 km to 75 km. The fast anomaly occurring at the surface in the northernmost area of the cross section corresponds with the surface expression of the Alaska Range.

6.6 Discussion

The results of our velocity inversion indicate that the high velocity anomaly associated with the subducted oceanic slab beneath Kodiak Island abruptly ends at an approximate depth of 200 to 225 km. This depth corresponds with the deepest seismicity associated with the plate in this area (*Pulpan and Frohlich, 1985; Burbach and Frohlich, 1986; Page et al., 1989*). While the resolution of our inversion decreases below a depth of about 200 km, our resolution tests indicate that we should be able to discern some expression of a very strong anomaly into deeper regions. Thermal models predict that the velocity contrast between the slab and the mantle will decrease down dip (*Engdahl and Gubbins, 1987*). A weaker high velocity anomaly below 225 km may not be detectable by

our inversions. East of this area, an increase in dip angle of the plate at a depth of ~100 km has been reported by previous authors *(Reyners and Coles, 1982). Pulpan and Frohlich (1985)* found the change in dip in the Kodiak region to occur at 70 km. For both of these studies, the determination of the dip angle was based on the location of seismicity associated with the Wadati-Benioff zone. It has been reported by *Hauksson (1985)* that a similar steepening of the dip angle in the Shumigan Islands area is artificial, due to a systematic mislocation of Wadati-Benioff zone earthquakes beneath a depth of 100 km. We do not believe this to be the case for our cross-section beneath Kodiak Island since the relocated local hypocenters correspond well to the imaged anomaly.

The lack of continuity of the slab image in our results in the area landward of the Kenai Peninsula could possibly be due to a lack of resolution with our data. This area has long been of interest due to the sharp change in strike of the line of volcanism north of 59° latitude and a corresponding change in strike of the Wadati-Benioff zone. *Burbach and Frohlich (1986)* placed a well-defined plate segment boundary (PSB) at the northern end of Cook Inlet and proposed that it may correspond to a tear in the subducted slab. This conclusion was also reached by *Pulpan and Frohlich (1985)* who also located another possible tear at the southern end of Cook inlet. Their model for the geometry of the subducted slab in this region shows an overlap of lithospheric material at the northern tear at approximately 63°*N* resulting from the eastward bending of the arc. It is also conceded that this lateral bend in the slab could be accomplished by ductile deformation rather than tearing. In the present study, we had hoped to be able to offer some insight into the subducting plate structure in this area. Unfortunately, our images of the slab in this region are

not clear enough to indicate whether there is a tear, a bend or even a thickening of lithospheric material at the point where there is a change in the orientation of the volcanic line.

The cause of the apparent thickening of the slab beneath the Kenai Peninsula and Cook Inlet in our image is unclear. *Pulpan and Frohlich (1985)* report a possible increase in thickness of the Wadati-Benioff zone beneath Cook Inlet as compared to that beneath the Kodiak area and also a higher rate of seismicity in the intermediate depth range, for cross sections somewhat southwest of the cross section we show in figure 6.8-b. They suggest that the increase in thickness may be caused by fragmentation, crumpling or the overlapping of material occurring as it is forced laterally into the mantle due to the bending of the subduction zone. Perhaps a thickening of the subducting plate such as indicated in our images to the northeast is also related to the lateral bending of the arc. Another possibility is that a portion of the Yakutat Terrane is overlying the oceanic plate. Based on a detailed seismic profile study, *Page et al. (1994)* concluded that the lower crust of the Yakutat Terrane is being subducted along with the Pacific crust in the Prince William Sound area. Their profile was located to the east of the cross section shown in figure 6.8-b. The same conclusion was drawn by *Brocher et al. (1994)* also based on seismic profiles. Perhaps the thickened anomaly in our cross section represents the western edge of the subducting Yakutat lower crust. In tomographic inversions of the Kenai Peninsula area, *Kissling and Lahr (1991)* found the upper boundary of the Pacific plate (based on seismicity) to be a region of reduced velocity. The fact that we do not see such a feature in our results may be due to our coarser resolution. The resolution of their model was 10 km.

The shallow slow anomaly in figure 6.8-c is associated with the Copper River

Basin. This basin is known to extend to a depth of ~ 8 km (*Elm. 1983*). The fact that the anomaly appears to be smeared out in depth in our images is probably due to the extremely slow velocities associated with this basin and our grid spacing of 25 km. A slight offset in the high velocity anomaly associated with the subducting slab occurs at the approximate location of the intersection of this cross section with the estimated surface projection of the line along which the Aleutian Wadati-Benioff zone ends (labelled RM-1 in figure 6.8). This is an interesting feature since there has been much speculation on the nature of the subducting plate in this region. No such offset occurs for this cross section in the resolution images so we do not believe it is an artifact of uneven ray path coverage. The structure of the synthetic model in this region was well resolved. Nevertheless, the size of this feature is bordering on the limits of even our best resolution and the region just to the east is poorly resolved. Based on a detailed study of seismicity in this region, *Page et al. (1989)* concluded that the plate is continuous across the RM-1 line at least in the depth range of 20-45 km. A determination of the location of the plate to the east of the cross section in figure 6.8-c would be very helpful in determining the nature of the plate geometry in this area. Unfortunately, in our study, resolution to the east of this cross section is poor due to a lack of ray path coverage. Perhaps future data in this area will shed more light on this feature.

6.7 Conclusions

A tomographic velocity inversion using local and teleseismic data was carried out for Alaska to a depth of 500 km. The results clearly image a high velocity anomaly for the

subducting slab that terminates at a depth of about 225 km. Reconstruction image tests indicate that this is not an artifact due to the diminished resolution beneath a depth of approximately 200 km. We speculate an apparent thickening of the subducting slab beneath the Kenai Peninsula may be caused by the lower crust of the Yakutat Terrane overlying the Pacific plate and being subducted concurrently. An alternate interpretation for this feature is that it is due to crumpling or overlapping of oceanic lithospheric material arising from the lateral bending of subduction zone in this region. A cross section through southern Alaska indicates a very shallow dipping plate with a broad contact zone. An offset in the plate appears to exist at the approximate location of the intersection of the RM-1 line with this cross section. We are not sure that this feature is real but suggest that it may be related to a tear or deformation of the subducting slab associated with the abrupt termination of Aleutian Wadati-Benioff zone seismicity. More data in the Wrangell area may some day provide better insight into the structure of the plate in this area.

Chapter 6 References

Aki, K., A. Christofferson, and E. S. Husebye, Determination of the three-dimensional seismic structure of the lithosphere, *J. Geophys. Res.*, *82*, 277-296, 1977.

Burbach, G. V. and C. Frohlich, Intermediate and deep seismicity and lateral structure of subducted lithosphere in the circum-Pacific region, *Rev. Geophys.*, *24*, 833-874, 1986.

Brocher, T. M., G. S. Fuis, M. A. Fisher, G. Plafker, M. J. Moses, J. J. Taber, and N. I. Christensen, Mapping the megathrust beneath the northern Gulf of Alaska using wide-angle seismic data, *J. Geophys. Res.*, *99*, 11663-11685, 1994.

Delong, S. E., P. J. Fox, and F. W. McDowell, Subduction of the Kula Ridge at the Aleutian Trench, *Geol. Soc. Am. Bull.*, *89*, 83-95, 1978.

Dziewonski, A. M., and D. L. Anderson, Preliminary reference Earth model, *Phys. Earth Planet. Inter.*, *25*, 297-356, 1981.

Ehm, A., *Oil and gas basins map of Alaska, Map SR-32*, Alaska Division of Geological and Geophysical Surveys, Special Report 32, 1983.

Engdahl, E. R. and D. Gubbins, Simultaneous travel time inversion for earthquake location and subduction zone structure in the Central Aleutian Islands, *J. Geophys. Res*, *92*, 13,855-13,862, 1987.

Hauksson, E., Structure of the Benioff zone beneath the Shumagin Islands, Alaska: Relocation of local earthquakes using three-dimensional ray tracing, *J. Geophys. Res.*, *90*, 635-649, 1985.

Isacks, B., J. Oliver, and L. Sykes, Seismology and the new global tectonics, *J. Geophys. Res.*, *73*, 5855-5899, 1968.

Jacob, K. H., K. N. Nakamura, and J. N. Davies, Trench-volcano gap along the Aleutian arc: facts and speculations on the role of terrigenous sediments, in *Island Arcs, Deep Sea Trenches and Back Arc Basins*, Maurice Ewing Series I, edited by M. Talwani and W. Pitman Am. Geophys. Union, 1977.

Kienle, J., S. E. Swanson, and H. Pulpan, Magmatism and subduction in the Eastern Aleutian Arc, in *Arc Volcanism: Physics and Tectonics*, edited by D. Shimozuru and I. Yokoyama, Terra Scientific Publishing Co., Tokyo, 191-224, 1983.

Kissling, E. and J. C. Lahr, Tomographic image of the Pacific Slab under southern Alaska, *Eclogae geol. Helv.*, *84*, 297-315, 1991.

Lahr, J. C., R. A. Page, C. D. Stephens, and D. H. Christensen, Unusual earthquakes in the Gulf of Alaska and fragmentation of the Pacific Plate., *Geophys. Res. Let.*, *15*, 1483-1486, 1988.

Minster, J. B., T. H. Jordan, P. Molnar, and E. Haines, Numerical modeling of instantaneous plate tectonics, *Geophys. J. R. Astron. Soc.*, *36*, 541-576, 1974.

Page, R. A., C. D. Stephens, and J. D. Lahr, Seismicity of the Wrangell and Aleutian Wadati-Benioff zones and the North American plate along the Trans-Alaska Crustal Transect, Chugach Mountains and Copper River Basin, southern Alaska, *J. Geophys. Res.*, *94*, 16,059-16,082, 1989.

Page, R. A., N. N. Biswas, J. C. Lahr, and H. Pulpan, Seismicity of continental Alaska, in *Neotectonics of North America: Boulder, Colorado, Geological Society of America,*

Decade Map Volume 1, edited by D. B Slemmons, E. R. Engdahl, M. D. Zoback, and D. D. Blackwell, 47-68, 1991.

Page, R. A. , T. M. Brocher, C. D. Stephens, J. C. Lahr, K. A. Fogelman, and M. A. Fisher, Piggyback subduction at the eastern end of the Aleutian Trench and the giant asperity that ruptured in the great 1964 earthquake, in *SUBCON, an interdisciplinary conference on the subduction process*, convened by D. Scholl, G. Bebout and S. Kirby, 152-154, 1994.

Paige, C. C., and M. A. Saunders, LSQR: An algorithm for sparse linear equations and sparse least squares, *ACM Trans. Math. Software, 8*, 43-71, 1982.

Pulpan, H., and C. Frohlich, Geometry of the subducted plate near Kodiak Island and lower Cook Inlet, Alaska, determined from relocated earthquake hypocenters, *Bull. Seismol. Soc. Am., 75*, 791-810, 1985.

Reyners, M. and K. S. Coles, Fine structure of the dipping seismic zone and subduction mechanics in the Shumagin Islands, Alaska, *J. Geophys. Res., 87*, 356-366, 1982.

Robinson, M., XPICK script, Geophysical Institute, University of Alaska, Fairbanks, Alaska 99775-0800, 1991.

Stephens, C. D., K. A. Fogelman, J. C. Lahr, and R. A. Page, Wrangell Benioff zone, southern Alaska, *Geology, 12*, 373-376, 1984.

Stone, D. B., Present day plate boundaries in Alaska and the Arctic, in Western Alaska geology and resource potential, *J. Alaska Geol. Soc. 3*, 1-14, 1983.

Stone, D. B. and W. K. Wallace, A geological framework of Alaska, *Episodes, 10*, 283-289, 1987.

Um, J., and C. H. Thurber, A fast algorithm for two-point seismic ray tracing, *Bull. Seismol. Soc. Am.*, *77*, 972-986, 1987.

Yamaoka, K., Y. Fukao, and M. Kumazawa, Spherical shell tectonics: Effects of sphericity and inextensibility on the geometry of the descending lithosphere, *Rev. Geophys.*, *24*, 27-53, 1986.

Zhao, D. A *Tomographic Study of Seismic Velocity Structure in the Japan Islands*, Ph.D. Thesis, Tohoku Univ., 301 pp., 1990.

Zhao, D., D. Christensen, and H. Pulpan, Tomographic imaging of the Alaska subduction zone, *J. Geophys. Res.*, *100*, 6487-6504, 1995.

CHAPTER 7

Summary

This thesis presented three major studies in manuscript form (chapters 3, 4 and 6) as well as two companion chapters describing methods used in the manuscripts (chapters 2 and 5). This body of work represents the significant accomplishments of my doctoral program at the Geophysical Institute, University of Alaska. The primary unifying concept of this work is the study of velocity structure of the crust and mantle in Alaska and the tectonic framework from which this structure arises. The first two manuscripts use the analysis of receiver functions to derive crustal structure in the Fairbanks area (chapter 3) and the Brooks Range (chapter 4). The final manuscript (chapter 6) adduces a three-dimensional tomographic P-wave velocity inversion for the subduction zone beneath south central Alaska.

The principal findings for crustal structure in the Fairbanks study was the identification of Moho at an approximate depth of 32 km dipping to the North at an angle of at least 10°. A low velocity layer was identified between depths of 15 and 28 km that has been recognized in previous studies as a layer of high conductivity. This layer has been interpreted as a layer of flysch that has been thrust beneath the Yukon-Tanana Terrane following the tectonic erosion of the underside of this terrane. This study, therefore supports the concept that there has been large scale interactions between the tectonic terranes in Alaska (such as underthrusting). These interactions may be continuing today with the impingement of the Yakutat block on the Alaska land mass in the southern part of the

state.

The receiver function study of the Brooks Range was enhanced by an S-wave splitting study. Receiver functions were analyzed for four temporary stations in the Brooks Range. These temporary stations were located along the Dalton Highway from Coldfoot Alaska to just north of Atigun Pass. From south to north, the depth to Moho was determined to be 32 km, 40 km, 54 km and 50 km. This result agrees well with previous studies in the Brooks Range.

The tomographic velocity inversion for south central Alaska was conducted to a depth of 500 km. This work was able to clearly image a high velocity anomaly that we identify as the subducting Pacific Plate. The anomaly appears to terminate at a depth of about 225 km supporting the conclusion that a high velocity anomaly associated with the plate does not extend past the known Wadati-Benioff zone seismicity. An offset in the subducting plate occurs inland of the Prince William Sound Region at the approximate location of the abrupt termination of Aleutian Wadati-Benioff zone seismicity. We speculate that this feature is an indication of deformation in the subducting slab at this location. Relative plate motions change from normal subduction in the west beneath the Aleutians to a transform fault in the east. The region between the Aleutian and Wrangell subduction zones, as well as the Wrangell subduction zone itself, are located in this transitional region. This fact, along with the observation that there is an extreme change in orientation between the Aleutian and Wrangell subduction zones imply that the subducting plate in this area must be greatly contorted or torn.

A thickening of the high velocity anomaly beneath the Kenai Peninsula is believed

to represent an underthrust portion of the Yakutat Terrane that is welded to the upper portion of the Pacific Plate. Another scenario for this thickening is presented in which the subducted slab is buckled due to a severe bend in the trend of the slab. Since previous studies present evidence that the lower crust of the Yakutat Terrane has been underthrust beneath the North American Plate in the Prince William Sound region, we favor the first hypothesis. Such a conclusion attests to large scale influences of exotic terranes on the tectonic structure of Alaska. The results of the tomographic imaging in the Kenai region and the receiver function analysis beneath station COL both support the theory that terranes in Alaska may be stacked vertically as well as horizontally. Furthermore, interactions between terranes appear to be complex as in the hypothesized tectonic erosion of the underside of the Yukon-Tanana Terrane suggested by earlier studies and supported by the COL study presented here.